Measurements of the maximum depth of air shower profiles at LHC energies with the High-Elevation Auger Telescopes

Zur Erlangung des akademischen Grades eines

Doktors der Naturwissenschaften

an der Fakultät für Physik des
Karlsruher Instituts für Technologie (KIT)

genehmigte

Dissertation

von

Dipl.-Phys. Alaa Metwaly Kuotb Awad

aus El Fayoum/Egypt

Abstract

More than 100 years after their discovery, the nature of cosmic rays is still a mystery in many aspects. The subject of this thesis is to measure the mass composition of the cosmic rays at an energy range from $10^{15.8}$eV to 10^{17}eV. This relies on the Cherenkov light emitted in the forward direction of the shower, directly pointing towards the telescopes. A new technique was proposed for the reconstruction named Profile Constrained Geometry Fit (PCGF). The benefit of this special technique is a high accuracy geometry reconstruction, which is possible using only the telescope signals. A full PCGF dataset is produced for the Cherenkov dominated showers observed by the High Elevation Auger Telescopes (HEAT). The mass composition is deduced from the distribution of the maximum depth of those showers, $X_{\max}$. The first two moments of the distribution, $\langle X_{\max} \rangle$, and $\sigma(X_{\max})$, are compared to their counterparts of proton and iron simulations. The performance of the reconstruction and the analysis is studied using a complete time-dependent Monte Carlo simulation. It is a novel technique that is used for the first time in Pierre Auger, and by which the mass composition is measured in the energy region where there are signatures of cosmic ray transition from galactic to an extragalactic origin. Successfully, the Pierre Auger measurements in this aspect are extended by one order of magnitude to lower energy toward the knee. The results showed an interesting composition that is heavily dominated by iron around the second knee and towards the knee, it starts to get lighter. The measurements in this energy region will play a critical role in understanding key features of the cosmic ray nature.

Contents

CHAPTER 1

Introduction

The research of "Cosmic Rays" first appeared in the scope of physics in 1912 [1]. Today cosmic rays are understood to be as ionized particles bombarding the Earth from outer space, having energies varying at many order of magnitude of energy from a few GeV to more than 100 EeV. The record in energy measured so far is about 3×10^{20}eV, which was observed by Fly's Eye cosmic ray detector in 1991. If this highest energy particle was a proton, then the energy of its interaction with an air nucleus would correspond to $\sqrt{s} \approx 750$TeV.

Countless theories have been proposed to explain the origin of ultra high energy cosmic rays (UHECRs). Some of them rely on a new physics, and others are more conventional, based on ordinary matter undergoing an acceleration process in a magnetic field of an astrophysical system. Actually, our understanding of the cosmic rays has improve exponentially thanks to modern reliable experiments built especially for this task. It is one of the big questions of fundamental physics to find the origin of cosmic rays that in turn will offer more understanding of the universe around us. One of these experiments, which proudly I am a member of its collaboration, is the Pierre Auger Observatory. Pierre Auger Observatory recently found that the cosmic rays at energies above 8 EeV are propagated to us from extragalactic sources [2]. On the other hand, it is well known that the cosmic rays with energies up to 10 PeV originate inside our galaxy. According to this, there must be a transition between 10 PeV and 8 EeV with a change of the cosmic ray sources. The nature of this transition is one of the biggest mysteries of cosmic rays research today. Many scenarios predict a changing in the mass composition from heavy to light at the transition region. The preference between those models requires accurate measurements of the mass composition in this energy region. One of those scenarios, the "ankle model", which predicts a heavy composition around the ankle region, was already disfavored after the measurements of the Pierre Auger Observatory [3], and Telescope Array [4] showing that the composition is light around $(3-5) \times 10^{18}$eV. So indeed the composition study is of major importance along the whole range of cosmic rays energies.

Understanding the mass composition of cosmic rays in the low energy region of the UHECR spectrum will represent a crucial piece of information, which is needed for a breakthrough in the UHECR physics, since this will put constraints on possible sources and acceleration mechanisms. I am proud to present this thesis as a piece in solving this puzzle. In this thesis, I measure how the cosmic ray compositions change as a signature of the transition from galactic to extragalactic sources. This is the first step by the Pierre Auger Observatory to measure the mass composition at such low energies. It was necessary to make use of a different and custom-developed reconstruction approach for the data analysis. An introduction

to cosmic rays and the derivation of their mass composition from air shower observables is presented in Chapter 2.

At energies above $\approx 10^{18}$eV, the Pierre Auger uses a hybrid design to observe the UHECR. It consist of a large surface array (SD) of 1660 water-Cherenkov tanks covering 3000 km^2 overlooked by 24 fluorescence telescopes (FD) in four sites enclosing the boundary of the SD. To extend the hybrid observation energy down to 10^{17}eV the three High Elevation Auger Telescopes (HEAT) were added to FD of Pierre Auger at the Coiheuco site. Only the showers observed by HEAT are directly involved in the final result of this analysis by concentrating mainly on the showers induced from the Cherenkov light. Performing the analysis in the energy range of interest, $(10^{15.8} - 10^{17})$eV, is not possible with the Pierre Auger standard hybrid technique of reconstruction. This is why in this thesis a different reconstruction technique is introduced to reconstruct the Cherenkov showers observed by HEAT. This reconstruction is a FD based reconstruction named Profile Constrain Geometry Fit (PCGF) which is used for the first time in the Pierre Auger Collaboration. The PCGF was used in 2008 by the High Resolution Fly's Eye, HiRes, [5] and in 2018 by Telescope Array [6] to publish results of cosmic ray energy spectrum. However, these experiments so far did not present their findings on the cosmic ray composition. Hence, this thesis can be considered as the first cosmic ray mass composition study in this energy range using the PCGF technique. An overview of the Pierre Auger Observatory and the reconstruction techniques is given in Chapter 3.

In Chapter 4, I will discuss a special study based on using the amazing feature of HEAT for changing its field of view by tilting up and down. This study is done for two different aspects: first to cross-calibrate the hybrid reconstructed data of Coihueco and HEAT. Second is to measure the detection resolution for the showers reconstructed with PCGF. This study for the first time indicated a clear and significant time-dependence in the calibration of HEAT.

To introduce the Cherenkov dominated showers with the PCGF reconstruction in the Pierre Auger Collaboration was challenging. Most of the available tools were designed to work with the hybrid fluorescence showers. The most important studies I did to overcome these limitations will be introduced in the following two chapters. In Chapter 5, a validation of the reconstruction of the Cherenkov light within the $\overline{\text{Off}\underline{\text{line}}}$ software framework of the Pierre Auger Observatory using a full Cherenkov CORSIKA simulation is discussed. In Chapter 6, the first full dataset of the PCGF reconstruction produced for the entire Pierre Auger Collaboration is presented. As well as the selection criteria of high quality showers for the analysis are determined with a particular explanation for the effect of the limited field of view of the telescopes. For this it was needed to first add the Cherenkov effect to the determination of the field of view. The performance of the reconstruction and the analysis are investigated using a realistic Monte Carlo simulation which is presented in Chapter 7. For this study it was necessary to produce a massive library of more than half million simulated events with the time-dependent detector simulation of the Pierre Auger Collaboration at unprecedented low energies and high Cherenkov fraction. The study of the systematic uncertainties and the stability of the measurements will be presented in Chapter 8. The first results by Pierre Auger Observatory for the mass composition below 10^{17}eV indicates a very heavy, almost iron, composition just before the second knee that clearly gets lighter towards the knee. This interesting result will be discussed in Chapter 9.

CHAPTER 2

Cosmic rays

In 1912 V.F. Hess [1] had recorded an ionization radiation which increases with the altitude. This was the discovery of the "Cosmic Rays". For this discovery Hess has been awarded Nobel price in physics in 1936. The discovery of the cosmic rays was the beginning of a new domain in physical science. There was a great passion to know and understand the mystery of these particles, which are bombarding our Earth from outer space. Where do they come from? How do they accelerate to such high energies? In the way to answer these main questions, many successes have been accomplished in many branches of physics. For instance, cosmic rays played an important role in particle physics, new particles were discovered thanks to the CR[1] [7–11]. Moreover, CRs are the tool to study phenomena at ultra-high energies beyond the reach of the man-made accelerators. In this chapter, I will discuss briefly the most important hypotheses and findings about the acceleration, propagation, and mass composition of cosmic rays as well as how we measure these particles at the ground.

2.1 Energy spectrum

The measurements of cosmic ray particles were recorded with different energies extended over a wide range starts from few GeV up to more than 100 EeV[2]. The interesting thing is that the flux with which these particles reach the Earth is depending on their energy and drops rapidly at high energies. The flux at certain energy ranges is [12]:

$$\text{flux(E)} \sim \begin{cases} 1000 \text{ particles/s m}^2 & \text{GeV} \\ 1 \text{ particle/year m}^2 & \text{PeV} \\ 1 \text{ particle/century km}^2 & 100 \text{ EeV} \,. \end{cases} \tag{2.1}$$

Such a feature makes it not possible to have one type of detector studying the cosmic rays. There are two main type of detections: space-based [13] and ground-based detectors. The first type is also known as the direct experiments and it based on launching small detectors on satellites to the outer space or using balloons to measure the cosmic ray particles in the TeV energy range. The detection of the cosmic rays at highest energy can be possible only on the ground level by using the Earth's atmosphere as a calorimeter and detect the secondary particles produced in the interaction of the primary particles with air molecules. With this

---

[1]Cosmic ray

[2]10^{18} eV

in mind, large area and a clear atmosphere are necessary to build a ground observatory for the high energy cosmic rays.

The experimental study of cosmic rays identifies a power-law energy spectrum, with several important characteristics at certain energies,

$$\frac{dN}{dE} \propto E^{-\gamma}. \tag{2.2}$$

The spectrum as can be seen in Fig. 2.1a appears featureless but scaling it by $E^{2.5}$, the interesting characteristics are displayed, which are more evident in Fig. 2.1b. The energy index γ is 2.7 for energies between 10 GeV and PeV[3] which become steeper, 3.1, around $(3-5) \times 10^{15}$eV this feature is known as the knee [14]. A further steepening of the spectrum at about $(0.8-3) \times 10^{17}$eV is measured [15–17], naturally called the second knee. The $(3-5) \times 10^{18}$eV energy is called the ankle [18] whereof the spectrum becomes flat again. The spectrum ends with strong suppression around 3×10^{19}eV. Each of these features requires an explanation scenario in the acceleration and the propagation from the cosmic rays source which is discussed in the next sections.

2.2 Sources of cosmic rays, acceleration and propogation

In this section, I will give a short review for the most reasonable scenarios that came out in explaining the origin of the cosmic rays.

2.2.1 Acceleration mechanism

There are different available acceleration mechanisms predicting how the cosmic ray primaries are accelerated to such high energies. The observations have shown that the cosmic rays produce a power-law spectrum which are signature of non-thermal acceleration. With this in mind, the first-order Fermi acceleration [20–23], known also as diffusive shock acceleration, is the most promising mechanism for explaining the cosmic rays flux. The principle of this mechanism is an energy transfer between a macroscopic object and a microscopic particle through "collisionless" process. This macroscopic object could be a fast-expanding shock wave traveling with supersonic speed accompanied with a strong magnetic field. The particles bouncing back and forth crossing the shock many times and in each cycle the particle gain energy. The acceleration process continue for a particle till it gains the enough energy to escape from the shock.

The maximum energy a particle can gained is depending on the charge of the particle, the time it lived in the acceleration area, and with no doubt the magnetic field of the shock, $E_{max} \sim Ze\beta_s.B.TV_s$ [12], where $\beta_s = V_s/c$ is the velocity of the shock. As consequence, the heavy nuclei will gain more energy during the acceleration. Such feature in the acceleration can be coupled with another observed in the cosmic ray spectrum. One of the popular explanation for the knee feature is the absence of the light cosmic rays particles to contribute in the flux, since they already reached maximum energy at the possible galactic sources. This means that the knee must happen at different energies for different masses. This theory has been confirmed in the KASCADE-Grande [24] experiment results where it shows that the flux of heavy cosmic rays experiences a break at an energy of 0.8×10^{17}eV, that called the heavy knee. However, there still an argument if the heavy knee is the same as the second knee.

---

[3]10^{15} eV
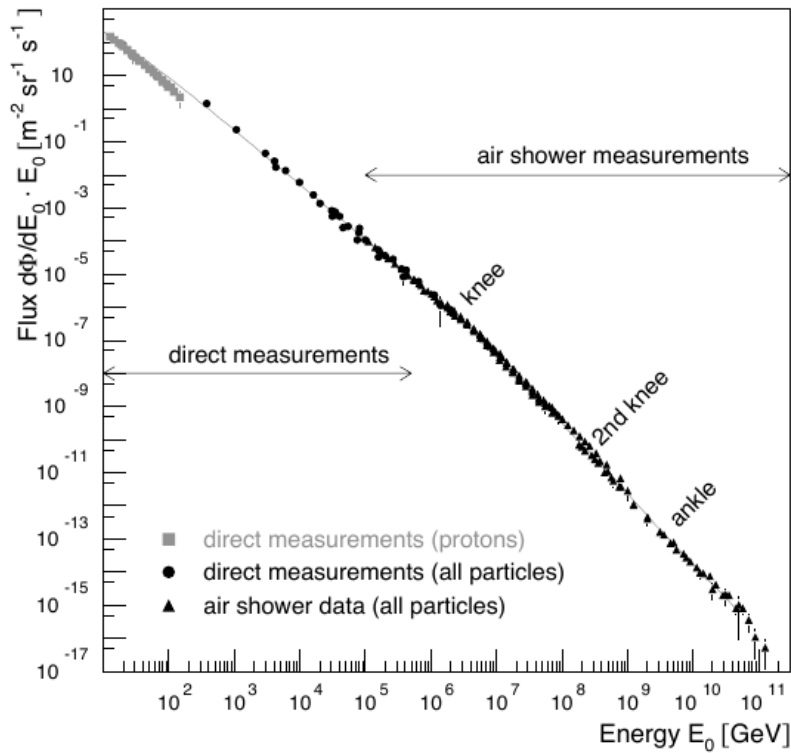
(a) The flux as measured using direct and ground-based detectors. Figure from [12].
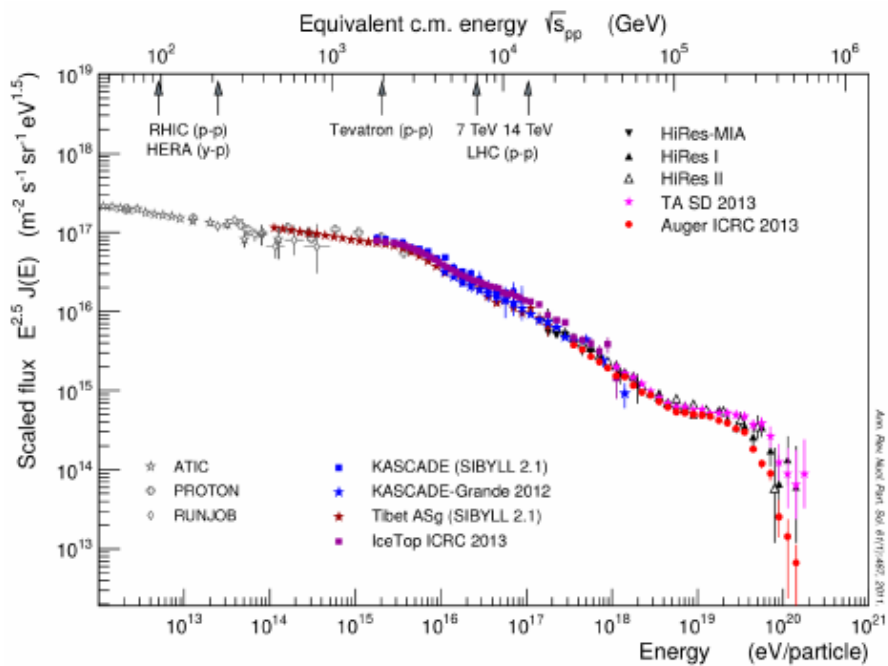
(b) The flux is multiplied by $E^{2.5}$ and the equivalent center-of-mass energy of accelerators at the top axis. Figure from [19].

Figure 2.1: The cosmic ray energy spectrum of all particles flux over twelve decades of energy.

The resulting energy spectrum depending on the first-order Fermi acceleration is a power-law, $dN/dE \propto E^{-2}$ [25], with an index in a good agreement with the observed value after considering the energy losses in propagation from the source till reach our detectors.

2.2.2 Propagation

After being released from the magnetic field of the source, cosmic rays start their journey in propagation in the interstellar space. There are two processes the cosmic rays experience in their way to the observer, which affect their propagation direction, or their energies and compositions. First, the interaction with the cosmic magnetic fields. In this process, the cosmic rays facing traveling troubles; deflection out of the path and time delay. In the second process and especially for those cosmic rays with high energy, they interact with universe backgrounds, for example, the Cosmic Microwave Background, CMB, and the Extra-galactic Background Light, EBL. And as an outcome of these interactions, the energy, and composition of the cosmic rays are changed.

Three expected types processes controlled these interactions, as came in [23], are pair-production, photo-pion production and, only for heavier than protons, photo-disintegration. The more dominant process at high energies is the photo-pion production, in which a cosmic particle, e.g. proton, interacts with the CBM photon and produce pions. This process is one of the most powerful explanations for the sharp suppression observed at the end of the spectrum that known as Greisen, Zatsepin, and Kuzmin, GZK, cut-off [26, 27]. In the case of protons at $\simeq 5 \times 10^{19}$eV the highest interaction channel is the formation of a Δ^+ (1232 MeV) resonance [28]

$$p + \gamma_{CMB} \to \Delta^+ \to \begin{cases} p + \pi^0 \\ n + \pi^+. \end{cases} \tag{2.3}$$
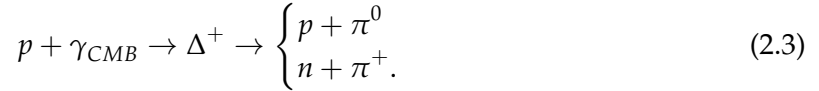
The products, pions and neutron, further decay producing secondary photons and neutrinos

$$\pi^0 \to 2\gamma, \tag{2.4}$$

$$\pi^+ \to \mu^+ + \nu_\mu \to e^+ + \nu_e + \bar{\nu}_\mu, \tag{2.5}$$

$$n \to p + e^- + \bar{\nu}_e. \tag{2.6}$$
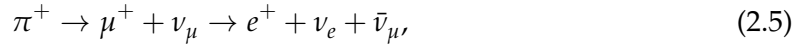
This process happens continuously till the result proton reach an energy below the threshold energy. The pair production process starts at threshold energy 2×10^{18}eV, for proton, in which a pair of electron-positron produces in the interaction with the CMB photons

$$p(A) + \gamma_{CMB} \to p(A) + e^+ + e^-. \tag{2.7}$$
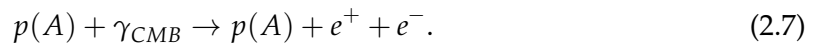
In case of heavy nuclei, A >1, an extra losing energy process can take place; the photo-disintegration which mean that one or more nucleons stripped of the nucleus [29, 30]. This process produced secondary hadronic particles and refer to fact that the heavy injection cosmic rays flux at the source will be observed at Earth as lighter nuclei due to the nucleus disintegration. The same interactions can occur with the EBL photons but with less probability and at lower energies [31]. In Fig. 2.2 a modeling for each of these processes for the energy loss length is shown in case of proton and iron at different energies.

2.2.3 Sources

The cosmic rays suffering many deflections in the magnetic field of the interstellar medium during their propagation due to their feature of being predominantly charged particles. All these deflections make the cosmic rays lost their original path and hence their emission sources are a mystery especially those at Ultra-high energies. But based on the models of acceleration and propagation there are strict requirements must be fulfilled by any astrophysical objects to be considered as a candidate source of the cosmic rays. Hillas [33] studied
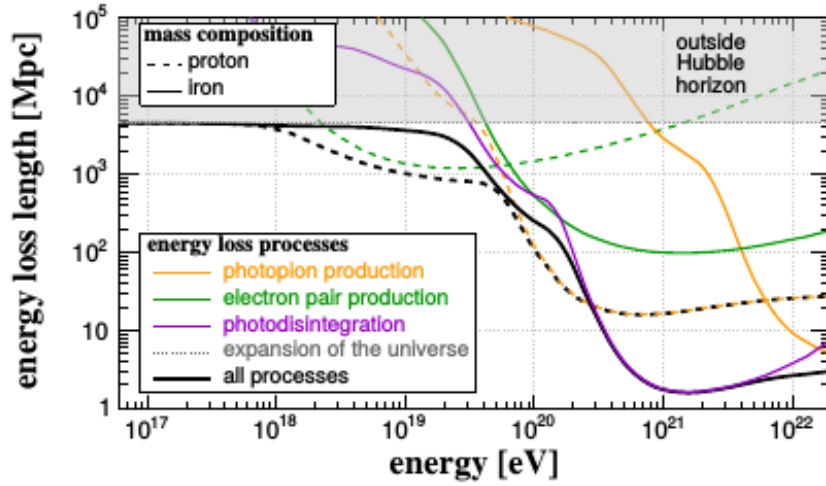
Figure 2.2: The possible processes cause energy lose during the propagation of cosmic rays from the source. Energy loss lengths of proton (dashed lines) and iron (sold lines) for each process and the average of all the processes(black) within the invisible universe. Figure from [32].

these requirements for the known astrophysical objects in the universe and came up with his famous plots, which named after him. In his diagram, Hillas placed the sources in a $B - R$ phase-space depending on their magnetic field strength, B, and size, R, and compare these with the maximum acceleration energy. Hillas criterion stated that the source must has a size larger than the Larmor radius[4] of cosmic rays $R \geq r_L$, where [34]

$$r_L = \frac{E}{ZeB} \sim \frac{110\,kpc}{Z} \left(\frac{\mu G}{B}\right) \left(\frac{E}{100\,EeV}\right), \tag{2.8}$$

in order to be able to trap the particle. From this and with simple calculations one can figure out that the Cosmic rays with energies over 10^{18}eV are not held in the Milky Way Galaxy any more since their Larmor radius are much larger than the thickness of the Galactic disk. So what we observed is originated from extragalactic sources. According to the Hillas plot in Fig. 2.3, the best source candidate to accelerate UHECR are the neutrons stars, Active Galactic Nuclei(AGN), Gamma Ray Bursts (GRBs), and accretion shocks in the intergalactic medium [34]. At lower energies or the galactic sources supernova remnants (SNR) more relevant.

2.3 Transition from galactic to extragalactic

It is widely accepted that the cosmic rays below $\approx 10^{16}$eV are of galactic origin and on the other hand, cosmic rays above $\sim 10^{19}$eV are of extragalactic origin [35]. From this we can infer that between 10^{16}eV and 10^{19}eV there will be a galactic-extragalactic transition. This transition of the cosmic rays from galactic to extragalactic sources are discussed in the light of three models: ankle [36], dip [37], and mixed composition [38]. These three models agree on that the transition is an intersection between a steep component from the galactic and another flatter one from the extragalactic [39]. Most models expect a heavy composition just before the transition value.

The ankle model assumes that the transition appears as a flat feature in all particles spectrum at the ankle region, $(3 - 5) \times 10^{18}$eV. A consequence from this model the ankle

---

[4]The radius of oscillation of a charged particle in a magnetic field.
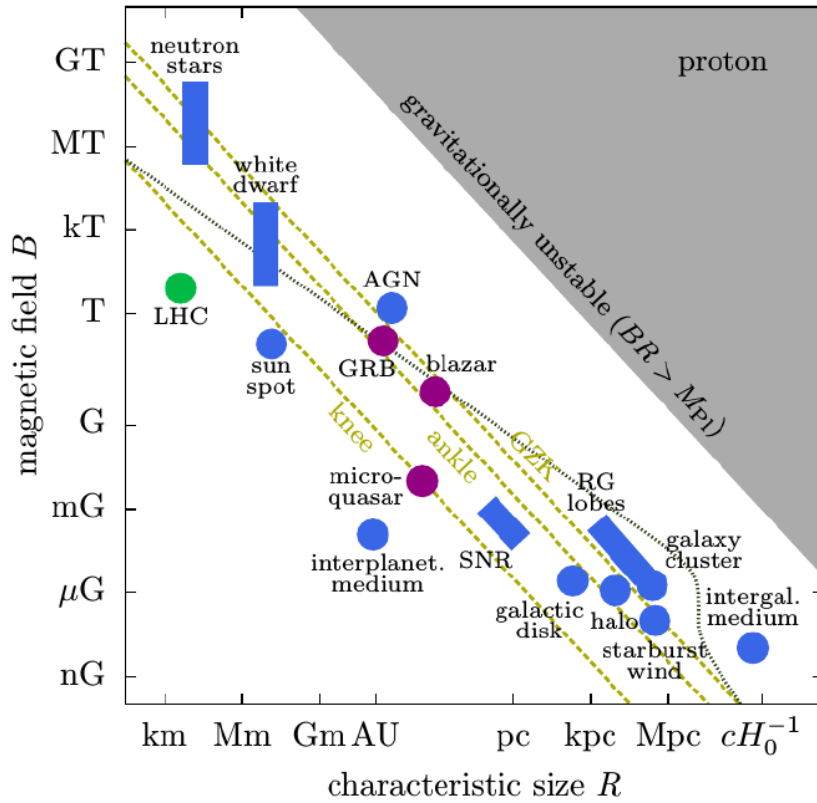
Figure 2.3: Modified version of Hillas diagram, 1984 [33], for the most powerful candidate sources of cosmic rays (blue). The golden dashed lines show the lower limits for the acceleration of protons at energies of the spectrum feature. Figure from [25].

must be dominated by heavy components. This model is constrained by the experimental observations of both Auger and HiRes that showed that the composition is more likely proton around $(2-5) \times 10^{18}$eV [39, 40]. By contrast, the dip model explains the ankle feature in the spectrum as pure extragalactic proton flux that suffers energy losses during their propagation to the Earth. This, in turn, expected the transition between the galactic and extragalactic to be occur at low energies around 0.1 EeV which could explain the feature of the second knee [39, 40]. The mixed composition model is based on an injected mixture of different nuclei from the extragalactic and pure iron composition above 0.1 EeV from the galactic cosmic rays. This model assumed that the ankle can describe the end of the transition from galactic to extragalactic cosmic rays [35, 41]. In Fig. 2.4 the predictions of each model is compared to the experimental measurements. The different models predict significantly different mass composition in the transition region around 10^{17}eV.

2.4 Extensive air showers

An amazing phenomenon occurs continuously in the atmosphere, known as the Extensive Air Shower, EAS. The observation of this phenomenon followed the discovery of the cosmic rays by about 20 years when Bruno Rossi [42] in 1934 observed that the counters placed in a horizontal plane had coincidences counting. Pierre Auger, in 1938 build the first observatory cite to study this phenomenon and the concept of Extensive Air Showers was first introduced by him. Whenever a high energetic cosmic ray particle strikes the Earth's atmosphere an extensive air shower is produced. Being a hadron, the cosmic ray primary particle collides
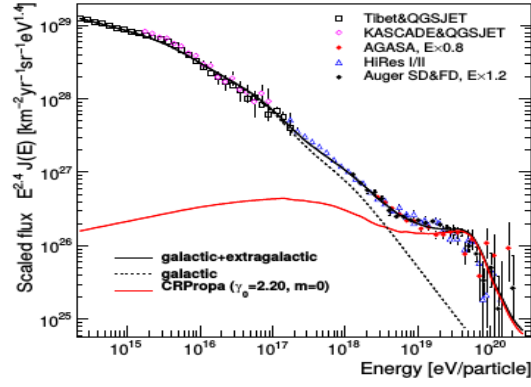
(a) Ankle scenario.
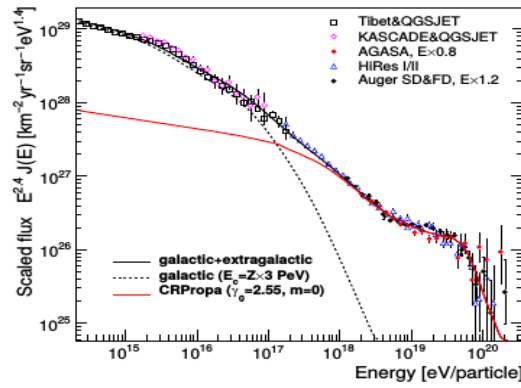
(b) Dip scenario.
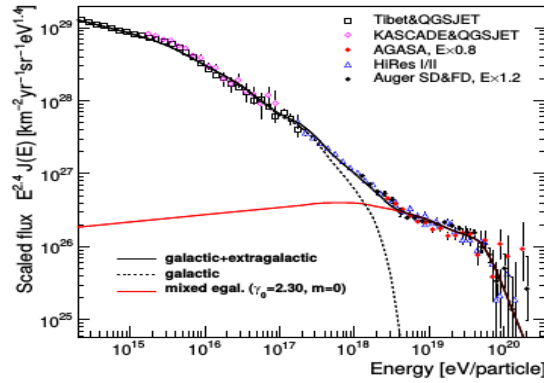
(c) Mixed composition scenario.

Figure 2.4: The transition from galactic to extragalactic cosmic rays In view of three models compared to the experimental observations. The dotted line refer to the expected galactic flux and the red line is the extragalactic one. Figures from [40].

with the air nuclei and produces secondary particles that in turn further interact all the way down in the atmosphere. In the first collision of the primary with air nuclei and through the strong interaction pions, kaons, baryon-antibaryon pairs are produced, but pions are the most frequent. These particles spread laterally and longitudinally in downward by decay or interact more with the air nuclei, mainly nitrogen, oxygen, and argon.

The lower the energy of the secondary particles the wider its spread angle from the shower axis, the direction of the primary particle, that means that the high energy hadrons

will be concentrated in the core of the air shower[5]. This feature of the air shower define the lateral distribution which can be seen in Fig. 2.5a for different shower component simulated with CORSIKA [43]. The shower continuously grows with each interaction of the secondary particles in the atmosphere till it reaches the maximum number of particles, N_{max}, this point in the atmosphere is known as the maximum depth of the shower, X_{max}. Then the decay, for the hadronic component, and the ionization energy loss, for electromagnetic component, will dominate over the interaction process and the shower starts to attenuate. The number of particles produced along the shower axis as a function of atmospheric slant depth is called the longitudinal profile, which is shown for a simulated proton-induced shower in Fig. 2.5b. There are many products in an air shower that can be grouped as a soft component or the electromagnetic particles, a hard component as the hadronic particles, and the muonic component. In addition, there are also productions of fluorescence and Cherenkov light and radio emission. Illustration of the air shower development components are visualize in Fig. 2.6.

2.4.1 Electromagnetic cascade

Electrons and photons interact with the atmosphere through a series of electromagnetic interactions which initiate electromagnetic cascade development. As soon as a high energy photon enters or is created in the atmosphere an electron pair is produced through a pair-production process. The produced high energy electron pair undergoes bremsstrahlung process which in turn emit high energy photon. The features of this cascade well predicted using the very simplistic Heitler model [45, 46]. This model is based on three particles: electron, positron, and photon. In a sequence of bremsstrahlung and pair production processes the number of particles increase by factor of two in each stage and the energy is decreases by splitting equally between the particles in the same stage. Each particle travel a fixed distance $d = \ln 2 \lambda_r$ before splitting, where $\lambda_r \approx 37 g/cm^2$ the electromagnetic radiation length in air. So after n stages, or generations, there will be 2^n particles. These processes continuously grow up building the electromagnetic shower, see Fig. 2.7a, until the individual energy of $e^\pm$ particles drop below the "critical energy", $E_c = 86 MeV$ [19] in air. At which the energy loss due to the ionization equals the energy loss due to bremsstrahlung. At this stage the shower reach its maximum size, N_{max}, at maximum depth X_{max}:

$$N_{max} = \frac{E_0}{E_c} \quad \text{and} \quad X_{max}^{em} \sim \lambda_r ln(\frac{E_0}{E_c}). \tag{2.9}$$

The two important features of the shower cascade are properly described by the Heitler model are that the maximum number of particles in the shower is proportional to the primary particle energy. The second important thing is the dependence of the shower maximum, X_{max}, on the logarithmic primary energy.

2.4.2 Hadronic cascade

The hadronic cascade is not as simple as the electromagnetic one. In this case, the shower development is involving multi-particle productions and also the decay of those particles need to be tracked, which make the analytical solution of the hadronic cascade equations complex. A general vision of the simplistic Heitler model can be used as a description of the hadronic cascade [46]. The principal is to imagine the atmosphere as a layers and each layer has a fixed thickness $\lambda_{ine}\ln 2$, where λ_{ine} is the interaction length. Assuming that the hadron particle, proton, inter the atmosphere with energy E_0 and interact producing N_{tot} particles,

---

[5]The shower core is the point where the shower axis meets the ground
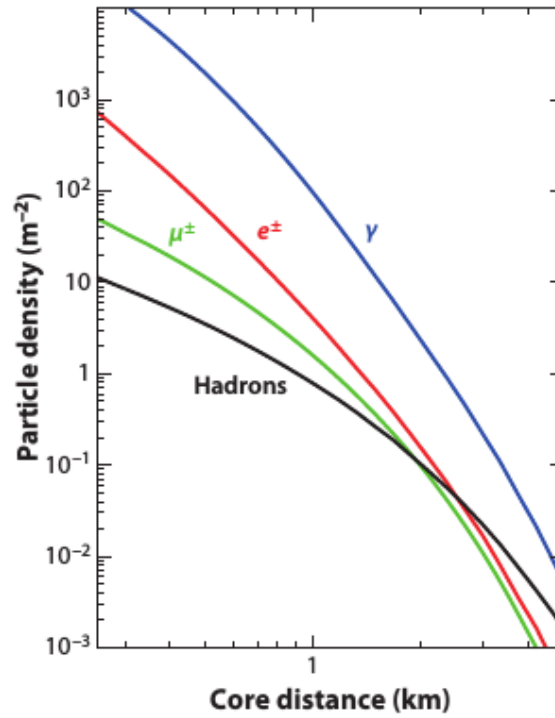
(a) Lateral shower profile.
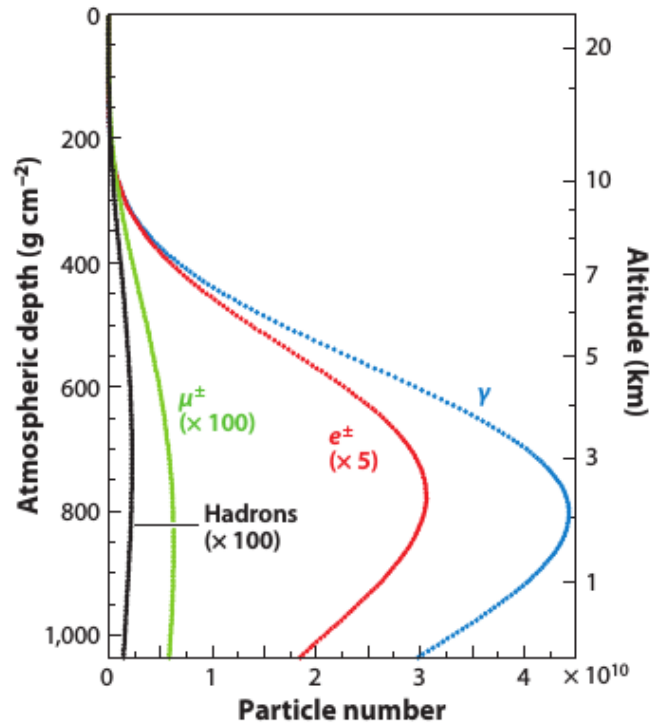
(b) Longitudinal shower profile.

Figure 2.5: Simulation with CORSIKA for proton-induced showers at 10^{19} eV. Figures from [19].

say $\pi^{\pm}$ and π^0, so $\frac{1}{3}N_{tot}$ will be neutral pions and $\frac{2}{3}N_{tot}$ charged pions. The π^0 decay directly into two photons ($\pi^0 \rightarrow 2\gamma$) and start electromagnetic sub-cascade. The charged pions
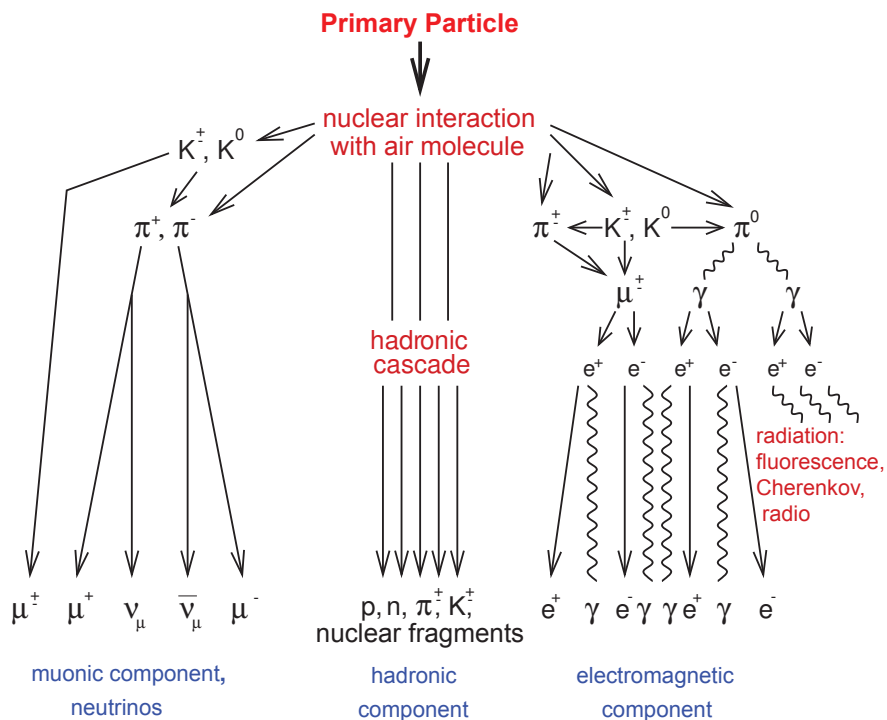
Figure 2.6: An extensive air shower and its main products development. Figure from [44]
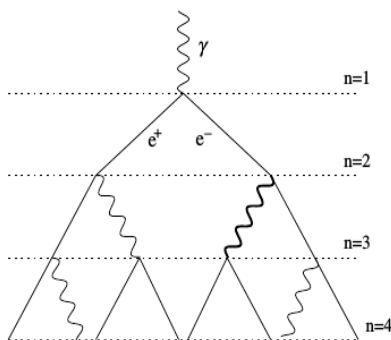
(a) Electromagnetic cascade. Figure from [46].
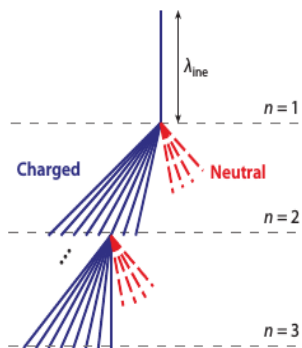
(b) Hadronic cascade. Figure from [19].

Figure 2.7: The development of air shower as described by Heitler model.

continue interact producing new charged and neutral pions. After n generation the energy is distributed between the hadronic and electromagnetic component as:

$$E_{had} = (\frac{2}{3})^n E_0 \quad \text{and} \quad E_{em} = E_0 - E_{had}. \tag{2.10}$$

The process continue till the energy of the pion reach the critical energy, E_c^π, at which the decay mean free path is shorter than the interaction length at about 20 GeV to 30 GeV [46]. Considering the electromagnetic cascade from the first interaction point X_0, the depth of shower maximum of a proton shower is given by

$$X_{max}^{had} \sim \lambda_{ine} + X_0 ln(\frac{E_0}{2N_{tot}E_c^\pi}). \tag{2.11}$$

In light of the superposition model [47], in which a nucleus of mass A is equivalent to a superposition of A individual nucleons, because the binding energy, $\sim 5MeV$, is much smaller compared to the interaction energy. The cascade of heavier nuclei can be described using the proton cascade

$$\begin{aligned} X_{max}^A &= X_{max}^p(E_0/A) \\ &\approx \lambda_{ine} + X_0\left(ln(\frac{E_0}{2N_{tot}E_c^\pi}) - lnA\right). \end{aligned} \tag{2.12}$$

2.5 Light production

Accompanying the cascade of particles in the air shower, there is light produced along the shower track. This light plays an important role in the determination of the longitudinal shower profile, which in turn is used to calculate the energy and the mass of the cosmic primary particle. The light produced in the air showers come from two different mechanisms, fluorescence, and Cherenkov.

2.5.1 Fluorescence light

The passing of the EAS charged particles, mostly electrons[6], through the atmosphere results in the ionization and excitation of the air molecules, mainly nitrogen, which produce fluorescence light in the ultraviolet range, $300 - 430nm$ [48]. The fluorescence photons are emitted isotropically and the shower can be represented in the observer frame as a small source of light propagates down through the atmosphere. The fluorescence yield is defined in [49] as the number of photons produced when an electron goes through one meter of air. It depends on the number of electrons in the shower and the atmospheric condition. The absolute yield as measured in dry air with electron energy of $0.85\,MeV$ is about 4.23 ± 0.20 photons per meter [49] at 760 mmHg and $15°$C.

2.5.2 Cherenkov light

The Cherenkov light is very common in the extensive air showers since most of the charged particles are relativistic. Cherenkov light is the emitted radiation when a charged particle travels through a transparent medium faster than the propagation speed of light in this medium. What happens is that the passing of the relativistic particle through the medium

---

[6]Both e^+ and e^-
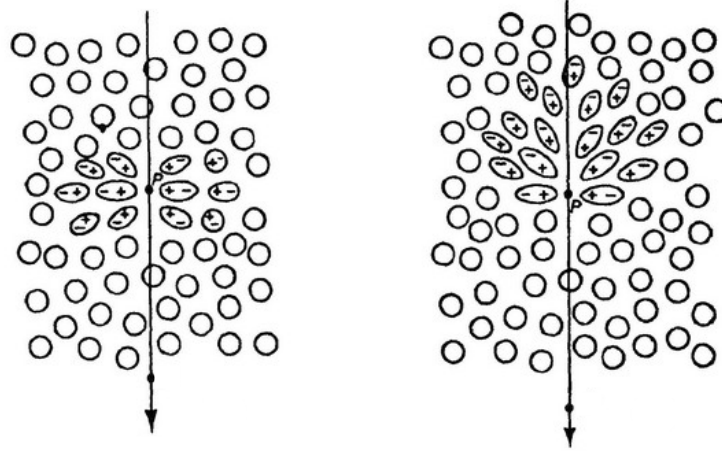
Figure 2.8: The polarization produced in a dielectric medium due to passing of left slow charged particle, at low (left) and relativistic (right) velocity, from [51].

causes a local temporary polarization along its direction. This polarization normally produces very brief electromagnetic wavelets but since the particle travels faster than the light, these emitted wavelets bunching up behind the particle and interfere constructively forming a light shock wave cone, see Fig. 2.8. A radiation in the visible and near-visible regions is emitted at an angle θ_c relative to the track of the particle. This angle known as the Cherenkov angle and is given by

$$\cos \theta_c = \frac{c}{nv} = \frac{1}{\beta n}, \tag{2.13}$$

where $v, c,$ and n are the particle, light velocities, and the refractive index of the medium respectively. In order to Cherenkov radiation to happen the particle must travel with a velocity higher than the threshold velocity, $\beta_{min} = 1/n$, which corresponding to $\theta \sim 0$. The Cherenkov angle in air is about $1.4°$ at the sea level this value decreases for higher altitudes. Depending on that one can define minimum kinetic energy of the particle or in another word the Cherenkov threshold energy as

$$E_{th} = m_o c^2 \left(\frac{1}{\sqrt{1 - n^{-2}}} - 1 \right). \tag{2.14}$$

The Cherenkov radiation yield produced by charged particle of total energy E and charge Z in a certain wavelength range is given by [50]:

$$\frac{dN_\gamma}{dX} = \frac{2\pi \alpha Z^2}{\rho(h)} \int_{\lambda_1}^{\lambda_2} \left(1 - \frac{1}{n^2(h,\lambda)\beta^2} \right) \frac{d\lambda}{\lambda^2}, \tag{2.15}$$

where $\beta = v/c$, ρ the air density at height h, $\alpha \approx 1/137$ is the fin-structure constant, and n the refractive index. This represents the photons produced in air shower with only one electron. The Cherenkov light produced in an air shower is almost at the same order as the fluorescence light signal depending on the observation angle with respect to the shower axis. Unlike the fluorescence light, Cherenkov photons are emitted in the forward direction.

2.6   Air shower simulations

The measurements of the air shower cascade are confirmed using Monte Carlo simulations of air showers. Here comes the important role of the simulation package together with
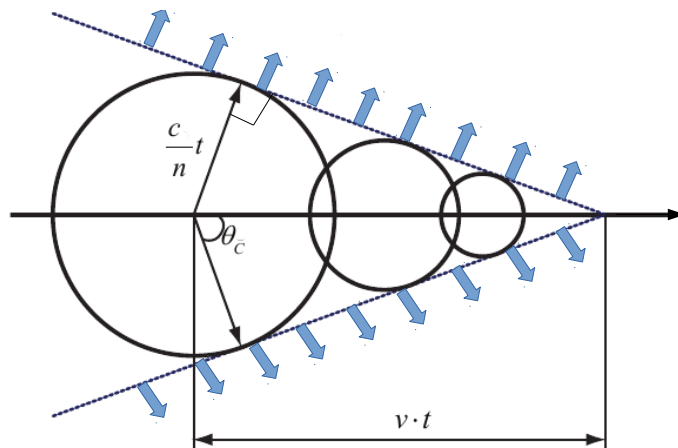
Figure 2.9: A particle travel a distance $d_p = vt$ through the medium along the black arrow producing Cherenkov radiations waves travels distance $d_w = \frac{c}{n}t$. Using simple trigonometric calculation the Cherenkov angle would be $\cos\theta_c = \frac{d_w}{d_p}$, where the wave front represents the tangent.

high-energy interaction models, which allow a reliable prediction of particle distributions in showers. The simulation software programs model the shower development in the atmosphere by simulating the interactions of the secondary particles as well as their decays and track them until they reach the ground. Such a simulation of one shower requests a long computing time which increases exponentially with the energy of the primary particle. For this, there are two approaches to reduce the time required for the simulations: first not track all the secondary particles but only after certain energy only a fraction of representatives particles are tracked, this method is known as thinning. In the second approach, the first interactions are tracked in detail then the complete development of the shower is described using tables of particles obtained via numerical solution of the cascade equations. The most important air shower simulation package using the thinning approach is CORSIKA [43], COsmic Ray SImulations for KAscade, which defined as a detailed simulation program. The amazing things in CORSIKA is the option to simulate Cherenkov light in the atmosphere which I used in this thesis as describe in Section 5.1.1. For the second approach the one-dimensional extensive air shower simulation CONEX [52] is the best option.

2.7 Mass composition from air shower observables

One of the key missing pieces in solving the cosmic rays puzzle is to know their composition. Since this will drive more information on the acceleration and propagation hypotheses. The composition of cosmic rays of energies up to 10^{14}eV is quite understandable from the direct measurements which showed that the primary particles consist mainly of $\sim 86\%$ proton, 11% helium, 1% heavier nuclei, and 2% electrons [53]. On the other hand, it is a challenge to distinguish between light and heavy compositions at the higher energies. Understanding that measuring the mass composition of primary particles through the air shower experiments is quite indirect and complicated and depend on the understanding of the shower development. The idea is based on measuring the parameters of the shower that are sensitive to the mass of the primary which then can be translated to the composition of the primaries using hadronic interaction models within the air shower simulations frame. These parameters depend on the detection type in case for the surface array detectors the observers

of interest are the particle densities, electrons and muons numbers, of air showers at ground. In this technique, they use the fact that the ratio of the muon to electron number is connected to the mass of the primary. Detail explanation is given in [54].

The most appropriate technique to infer the mass composition from the air shower is through observing the longitudinal development of the shower by recording the light, fluorescence and/or Cherenkov, emitted along the shower path. The observer of interest in this case is the depth of the atmosphere at which the deposit energy is maximum, X_{max}. In light of Heitler model as shown in Section 2.4.2 and Eq. (2.12), X_{max} is proportional to the logarithm of the mass A of the primary particle. But because of the dependence of X_{max} on the first interactions of the primary in the atmosphere which fluctuated from shower to shower, the mass composition measurement can be deduced from the distribution of the X_{max}. From the air shower modeling, it follows that for a given energy the primary with higher mass is induced shower shallower than the lighter masses. Moreover, the shower to shower fluctuation is smaller in case of the heavy primaries. Originating from this understanding, one can sample the all the observed showers into single energy bands and study the first two moments, mean and sigma, of the X_{max} distributions in each band. These first two moments of X_{max} distribution carry the information of the mass composition of the primary particle which can be translated using a generalized superposition model to the first two moments of the logarithm of the mass A distribution as [55, 56]

$$\langle X_{\mathrm{max}} \rangle = \langle X_{\mathrm{max}} \rangle_p + f_E \langle \ln A \rangle \text{ , and} \qquad (2.16)$$

$$\sigma^2(X_{\mathrm{max}}) = \langle \sigma_{sh}^2 \rangle + f_E^2 \, \sigma_{lnA}^2 \text{ ,} \qquad (2.17)$$

where $\langle \sigma_{sh}^2 \rangle$ is parameter represents the shower to shower fluctuation, $\langle X_{\mathrm{max}} \rangle_p$ is the mean X_{max} of proton showers, and f_E is energy dependent parameter expressed as

$$f_E = \xi - \frac{D}{\ln 10} + \delta \log_{10}(\frac{E}{E_o}) \text{ ,} \qquad (2.18)$$

with ξ and δ are parameters depend on the used hadronic interaction model, and D is the change of $\langle X_{\mathrm{max}} \rangle$ with the logarithm of energy $D = \frac{d\langle X_{\mathrm{max}} \rangle}{d\log_{10}(E/eV)}$ known as the elongation rate. In Fig. 2.10 the recent results of Pierre Auger Observatory for the X_{max} moments measurements using two different techniques based on the surface array detector, SD, and the fluorescence telescopes, FD, for energy shower $> 10^{17}$eV. And in Fig. 2.11 the induced $\langle \ln A \rangle$ moments in light of three different hadronic interactions models EPOS-LHC [57] ,QGSJET-II.04 [58] , and SIBYLL-2.3C [59, 60].
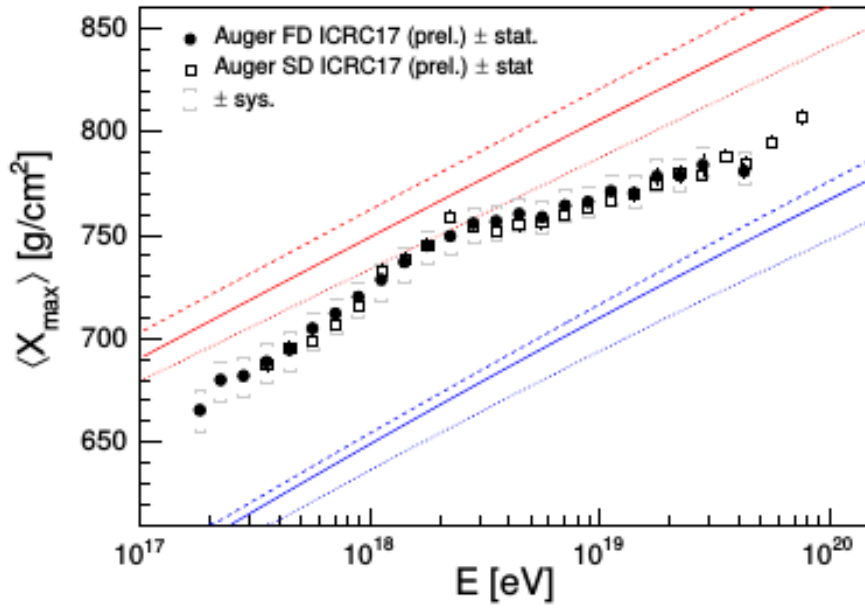
(a)
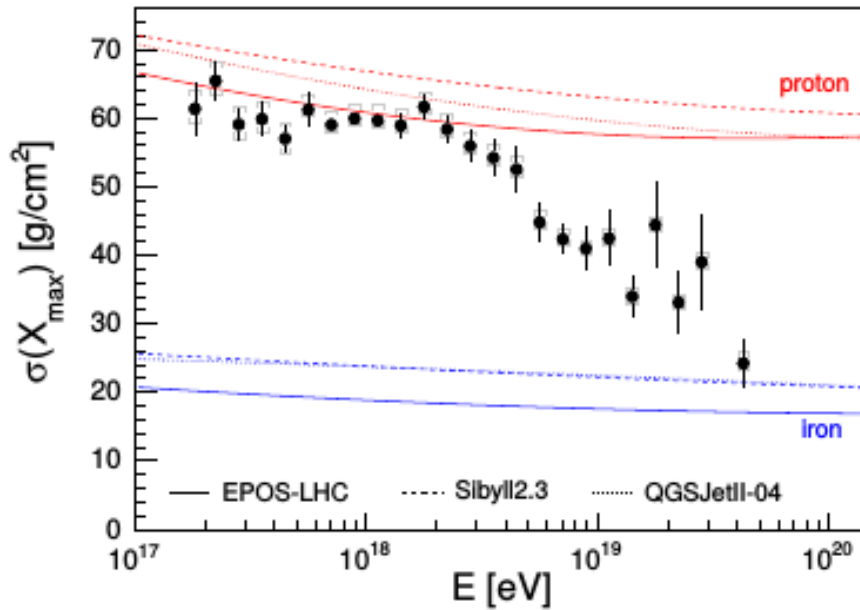
(b)

Figure 2.10: Measurements of Pierre Auger Observatory for (a) mean and (b) standard deviation of X_{max} distribution using two different techniques based on the surface array detector, SD, and the fluorescence telescopes, FD, for energy shower $> 10^{17}$ eV. The results are compared to air shower of proton (red) and iron (blue) simulated using different hadronic interaction models, EPOS-LHC, QGSJET-II.04, and SIBYLL-2.3C. Figure from [61]
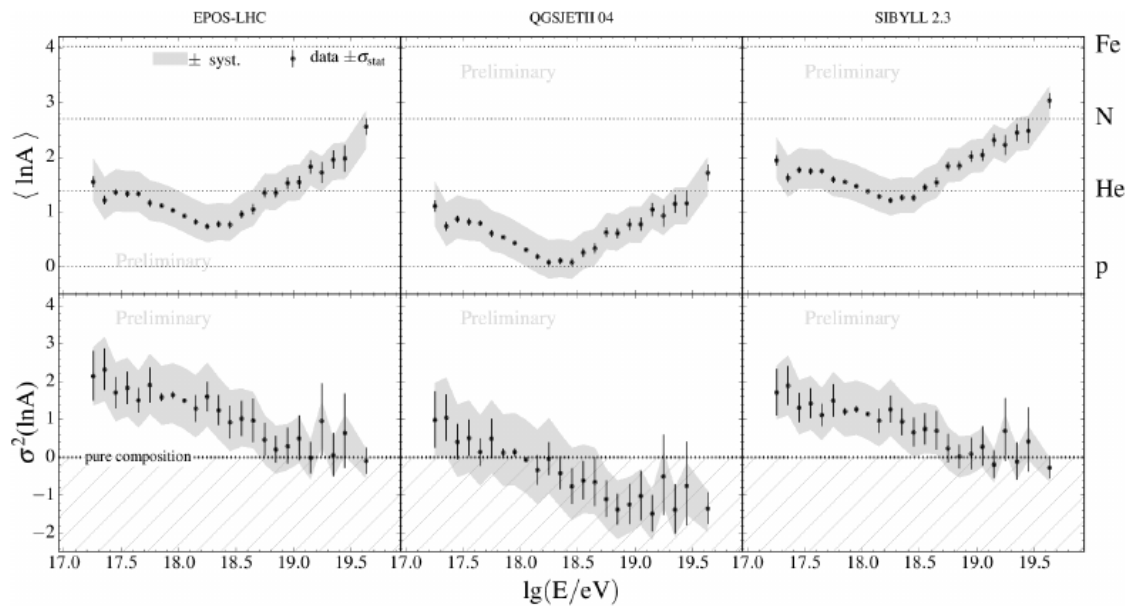
**Figure 2.11:** The mean and standard deviation of logarithmic mass,lnA, of Auger with EPOS-LHC,QGSJET-II.04, and SIBYLL-2.3C simulations. Figure from [62]

CHAPTER 3

Pierre Auger Observatory

The Pierre Auger Observatory [63], named after the physicist Pierre Victor Auger, is the largest observatory built to detect the Ultra-High Energy Cosmic Rays (UHECRs). It is located 1400 m above the sea level on north-east of the city of Malargüe, Argentina. Auger is designed, see Fig. 3.1, in a way that uses two different technique to measure the extensive air shower proprieties, e.g. energy, composition and arrival direction, over a wide range of cosmic rays energies up to $E > 10^{19}$ eV and with this study, down to $E < 10^{16}$ eV. The dual design of Pierre Auger Observatory consists of a surface detector array (SD) [64, 65] and fluorescence detector (FD) [66]. The SD measures the particle density of the air shower at the ground level using water-Cherenkov stations and FD observes the longitudinal development profile in the atmosphere using high precision cameras to image the fluorescence and Cherenkov light produced along the shower path on the dark moonless nights. This two techniques form together a complementary way to study the UHECRs. In the next sections, I will give a short overview of the SD and more details about the FD, which is directly related to this thesis.

3.1 Surface detector

About 1660 of stations, covering an area of $3000\,\mathrm{km}^2$ with 1.5 km separation distance, are grouped together forming the flat grid of the surface detector array (SD). There is a smaller array, known as Infill, with only 750 m separation distance between these stations that extend the hybrid detection sensitivity down to 10^{17}eV [63]. Each station is a water-Cherenkov detector, WCD. Each WCD is consists of a polyethylene tank filled with 12 tons of purified water, which is enfolded in a liner with a reflective inner surface. When the particles pass through the water volume they produce a Cherenkov light, which is reflected on the surface of the liner and then collected by three PMTs that observe the water volume through three windows which symmetrically located in the top of the liner. The station is self-powered by a batteries connected to two solar panels. The signal recorded by the station is emitted to the central data acquisition system of the observatory through a radio antenna mounted in a mast on the top of the tank. Each station host a GPS system on the top of the communication mast which allow the determination of event timing. The Fig. 3.2 shows an external and internal view of one of the SD stations. A more detailed description for the surface detector can be found in [63, 65, 68].
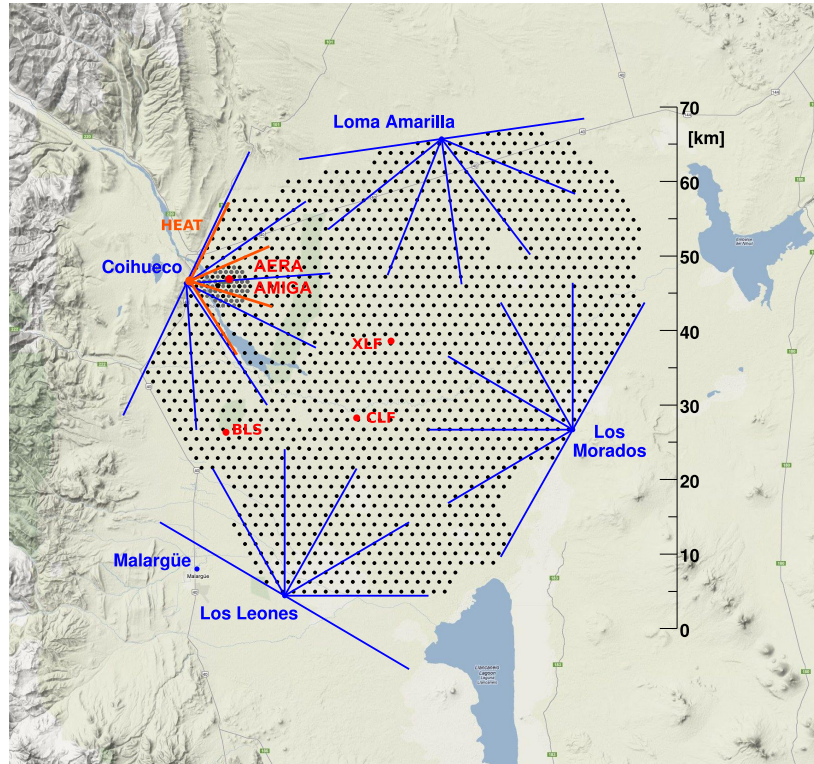
Figure 3.1: A layout of Pierre Auger Observatory. Figure from [67]. The FD standard telescopes represent by the blue lines which represented the filed of view in four sites. HEAT represented with red lines in the site of Coihueco. The black dots represents the SD stations. The position of laser facilities, CLF and XLF ,and the weather balloon launching, BLF, are represented by the red dots.

3.2   Fluoresence detector

The moment that the cosmic rays enter the Earth atmosphere they start interacting with the air molecules which in turn produce shower cascade of secondary particles. The electromagnetic component of the shower, mainly electrons and positrons caused the excitation of the nitrogen molecules and these excited molecules back to their ground state by emitting UV-photons, $300 - 430$nm, called "fluorescence light". The fluorescence light is not the only light produced in the air shower of a cosmic ray, there is also the Cherenkov light which both together describe the longitudinal profile of the shower. Pierre Auger Observatory use fluorescence detector to observe the atmosphere above the surface array. There are four FD sites are surrounding the SD array are called Los Leones (LL), Los Morados (LM), Loma Amarilla (LM), and Coihueco (CO). In each site there are six independent telescopes as an exception, Coihueco site hosts three extra telescopes. In total there are 27 FD telescopes 24 of them are the standard Auger telescopes. In Fig. 3.3 the Los Leones sites with its six telescopes can be seen.

3.2.1   The telescopes

The design of the optical system of the telescope is based on the Schmidt optics [70] which is limiting the spherical and coma aberrations [71]. A bay and the main components of the telescope can be seen in Fig. 3.4a. The bay is a clean climate-conditioned building with a circular aperture of 2.2 m radius which is optimized to limit the angular spread on the camera within

(a)
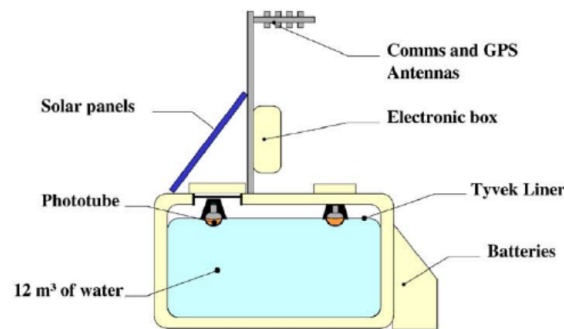
(b)

Figure 3.2: One of the SD stations in the field shown with its main components. External view (a) from [69] and schematic internal structure (b) from [68].

$0.5°$ [1]. The geometry of the optical system used in the FD telescopes is shown in Fig. 3.4b. The aperture is covered with a glass UV-transmitting filter, which functions to improve the signal by reducing the background of visible light flux. This is not the only function of the filter, moreover, it serves as a window of the bay, thus keeping the environment inside clean and climate controlled. The optical system of the telescope is outfitted with a corrector ring lens [72, 73] in order to increase the telescope aperture. The corrector lens has been designed in a ring shape of inner radius of 85 cm and outer radius of 110 cm and divided in 24 segments. This design was selected to reduce the total cost since the simulations showed that only rays beyond 85m need to be corrected [73].

The telescope mirror is a $\sim 13\text{m}^2$ spherical mirror of 3.4m radius of curvature. Such a large area mirror is reduced to segments with the aim to reduce costs and easy transportation. The segments are two configurations that represent 36 rectangular anodized aluminum mirrors and 60 hexagonal glass mirrors. Telescopes mirrors of Los Leones and Los Morados have the rectangular configuration and the hexagonal glass mirrors are used for Loma Amarilla, Coihueco, and HEAT. The two different designed used in the FD telescopes mirrors are shown in Fig. 3.5. The rays reflected on the mirror are detected by a camera of 440 hexagonal pixels located on the focal surface of the telescope converted into electric pulses every 100 ns. Each pixel in the camera is a photomultiplier tube, PMT, housed in an aluminum block shaped as an array of 22 rows by 20 columns. The corresponding field of view of each pixel is about $1.5° \times 1.5°$. The whole telescope of the standard FD telescopes has a field of view,

---

[1]One-third of the camera pixel size,$1.5°$ and corresponding to spot size of 15mm diameter due to the spherical aberration.

(a)

(b)
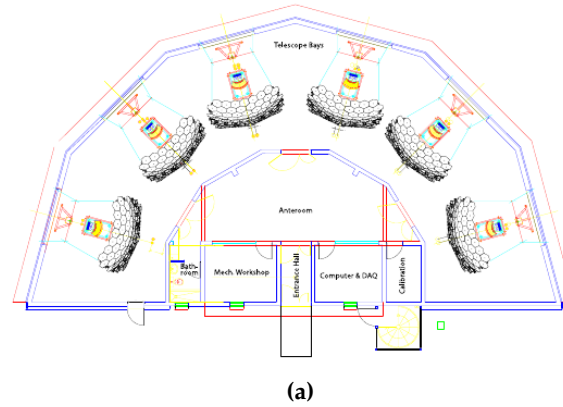
Figure 3.3: Two different view for a FD building. Schematic layout (a) with six fluorescence telescopes from [66] and a daytime photo of Los Leones FD telescopes (b) the shutters were opened for maintenance from [63].

FoV[2], of $30° \times 30°$ in azimuth and elevation. The six telescopes in each site cover a combined $180°$ in azimuth towards the SD array. In Fig. 3.6, a side picture for the FD camera and in the background the UV-filter and the corrector ring lens are very obvious.

The bay has a shutter which is opened so the light finds its way to the camera for data taking and is closed during the daytime to prevent the PMTs damage due to high exposure to light. The control of the shutters is done automatically using a remote-controlled system called "Slow Control System", SCS. The SCS operates the whole FD system from the central campus in Malargüe. The FD telescopes can take data only during the moonless nights with good weather conditions. For that reasons, the FD has only 15% duty cycle. There is a study to operate the FD telescopes during the high moonlight by reducing the PMT gain [74].

3.2.2   The High Elevation Auger Telescopes

In the frame of extending the Pierre Auger Observatory measurements down to below 10^{17}eV, three telescopes are added to the family of the FD Auger telescopes. These telescopes named the High Elevation Auger Telescopes [75], HEAT, which have a similar optical system like the 24 other Auger standard telescopes. The feature of these telescopes is the ability to be tilted by $29°$ upward using a hydraulic system. Each telescope of HEAT telescopes can

---

[2]The solid angle in which the light can be observed by the telescope. It describes in terms of the azimuth and the elevation angles in a spherical coordinate system.
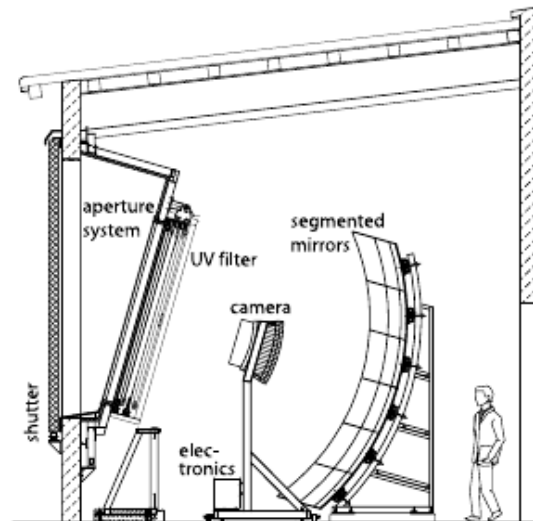
(a) A schematic layout of an FD telescope and its main components. Figure from [63].
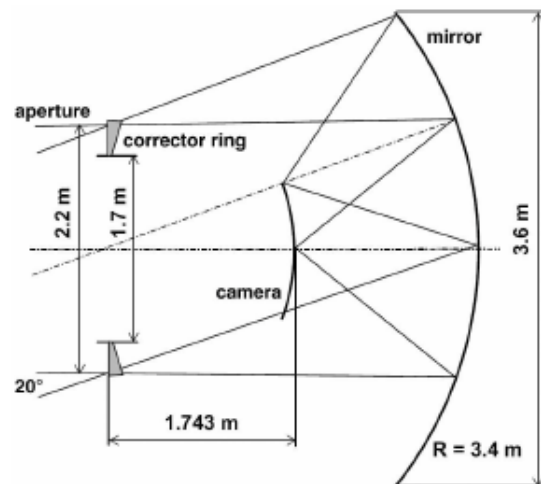
(b) The geometrical shape of the optical system used at the FD telescopes. Figure from [66].

Figure 3.4: The FD telescope optical system.

move independently, as they were installed in an individual buildings. HEAT considered as the fifth FD site is located 180 m north-east of the Coihueco site. A photographic view of the three HEAT telescopes is shown in Fig. 3.7. Another thing interesting in HEAT and makes it distinct from the standard FD telescopes its electronics are much faster, the signal can be digitized in ∼ 50ns. The main purpose for building HEAT telescopes is to detect the light production of the low energy cosmic ray showers, accordingly, the Pierre Auger Observatory measurements are extending from below the second knee up to the cutoff. The motivation to build only three telescopes looking high to the sky is the high cosmic rays flux at the energy range of interest as well as these low energy showers developed early in the atmosphere. A considerable number of events will be observed with only three telescopes. Supporting to the hybrid design of Auger, there are extra SD stations filled the region near to the HEAT, called "Infill" and "HEATLET", which allowed unbiased hybrid measurements for the cosmic rays energy spectrum and the mass compositions.
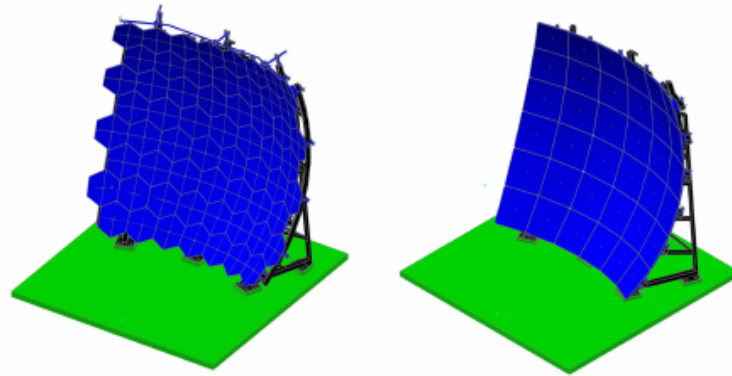
Figure 3.5: The two different segmentation configurations of the mirror used in the FD telescopes from [66]. In the right, mirror with 36 rectangular anodized aluminum segments mainly used in Los Leones and Los Morados telescopes. In the left, mirror with 60 hexagonal glass segments mainly used in Loma Amarilla, Coihueco, and HEAT telescopes.
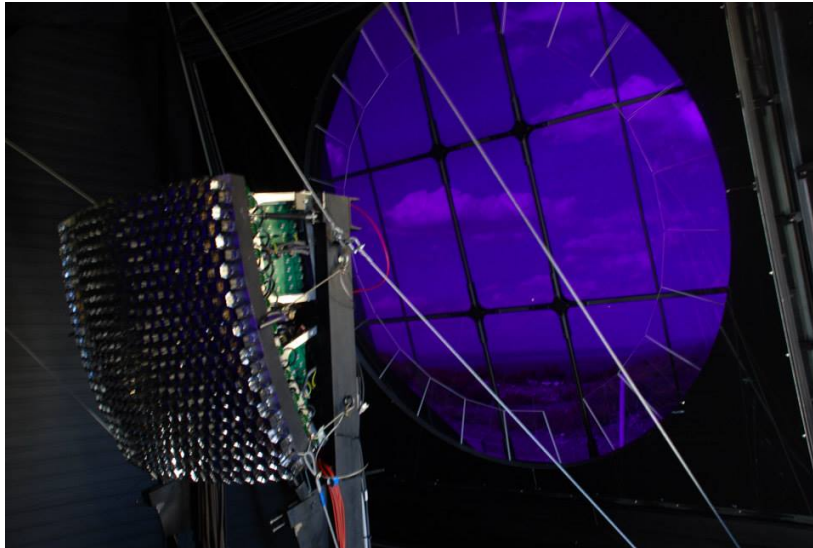
Figure 3.6: Picture for some of the FD telescope components where the camera, the UV-filter, and the annular correction lens.

HEAT has the main operation mode where its telescopes are tilted up with a field of view $30° \times 58°$[3], called "upward" mode. Moreover, HEAT also operates in the horizontal position, "downward" mode, in this mode the field of view coincides with Coihueco field of view. From this point comes the importance of this mode to use as cross-check of the agreement in the measurements between HEAT and Coiheuco. A HEAT telescope in the two operating modes "upward" and "downward" is shown in Fig. 3.8. Existence at a relative close distance to each other, HEAT and Coihueco see a significant number of coincident showers this give them the power to combine together to form a virtual FD site, "HeCo", which has a wider FoV range to measure showers with high accuracy. The virtual FD site is discussed further in Section 4.1. HEAT started taking data in September 2009 [75] and since June 2010 HEAT data is considered officially stable [76].

---

[3]There is about $1°$ of elevation between the horizontal and the field of view bottom line.

Figure 3.7: Photograph of HEAT telescopes tilted upward [77]. The first and the third telescopes with closed shutters and the shutter of the second telescoped is opened for cleaning.
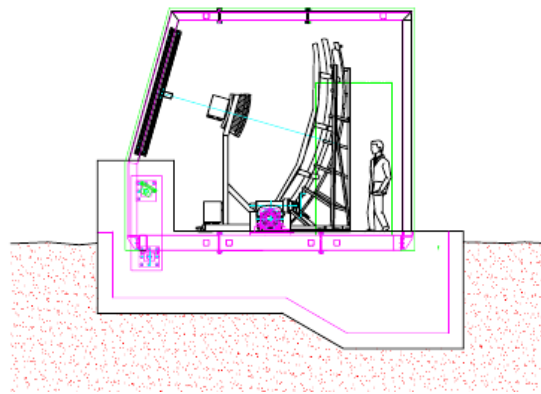
(a) Cross-calibration mode for HEAT telescopes, "downward".
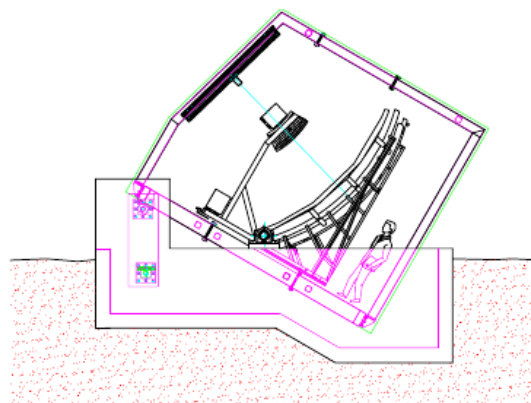
(b) The default tilting mode for HEAT telescopes, "upward".

Figure 3.8: Schematic drawing for the HEAT bay in the two possible working modes from [75].
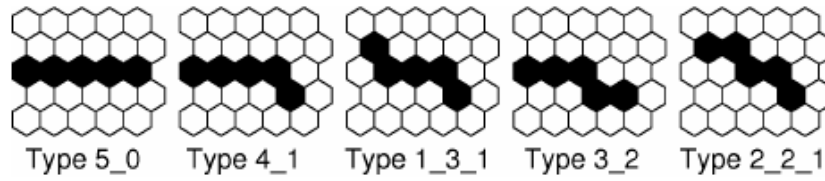
Figure 3.9: The fundamental track patterns used in the SLT. Figure from [66].

3.2.3   Trigger and data acquisition system

The FD data processing passing by a hierarchical-chain, starting from the moment when the light strikes the camera till ending with a true shower candidate for a hybrid event. The data acquisition system, DAQ, faces a big challenge to define the true shower signal in an enormous light background. Each row of the 20th rows of the camera is connected to an Analog Board, AB, to read out the data. A single row in the camera represents a channel of 22 pixels. Those ABs are part of the front-end unit, FE, where the signal is shaped, digitized[4], and triggered for the first time. The First Level Trigger, FLT, takes place on the front-end board which adjusted to produce a trigger rate of 100 Hz in each pixel. The triggered pixels of each channel is sent to the Second Level Trigger board, SLT, which searches for track segments of five pixels in length. The fundamental track patterns used in the SLT logic are shown in Fig. 3.9 also the rotations and the mirror reflections of these patterns are possible. Taking into account the reality that the track can't pass through every pixel center, four out of five pixels in the pattern must be triggered. The events of the SLT will be stored in the "MirrorPC" if they pass the Third Level Trigger, TLT, which reject the noise events caused by lightning, cosmic ray muon interacting with the PMTs, and randomly triggered pixels. The surviving data in each "MirrorPC" are sent to the "EyePC", where the FD event is built by merging the coincident events from all "MirrorPCs" data of the same FD site. The "EyePC" also generates a trigger, T3, and sends it to the Central Data Acquisition System, CDAS, in Malargüe to search for eventual hybrid events also containing the SD.

3.2.4   Calibration

Knowing the response of the PMT to a certain flux of incident light is a crucial point to determined the light flux of an air shower, needed to reconstruct the total energy of the shower. This is done by using end-to-end calibration [78] for the FD telescopes, and since the response of the PMTs continually changes, the calibration is complemented with a nightly relative calibration. There are two main types of the calibrations: the absolute FD calibration, which is long-term calibration done yearly, and the relative FD calibration, which is done two times in one operating night before and after data taking. Multi-wavelength calibration [78] is also important for FD calibration and is done using certain wavelengths to measure the response of the PMTs for them.

The absolute calibration is done once per a year or after an extended maintenance to the components of the FD telescopes. It uses a portable light source of 2.5m of diameter that is fixed on the telescope aperture in order to provide uniformly flux of light to each pixel in the camera. Knowing the flux of the used light source and the ADC[5] counts from the acquisition system, the response of each pixel is self-evidently calculated. The FD response

---

[4]The sampling rates for digitizing the signal is 10MHz, equivalent to 100ns, for the standard FD telescopes and 20MHz, 50ns, for HEAT.

[5]Analog-to-digital converter

(a) The drum is mounted at the telescope aperture for the absolute calibration.

(b) Relative FD calibration with three different positions for the light source.
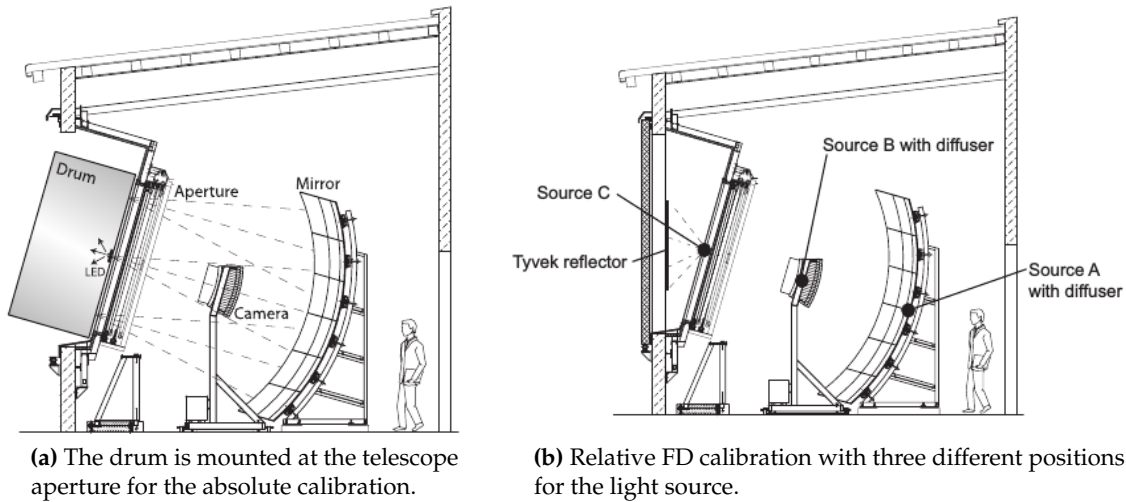
Figure 3.10: Schemes show two different techniques used for the FD telescopes calibration. Figure from [75].

is on average ~ 5 photons/ADC bin [66]. This calibration is known as the "drum calibration" because of the shape of the used light source is looking like a huge drum. UV LEDs are used to power the drum for the absolute measurement and for multi-wavelength calibration a xenon flasher is used instead. In Fig. 3.10a a schematic for the drum calibration is shown. The absolute calibration is cross-checked using a mobile laser system. The laser beam is fired vertically into the atmosphere at 4 km in front of the FD building. This method is used to cross-check the calibration of a few pixels since the calibration of the whole camera in this manner is impracticable.

The response of the telescopes changes from night to night. In order to monitor these drifts and to track the absolute calibration to reduce the systematic uncertainty, the relative calibration is used. The relative calibration is done using three illuminated points named A, B, and C which are permanently installed in each FD telescope at three different positions, see Fig. 3.10b. Point A is a diffuser at the center of the mirror powered through optical fibers from a permanently installed LED source for each FD building. Points B and C are also diffusers but illuminated from a xenon flash lamp. The diffuser-B is fixed in the camera side towards the mirror and diffuser-C fixed outside the aperture with its light directed to a Tyvek sheet in the inner face of the shutter, which reflects the light to enter the aperture.

3.2.5   Atmospheric monitoring

The atmosphere plays a major role in the indirect detection of cosmic rays. All the indirect observatories at the ground use the atmosphere as a giant calorimeter absorber. That way the variations in the atmospheric conditions will accompany with noticeable effects on the reconstruction of the air showers. Especially that the fluorescence yield in the atmosphere depends on pressure, temperature, and humidity of the air [79]. In a much simpler way than the fluorescence case, the Cherenkov yield in the atmosphere depends also on the atmospheric variations where the number of Cherenkov photons per charged particle per meter per wavelength depends only on the atmospheric refractive index and the dependence of the refractive index on the pressure and the temperature calculates analytically during the air shower reconstruction. Not only this but also the light is attenuated along its path due to scattering and absorption in the clouds, aerosols, and air molecules. For that purpose,

the Pierre Auger Observatory uses extensive techniques for monitoring the atmospheric parameters.

For determining the light attenuation due to aerosols, Auger uses two laser facilities [80] installed at central positions within the SD array: Central Laser Facility, CLF, [81] and eXtreme Laser Facility, XLF. Both CLF and XLF measure constantly the *vertical aerosol optical depth*, VAOD, profiles at the atmosphere using a calibrated UV laser beam fired directly into the sky. The scattered light from this laser beam produces tracks in the camera similar to the air shower light. And since it is expected that the laser beam is attenuated in the same way as the light of the air shower, the aerosols attenuation, T_{aer}, is deduced from the amount of laser light reaching the FD. The light scattering by the aerosols can be described by the Mie scattering theory. The light also attenuated due to scattering and absorption by the molecular air components. Ozone, O_3, is the most important absorber in the UV range and since O_3 molecules are highly concentrated in the stratosphere above the air shower measurements [82], the molecular attenuation, T_{mol}, is dominated by the scattering, which depends on the Rayleigh cross section [83]. The Rayleigh scattering can be calculated analytically for known temperature, pressure, and humidity of the atmosphere [84]. The light observed by the FD must be corrected for the attenuation both, by aerosol and molecular, using [84]:

$$I \propto T_{aer} T_{mol} I_o, \tag{3.1}$$

where I_o is the light intensity from the source. In order to calculate this correction in the reconstruction of the air shower, CLF and XLF measure the average of the VAOD profile over one hour and normalized it to reference profiles measured in aerosol-free nights. These reference night also referred as "Rayleigh nights" as the scattering is dominated by the molecular attenuation. For those nights in which the VAOD profiles are not available, a "parametric Mie model" is used [85].

At each FD site, there is a LIDAR station [86, 87], LIght Detection And Ranging, which scans the sky above the FD. This is done by shooting a UV laser beam each hour above the SD array and the backscattered light in the atmosphere is detected by the photo-receiver. Such a technique is used to estimate the vertical aerosol optical depth as well as the cloud coverage in the field of view of the FD telescope. In addition to the LIDAR system, an infrared camera mounted at each of the four FD building, using the fact that the cloud is warmer than the surrounding atmosphere and produces an infrared signal [63]. The field of view of the FD telescopes is imaged every five minutes. Moreover, cloud maps of the Pierre Auger Observatory are provided every half an hour by Geostationary Operational Environmental Satellites, GOES [88]. Monitoring the clouds above the FD telescopes is crucial since the high percentage of clouds can block the light from an air shower. For the atmospheric state variables like temperature, pressure, and humidity, are monitored on the ground using five ground-based weather stations and the Global Data Assimilation System, GDAS, or even at the atmosphere by radiosonde balloons. In Fig. 3.11 a schematic map for the atmospheric monitoring sites at the Pierre Auger Observatory is shown. More detailing of the atmospheric conditions monitoring at the Pierre Auger Observatory can be found in [84, 89–91].

3.3   Reconstruction of telescope data

The reconstruction of the observed air showers by the FD telescopes of the Pierre Auger Observatory is done in several sequenced steps. This section will discuss briefly these steps in two possible cases the FD mono reconstruction and the hybrid reconstruction. Basically, the FD reconstruction can be split into two parts the geometry and profile/energy reconstructions. The reconstruction starts with finding the pulses of the triggered pixels. The signal
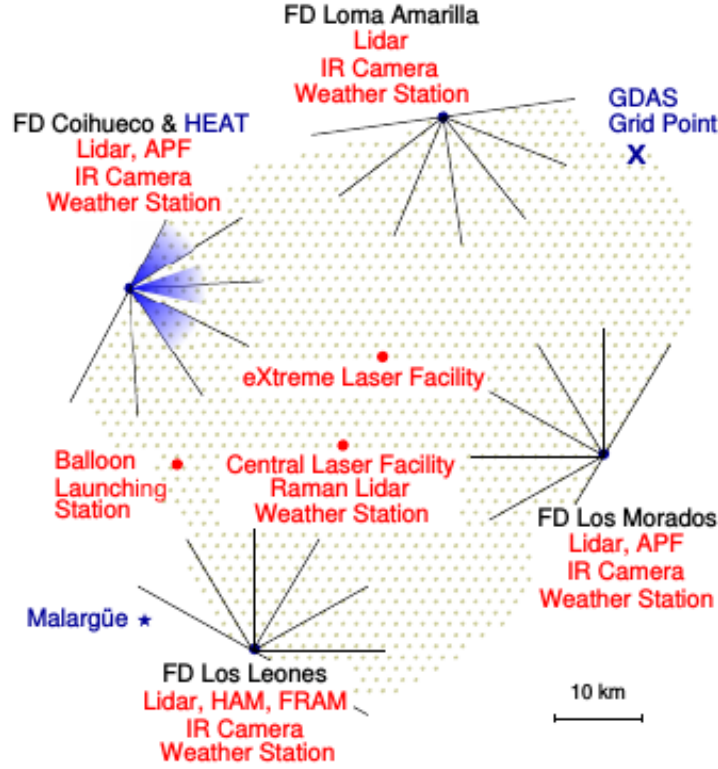
Figure 3.11: schematic diagram for the Pierre Auger Observatory atmospheric monitoring sites. Figure from [63].

to the noise ratio must be greater than 5, in order to accept these pixels in the geometrical reconstruction. Each pixel has a pointing direction and covers a small solid angle of the sky. In case of the angle between a pixel direction and the other lighted pixels is greater than $5°$, this pixel is considered isolated and has a random signal not part of the shower and is rejected in the reconstruction.

3.3.1 Geometrical reconstruction

The geometrical reconstruction is beginning by finding a plane containing both the FD eye position and the shower axis line, which is known as the Shower Detector Plane, SDP, see Fig. 3.12. The SDP is defined by the position of the eye and the two angles Θ_{SDP} and Φ_{SDP} which determined a normal vector to the SDP plane called the SDP vector. The next step is to define the position and the orientation of the shower axis within the SDP. This is done by determining the parameters of the shower axis: R_p, the perpendicular distance from the detector to the shower axis, χ_0, the angle of the shower axis inside the SDP, and T_0, the time in which the shower passes the R_p position. These three variables represent the free parameters of the fit function of the time development of the light in the camera,

$$t_i = T_0 + \frac{R_p}{c} \tan(\frac{\chi_0 - \chi_i}{2}), \tag{3.2}$$

where t_i is the arrival time of the light from the shower at the ith pixel with angle inside the SDP plane χ_i. A χ^2 minimization is used to determine the best shower axis parameters. In this step and depending on the timing information used the FD reconstruction split into two different types of reconstructions namely: FD monocular reconstruction, and hybrid reconstruction.

Monocular geometry

In the mono FD reconstruction only the timing information from the triggered pixels is used and in this case the χ^2 function is

$$\chi^2_{\text{mon}} = \sum_i (\frac{t_i - t_i^{exp}}{\sigma_{t_i}})^2, \tag{3.3}$$

where t_i and t_i^{exp} are the measured and expected arrival time respectively and σ_{t_i} is uncertainties of the arrival time measurements in i$^{\text{th}}$ pixel. From this fit, the shower will be reconstructed geometrically but the uncertainties of the reconstructed shower axis parameters can be significant if the shower has a constant angular speed along its track. In this case, the track of the shower is usually short, which means that the range of the angles is not sufficient to describe the curvature of the tangent function, Eq. (3.2), and the fit drops into a line. For that reason the monocular reconstruction is limited reconstruction in accuracy to reconstruct the shower axis. Because of this monocular geometry is not used in Auger for any physics analysis.

Hybrid geometry

To overcome the limited accuracy of the monocular reconstruction an additional time information is needed, which can be found in the SD array. Using the arrival time of the shower core at the ground from the nearest SD station will constrain the time fit within the SDP and reduce the uncertainty in the geometry reconstructed parameters. In this case the χ^2 function contains two term, FD timing term and SD timing term, which is given as

$$\chi^2_{\text{hyb}} = \sum_i (\frac{t_i - t_i^{exp}}{\sigma_{t_i}})^2 + (\frac{t_{SD} - t_{SD}^{exp}}{\sigma_{t_{SD}}})^2, \tag{3.4}$$

where $\sigma_{t_{SD}}$ is the uncertainty in the arrival time at the SD station. In Fig. 3.13a an example of a shower reconstructed by the hybrid and the monocular reconstructions and the values of the shower axis parameters in both cases. The correlation between χ_0 and R_p can be seen in Fig. 3.13b for both hybrid and the monocular reconstructions.

3.3.2 Reconstruction of the longitudinal profile and energy

After the geometrical construction, the shower energy reconstruction is performed. This is possible by disentangling the contributions of light produced by the fluorescence and the Cherenkov effects to the light collected at the aperture with consideration of scattering and attenuation of the light in the atmosphere. The number of photons per unit time is known as the light profile of the shower, which can be converted to the longitudinal profile, the energy deposit per unit slant depth. In Fig. 3.14 an example for the light profile and energy profile can be found. The longitudinal profile is extrapolated using Gaisser-Hillas function [94] to describe the whole shower longitudinal development. From the Gaisser-Hillas, GH, fit:

$$f_{GH}(X) = (dE/dX)_{\text{max}} \cdot (\frac{X - X_0}{X_{\text{max}} - X_0})^{(X_{\text{max}} - X_0)/\lambda} \exp((X_{\text{max}} - X_0)/\lambda), \tag{3.5}$$

X_{max} and energy of the shower is found where $(dE/dX)_{\text{max}}$, X_{max}, X_0 and λ are the free parameters of the fit, which can be fixed to certain values to improve the reconstruction. The calorimetric energy of the shower is the integration of the extrapolated Gaisser-Hillas function:

$$E_{cal} = \int_0^\infty dX f_{GH}(X). \tag{3.6}$$
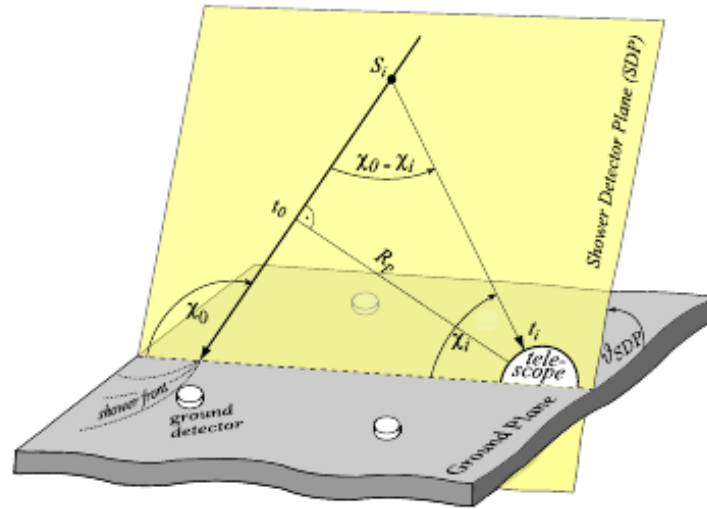
Figure 3.12: Illustration of the shower detector plane and the geometrical shower reconstruction parameters. Figure from [92].

Shower universality profile constraint

At lower showers energies the measured profile get very short providing little data to constrain the GH profile. In this section I will give a summary of the new constraint added to the FD reconstruction from the hypothesis of air shower universality [95, 96], which is also known as "*k*-constraint" to add additional stability where needed. This addition constraint is added to the Gaisser-Hillas fit in order to improve the reconstruction energy bias of the showers below 10^{18}eV. The universality factor k is given as:

$$k = \mathrm{E}_{\mathrm{cal}}/(dE/dX)_{\mathrm{max}}. \tag{3.7}$$

In Fig. 3.15a the *k*-constraint values as function of X_{max} are shown for all track lengths and high-quality tracks longer than $600\mathrm{g/cm}^2$, which shows that the k is almost constant for long track length. The values of this additional constraint parameter is added to the reconstruction for mixed composition, 50% proton plus 50% iron, with taken into account the difference between the simulated interaction models, see Fig. 3.15b.

3.4 Profile Constrained Geometry Fit

The hybrid reconstruction of the showers with energies less than 10^{17}eV is not possible and now geometry reconstruction does not yield acceptable accuracy. These showers are observed at very close distance to the telescopes, so there is no available information from an SD station that can be used for hybrid reconstruction, SD is not triggered. This leaves us only with the FD based reconstruction. But the pure-timing fit of the mono reconstruction performs an unreliable shower geometry for too short track lengths, which is the main feature of these low energies showers. The profile constrained geometry fit, PCGF, reconstruction was first applied at HiRes-I [98] to measure the energy spectrum of ultra high energy cosmic rays. A custom PCGF version is used here. The X_{max} in case of HiRes-I is fixed for certain values and is not free parameter to be fit like our case.

The PCGF was proposed to reconstruct the low energies showers observed by HEAT. The idea in PCGF is that the profile is used to contain the geometry of the shower by also
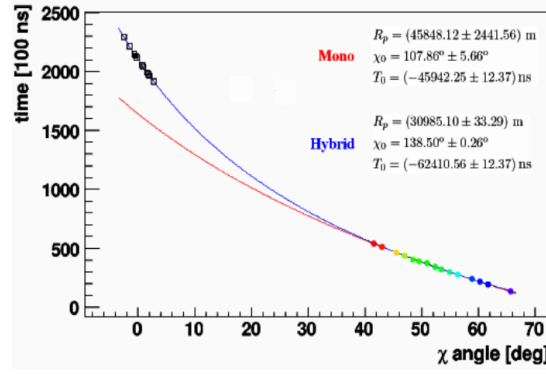
(a) the time-angle correlation for the same event in hybrid reconstruction (blue fit) and the monocular reconstruction (red fit). The squares indicates the SD station and the color points are the measured FD data which are color coded depending on the arrival time from early (purple) to late (red). Figure from [92].
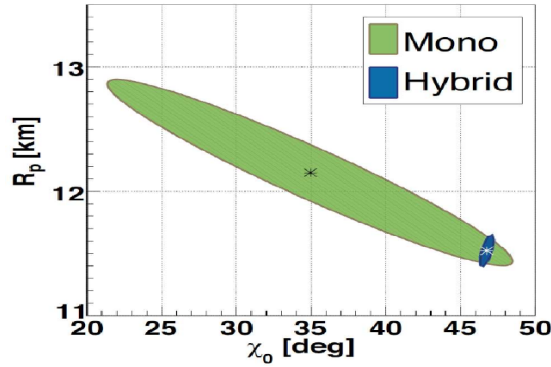
(b) The reconstructed values of R_p and χ_0 of the shower axis for mono and hybrid reconstruction the shaded regions represents the uncertainty. Figure from [93].

Figure 3.13: Comparison of the hybrid and the monocular reconstructions.

do profile reconstruction, GH-fit for trial geometries then combined the timing χ_t^2 and the profile χ_{GH}^2 and minimize the sum to pick up the best geometry. The PCGF reconstruction starts like the standard FD mono or hybrid reconstruction by finding the SDP, then the PCGF model starts to play its rule of finding the best shower axis. First the light is calculated at the aperture independently of the shower geometry then χ_0 is scanned $1°$ step in the range $10°$ to $170°$ or alternatively to this fixed range a pre-scan can be preformed with $4°$ for finding the range of χ_0 for the main scan. This pre-scan will shorten the time needed for the main scan. Using the linear regression of the time fit, Eq. (3.2), R_p and T_0 are calculated. These trial geometries are used to perform a profile reconstruction with GH-fit, Eq. (3.5), the four parameters of the GH-function are all fitted without constraining for better $X_{\max}$ calculation. The minimum of the profile fit is calculated and for the best combination of timing and profile fit the shower axis is reconstructed. After that the reconstruction is continued as in the standard way. The steps for finding the best shower axis are done within one module in $\overline{\text{Off}}\underline{\text{line}}$ called "FdProfileConstrainedGeometryFit". The configuration of the PCGF as it used in this work can be found in Appendix A. In Fig. 3.16 the best χ_0 for the minimum combined χ_{GH}^2 of timing fit and profile fit is shown as red square.
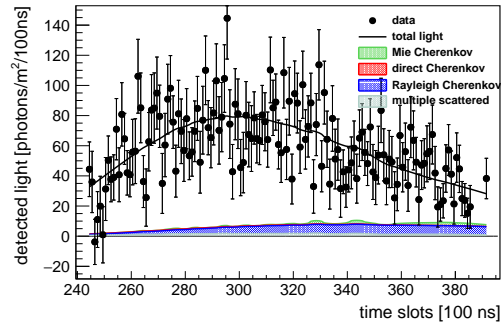
(a) The light profile and its composition.
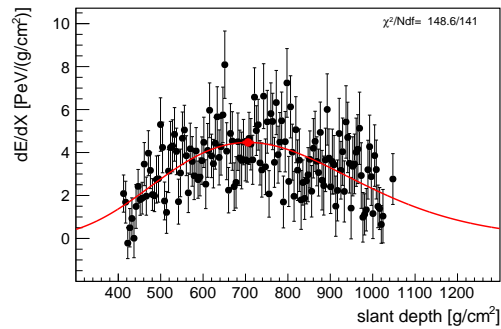
(b) The longitudinal shower profile with Gaisser-Hillas fit the red line and the red dot refer to the reconstructed $X_{\max}$ position.

Figure 3.14: Example for FD event light and energy profiles.

It is one aspect of this thesis to contribute to improve the PCGF reconstruction used in Auger and to test and optimize its performance. One important result is the first general reconstruction of the full Auger dataset from 2012 to 2015 that was produced for the entire Auger Collaboration in ADST[6] data format.

---

[6]Auger data summary tree
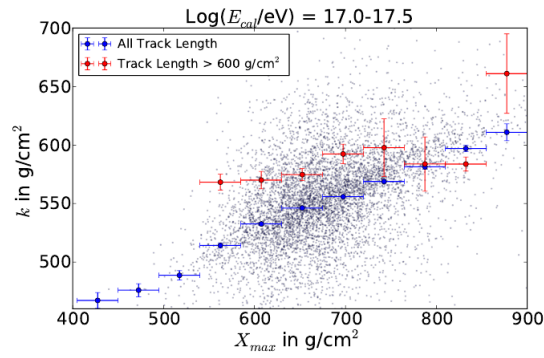
(a) The mean values of *k*-constraint as function of X_{max} in the energy range log(E/eV) $17.0 - 17.5$. The blue points represent all events and the red ones are only events with track length more than $600g/cm^2$.
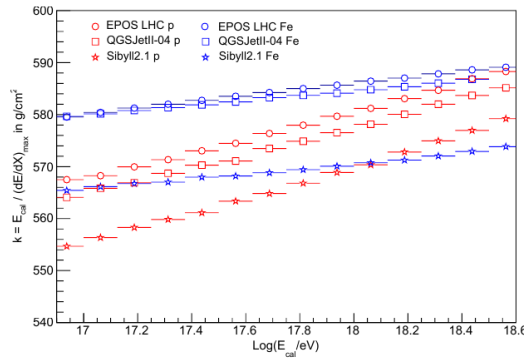
(b) The mean values of *k*-constraint in different energy bins for different proton and iron simulations using three different interaction models.

Figure 3.15: The universality factor *k* as function of X_{max} and calorimetric energy. Figures from [97].
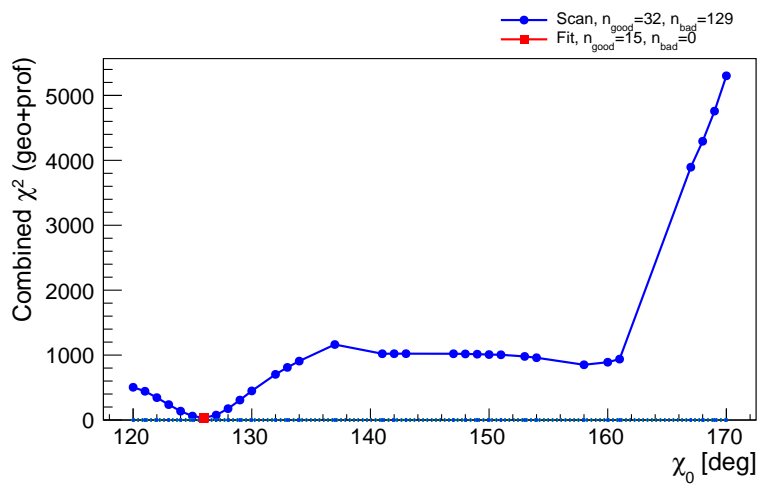
Figure 3.16: The shower axis scan in PCGF reconstruction. The best values at minimum χ^2_{GH} of timing fit and profile fit.

CHAPTER 4

HEAT-Coihueco cross-calibration

This chapter describes the process of cross-calibration of reconstructed data of HEAT and Coihueco data with different shower-reconstruction techniques. Where it pours into two important branches. The first, is the cross-check of the agreement in mass composition (X_{max}) and the energy between HEAT and Coiheuco. This is a significant step for studies using merged data from both eyes. For that part, I use two versions of standard hybrid reconstructions. Another aspect of that is to measuring the detection resolution for the showers reconstructed with PCGF[1], which it has a direct action on the results of my thesis.

Each telescope of HEAT can move independently in two positions "upward" or "downward", read section 3.2.2 for more details about HEAT operation. Upward is the default operating mode, which extend the FoV[2] of Coihueco bays (3 & 4 & 5) from $30°$ to $60°$ in elevation (Fig. 4.1a). This tilting allows the extent of Auger energy range down to 10^{17} eV and below. For special calibration runs HEAT can be tilted downward for full overlap with Coiheuco FoV. Fig. 4.1b give an illustration of the overlapping FoV of HEAT in downward and Coiheuco by an example of HeCo event with an average energy of 9.15×10^{17} eV.

4.1 HEAT-Coihueco virtual eye

Being at nearby locations from each other, HEAT and Coihueco share a lot of triggered showers. So the combination of measurements will result in extending the field of view with a high quality of GH[3] fit. By combining both HEAT and CO[4] telescopes this effectively introduces a new eye "HeCo[5]" of a virtual type with nine telescopes: 1 to 6 from CO and 7 to 9 from HEAT. The combination of HEAT and CO is ideal to measure showers between $10^{17} - 10^{18}$ eV for which purpose, HeCo data is reconstructed using standard hybrid reconstruction algorithms [76]. One main problem with this approach is that energy scale differences between HEAT and CO are directly shifting the profiles in a systematic way. Thus, the cross-calibration of HEAT and CO is in particular important for the combined measurement. Fig. 4.2 shows the track on the camera and the longitudinal profile with the G-H fit for a HeCo event with an energy of 4.7×10^{17} eV.

---

[1]Profile constrained geometry fit

[2]Field of view

[3]Gaisser-Hillas

[4]Coihueco telescopes

[5]HEAT + Coihueco merged telescopes

(a)

(b)
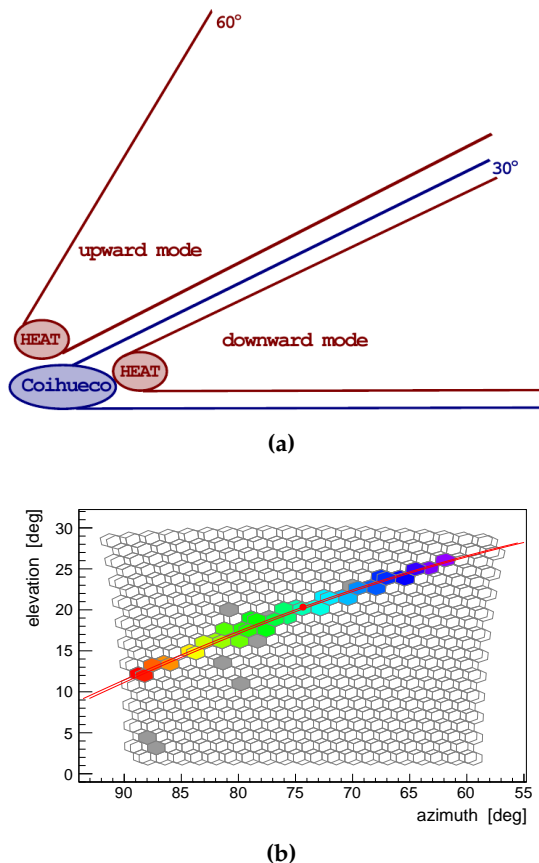
Figure 4.1: (a) Layout describing the field of view of HEAT in upward and downward modes compared to Coihueco. (b) An event in HeCo mirrors 3 & 7 which are mirror 3 from CO and 1 from HEAT.

4.1.1   HEAT campaigns in downward mode

When HEAT is tilted up it has the power to detect closer (low energies) showers as well as participated in producing HeCo events. However, HEAT in a downward mode is not less important. It has the identical field of view as Coihueco, which give us the ability to check the agreement between HEAT and Coihueco. This kind of cross-calibration has a big advantage as it uses the air showers themselves to calibrate the eyes, not others artificial sources of light as well as it does not need any complicated arrangements. Such data was already in the past used to cross-validate standard hybrid reconstruction algorithms [99]. With respect to the previous analysis there is now more HEAT downward campaigns, March and November 2014 [100], available increasing the statistics by $\approx$ 33%. Table 4.1 shows the periods in which HEAT was in the downward mode. Furthermore, a new reconstruction was produced recently by introducing an additional constrained (universality k-constraint) in the profile reconstruction see section 3.3. The cross-calibration is performed for the reconstruction with and without k-constraint.

4.2   Event selection and procedures

The first part of this analysis is using HeCo Auger-Observer reconstruction ADST files v11r0 produced with the $\overline{\text{Off}}\underline{\text{line}}$ software framework of the Pierre Auger Observatory [101, 102]

(a)

(b)
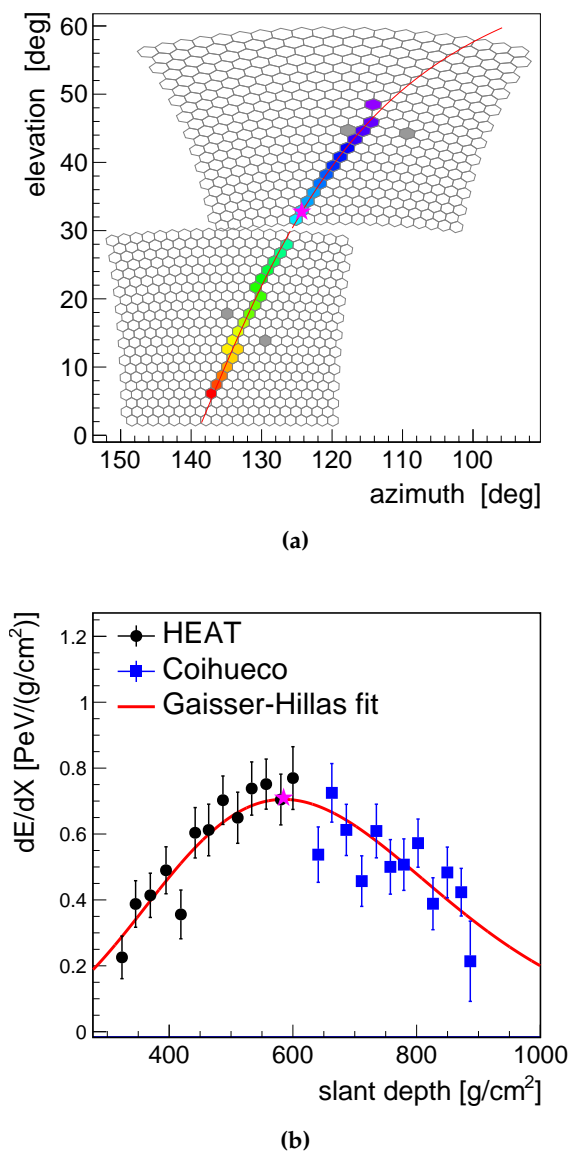
Figure 4.2: HeCo reconstructed event (a) camera view and (b) longitudinal profile with GH fit. The magenta star in both panels indicates the X_{max} position. Figures from [62]

Table 4.1: HEAT in downward mode. Shown are all available dates ta*k*ing campaigns.

Year	Month
2010	March & June & July & August
2011	August
2012	March
2013	January
2014	February & March & November
2015& 2016 & 2017	No HEAT downward
2018	March

v3r3p2-ICRC[6]-2015 [103]. Thus data are including the universality *k*-constraint. Monte Carlo

---

[6]International cosmic ray conference

simulations are produced with $\overline{\text{Off}\underline{\text{line}}}$ version v2r9 after ICRC-2013 before introducing the universality *k*-constraint, which is the same as used in Alessios Porcelli's analysis in 2013. It is a special MC production in which HEAT is reproduced in the downward mode.This MC has produced specifically for this type of cross-calibration. This MC library contains simulated showers in the energy range $10^{17} - 10^{20}$ eV using a spectrum index -2.7 using CONEX with SIBYLL-2.1 [104] as hadronic interaction model for a mixture of primaries half proton half Iron. For comparison purposes, the same analysis has been done again but with using HeCo ADST files v10r0 the same as used in ICRC-2015 [103], before introducing the *k*-constrained technique in the reconstruction. Both sets have the same time range from March 2010 till November 2014. The agreement with Coihueco has been studied for both the energy and X_{max}. For this analysis only events seen in both Coihueco and HEAT when HEAT was in downward mode are used. All the event selections used in this analysis are listed in Table 4.2. The atmospheric conditions are the same for Coihueco and HEAT, thus, the atmospheric cuts are not important. The difference in X_{max} and energy are measured as follows:

$$\Delta X_{\text{max}} = X_{\text{max}}^{\text{CO}} - X_{\text{max}}^{\text{HEAT}} \tag{4.1}$$

$$\Delta E(\%) = \frac{E^{\text{CO}} - E^{\text{HEAT}}}{\frac{E^{\text{CO}} + E^{\text{HEAT}}}{2}}. \tag{4.2}$$

Table 4.2: Event selections in ADST analysis format (adst cuts version: 1.0).

Cut name	Cut value	Meaning
eyeCut	111000	Select HEAT, CO& HeCo
!heatOrientationUp		Select HEAT downward showers
# hardware status cuts:		
badFDPeriodRejection		Reject events in bad periods
skipSaturated		Skip events that saturated the PMT camera
noBadPixelsInPulse		Reject events with bad camera pixels
# hybrid geometry cuts:		
maxZenithFD	85	Cut the up going and horizontal events
minLgEnergyFD	1.e-20	Reject the failed reconstructed events
maxCoreTankDist	1500	Reject events whose cores are > 1.5 km from SD station
maxVAOD	0.1	Vertical Aerosol Optical Depth below 0.1
minPBrass	0.9	Trigger probabilities for primaries (P & Fe) above 90%
maxPBrassProtonIronDiff	0.05	Difference between P and Fe trigger probability < 5%
# quality cuts:		
XmaxErrorLessThanXmax		
maxDepthHole	30.	Max gap in the slant depth < 30 % of the whole shower track
profileChi2Sigma	4. -1.2	Reject events with low quality fit results
# FoV cuts:		
xMaxObsInExpectedFOV	40 20	X_{max} reconstructed in expected FoV

4.3 Coihueco versus HEAT-downward results

Fig. 4.3 shows the difference between HEAT in downward mode and Coihueco in $X_{\max}$ and energy in percentage for both data and simulations. For $X_{\max}$ (Fig. 4.3a) we see a bias of $\approx 0.6 \pm 1.6 \mathrm{g/cm^2}$ and resolution $(RMS/\sqrt{2}) \approx 28.3 \mathrm{g/cm^2}$ at 5.6×10^{17} eV. Also $\Delta X_{\max}$ showed stability over a long range of energies as shown in Fig. 4.4. In case of energy (Fig. 4.3b) Coihueco shows about 8.1% higher energy than HEAT. In previous analysis [99] the observed energy shift (2010 - 2013) was just 5.3%. Using k-constraint reconstruction restricted to the same time period (2010 - 2013) we find just 3.5%.

In order to understand this shift in energy, I study the changes of the energy and $X_{\max}$ over time, see Fig. 4.5. In Fig. 4.5a the dependence of $\Delta X_{\max}$ versus time is shown. No significant time dependence is seen. This analysis also shows that the energy shift does change with time. From Fig. 4.5b it is clear that HEAT events measured during 2014 have about $19\% \pm 1.1\%$ lower energy than events from Coihueco and this was the main reason of the increased global shift. Such energy shifts are very importent for the reconstruction of combined HeCo events down to 10^{17}eV, since it directly affects the observed longitudinal profile.

This large difference in the reconstructed energies between HEAT and Coihueco during 2014 can be attributed to different FD optical response due to cleaning of optical elements of the telescopes. According to the FD cleaning list all Coiheco UV filters were cleaned on 17th March 2014 while HEAT was cleaned only on 3rd February 2015 [105]. The light can be scattered and absorbed by the dust layer in the filters, which can explain our observation. Just for clarification how much the effect could be before and after cleaning the filters see Fig. 4.7 [106]. Don't forget that HEAT most of the time tilted upward, which translated to an increased dust accumulation.

To show the advantage of the new k-constraint in the reconstruction, $\Delta X_{\max}$ and the energy difference have been analyzed without this constraint. Fig. 4.6 shows the difference between HEAT downward and Coihueco for $X_{\max}$ and energy before including the k-constraint to the reconstruction. Here only 517 events are selected instead of 621 in case of reconstruction with k-constrained universality. As well as increasing the measured shift in energy to about 9.2%.

In conclusion, the improved reconstruction found $\approx 20\%$ more events and also a decrease in the measured shift in energy by about 2%. That is to say, higher reconstruction efficiency coupled with a reduced incompatibility bias between HEAT and CO in both $X_{\max}$ and energy were the features with k-constrained reconstruction. Regardless, the measured shift in the energy there is a good agreement between HEAT and CO in $X_{\max}$ moreover there is a harmonization between data and MC. For the energy shift,on the other hand there must be a time dependent correction factor to correct CO energy to HEAT energy. HeCo reconstruction needs to take into account a correction factor connected to the cleaning schedule of the telescopes optical components. Not only that but also perform another HEAT downward campaigns or maybe even regularly in order to monitor these effects. Come to mention that there was a HEAT downward campaign in March 2018 as a result of this study. Furthermore, the time dependence correction suggested by this study was used by Auger collaboration to improve HeCo reconstruction [107]. Fig. 4.8 shows the so called "HEAT calibration" a fitting parameter in the HeCo profile fit as function of time. The black dots are the energy ratio between HEAT in downward mode and CO same as used in this study. The blue and red dots are additional measurements using HEAT downward and upward respectively. HEAT calibration time dependence fit (the blue line in Fig. 4.8) heavily changes with the mirrors and filters cleaning. The impact of including this parameter to the fit seen clearly in Fig. 4.9b where the HeCo mean $X_{\max}$ shows good stability over time. By contrast, Fig. 4.9a HeCo
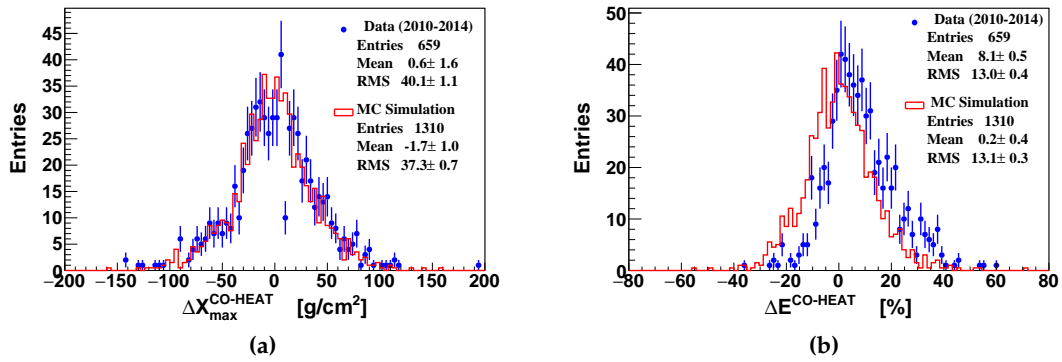
Figure 4.3: Comparison between HEAT in downward and Coihueco for both data (*k*-constrained reconstruction) and MC (before *k*-constrained reconstruction) (a) difference in $X_{\max}$ and (b) Energy difference.
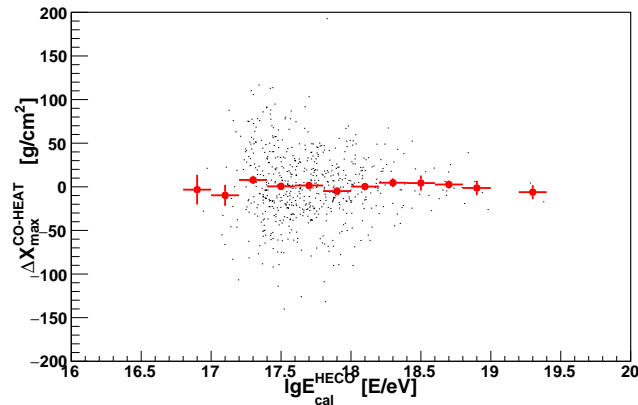
Figure 4.4: The stability of $\Delta X_{\max}$ as measured with HEAT downward data as a function of the energy with hybrid standard reconstruction.
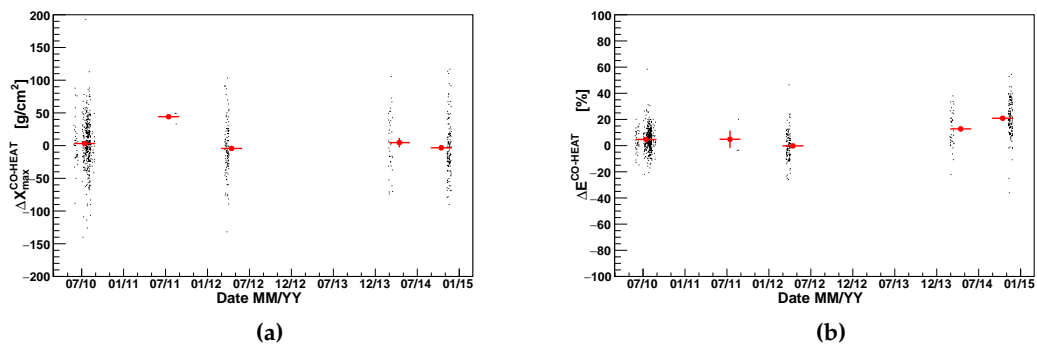
Figure 4.5: The difference between HEAT in downward and Coihueco reconstructed with *k*-constraint over time for (a) dependence of $\Delta X_{\max}$ with time and (b) the energy difference over time.

mean $X_{\max}$ swings over time. The HeCo showers used in Fig. 4.9 are the showers, which triggered in both eyes.
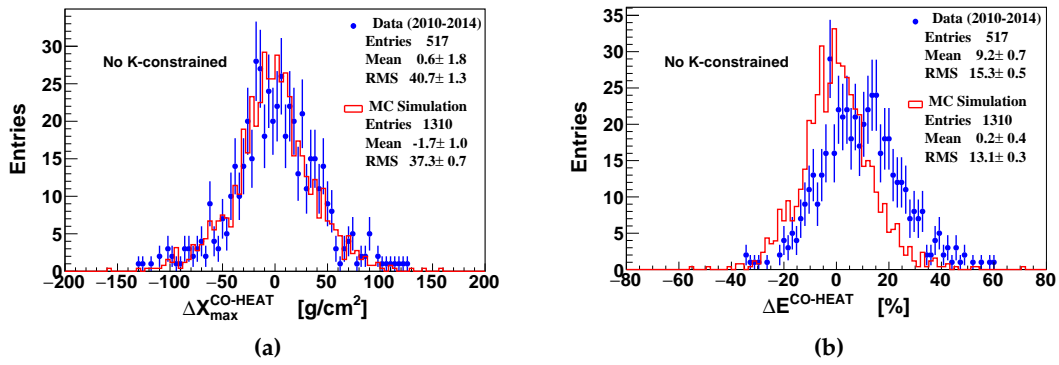
Figure 4.6: The difference between HEAT in downward and Coihueco with no *k*-constraint for (a) $\Delta X_{\max}$ and (b) energy difference.
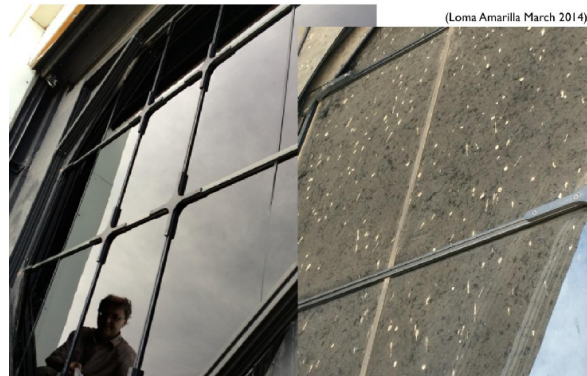
Figure 4.7: A picture of the UV filter of Loma Amarilla in March 2014 before (right) and after (left) cleaning. Figure from [106].
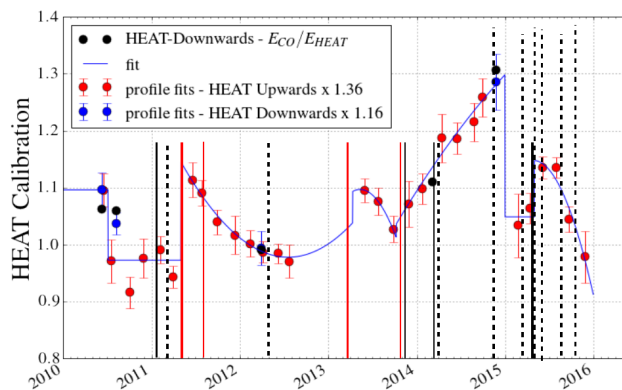
Figure 4.8: HEAT calibration time dependence function (the blue line). The vertical lines indicate calibration related (red) and mirror/filter cleaning (black) activities in CO and HEAT. Solid lines are for CO and dashed lines are for HEAT. Figure from [107].
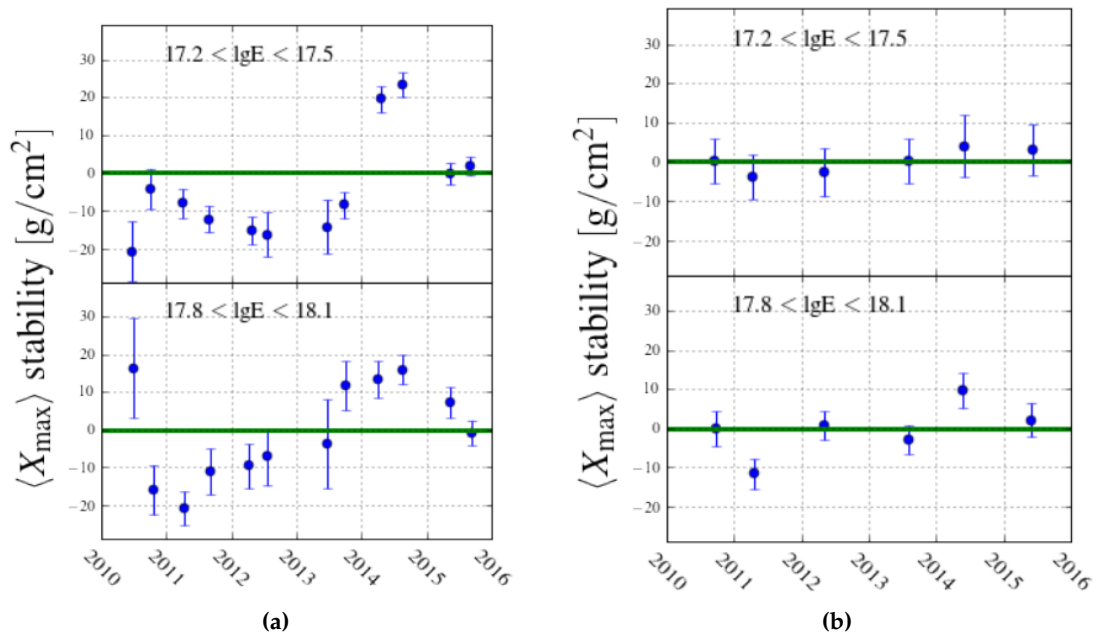
Figure 4.9: Stability of $\langle X_{\mathrm{max}} \rangle$ as a function of time at different energy ranges (a) before and (b) after the HEAT calibration function has been implemented in the $\overline{\mathrm{Off}}\underline{\mathrm{line}}$. Green lines represent the average $\langle X_{\mathrm{max}} \rangle$. Figure from [107].

4.4 Coihueco versus HEAT-downward from PCGF aspect

Now coming to the second part of this study, which is the calculation of detector resolution for the PCGF reconstruction using the data and compare this value with what we get from the RealMC, see Section 7.2. For that part I applied different selections described in Table 4.3, which doesn't contain any hybrid cuts as PCGF is mono reconstruction see section 3.4. The reconstruction and the selection cuts same as those used in RealMC only one difference that here I did not cut on the Cherenkov fraction to keep more statistics. The notable difference between the hybrid standard reconstruction with k-constraint and the PCGF, is that in case of PCGF we gained 80% more reconstructed shower. This is due reconstruction more Cherenkov showers with PCGF especially at energies less than $10^{17.4}$ eV. The PCGF shows small shift $\approx -2.2 \pm 0.8\%$ in the energy between Heat and Coihueco. But this reconstruction was done using recent version of $\overline{\text{Offline}}$ software than the one shown in Fig. 4.3 with about 2 years time gap. For $\langle X_{\max} \rangle$ the PCGF has only bias of $\approx -1.1 \pm 3 \text{g/cm}^2$ and the resolution is $(RMS/\sqrt{2}) \approx 75.4 \pm 3 \text{g/cm}^2$ at average energy $10^{17.6}$ eV. In Fig. 4.11 the biases in the HEAT reconstructed $X_{\max}$, energy, and $X_{\max}$ resolution are plotted in energy bins, each bin has at least 20 showers. The resolution increase dramatically in Fig. 4.11c for high energies which indicate that PCGF work quite well but only with rich Cherenkov showers.

Table 4.3: Event selections applied on PCGF in ADST analysis format (adst cuts version: 1.0).

Cut name	Cut value	Meaning
eyeCut	11000	Select HEAT, CO
!heatOrientationUp		Select HEAT downward showers
badFDPeriodRejection		Reject events in bad periods
skipSaturated		Skip events that saturated the PMT camera
noBadPixelsInPulse		Reject events with bad camera pixels
maxZenithFD	$80°$	Cut the up going and horizontal events
angleTrackLength	$6°$	More than $6°$ track length in the camira
relativeEcalError	15%	Uncertainty on the reconstructed $E_{cal} \leq 15\%$
GHNdof	8	At least 8 points in the profile
xMaxInFOV	20g/cm^2	$X_{\max}$ in FoV at least with $20g/cm^2$
xMaxObsInExpectedFOV	$(60\text{g/cm}^2, 0°)$	$X_{\max}$ reconstructed in expected FoV
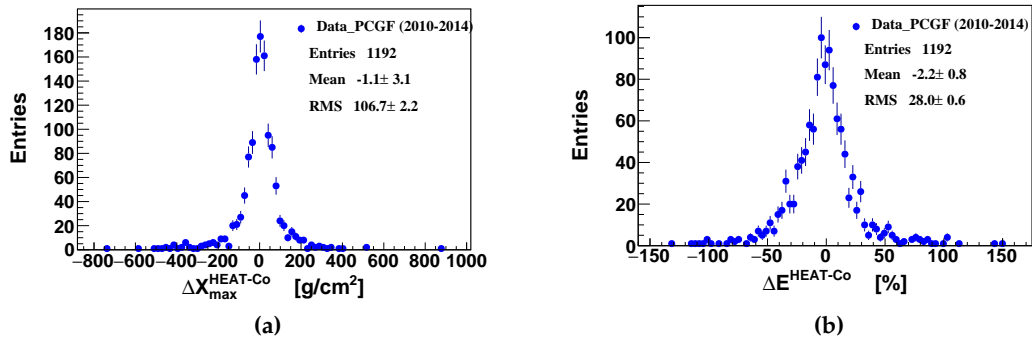
**Figure 4.10:** Comatibility of HEAT in downward and Coihueco data with PCGF reconstruction for (a) difference in X_{max} and (b) energy difference.
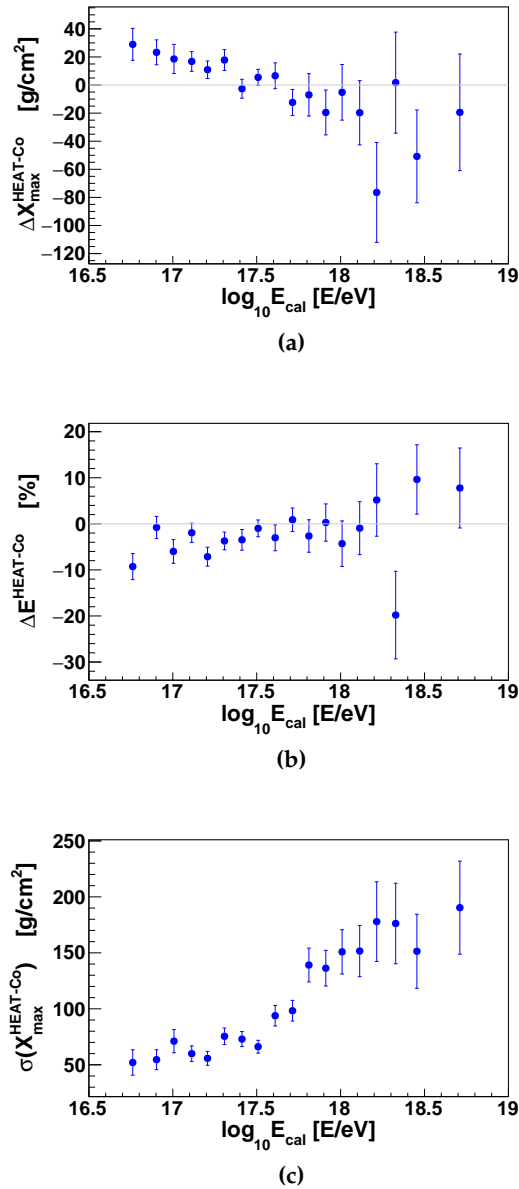

Figure 4.11: The stability of (a) ΔX_{max}, (b) Δ energy, and (c) X_{max} resolution as a function of the energy with PCGF reconstruction.

CHAPTER 5

Testing the performance of analytical Cherenkov light model in $\overline{\text{Off}}\underline{\text{line}}$

By default, air shower Cherenkov light is simulated in $\overline{\text{Off}}\underline{\text{line}}$ with an analytical model. This is very fast, and absolutely sufficient for high energy showers dominated by Fluorescence light. To test this model and to validate it also for shower dominated by Cherenkov light, I have tested the simulations with detailed Cherenkov photon emission directly generated in CORSIKA. This study aims to investigate how accurate the analytical Cherenkov light model [108] simulates and reconstructs the Cherenkov light in $\overline{\text{Off}}\underline{\text{line}}$. This is done using two Monte Carlo sets: CORSIKA set and CONEX set. The first set has showers with Cherenkov light simulated in CORSIKA and the CONEX set has showers with Cherenkov light simulated by the analytical Cherenkov model. By comparing the dependence of the interesting parameters, X_{max}, on the Cherenkov light in both Monte Carlo sets this giving the chance to indicate the accuracy of the analytical Cherenkov model and the impact on the measured parameter.

5.1 Simulations of Cherenkov showers with CORSIKA

In this section the different simulation parameters used to produced CORSIKA [43] and CONEX simulations are described. Together with the reconstruction technique used to reconstruct the low energy showers produced in both libraries.

5.1.1 CORSIKA configuration

Here is a brief description of the options used to run CORSIKA simulations to producing the "HEAT Full Cherenkov CORSIKA Library" for CORSIKA version 7.5602. A detailed description for each mentioned option can be found in [109]. CORSIKA supports many codes to simulate hadronic interactions. For the low energy hadronic interactions, the default one GHEISHA [110] is used and SIBYLL-2.3C [59, 60] is selected as the high energy hadronic interaction model. In order to simulate Cherenkov light, the CERENKOV option is used along with the CERWLEN option, which takes into account the dependence of the refractive index (n) on wavelength of the photons during the simulation process. Activating the SLANT option will calculate the longitudinal profile (dN/dX) as a function of slant depth instead of the vertical depth (as $X_{ver} \approx X \cos\theta$). In fact this option could be neglected in

case if zenith angle $\theta < 60°$, but for more accuracy, it is used. For performance reasons, the option THIN must be used to reduce the computing time for the full Cherenkov simulations. All these options are set during the program installation. To start simulating events with CORSIKA two main files are needed. The CORSIKA executable file in which all the input options are defined and CORSIKA input file named " steering card" in which the parameters of these options are controlled and coupled with many other parameters like shower geometry, energy and detection altitude. In Appendix B an example for one CORSIKA steering card can be seen.

The thinning option is a matter of reducing computing time for full Monte Carlo simulations. When the energy sum of all secondary particles in one generation falls below the thinning energy only one particle is considered as a representative of the other particles with a certain weight. Selecting large thinning levels ($\epsilon_{th} = E/E_o$), where E_o is the energy of the primary particle, will save much more of CPU time but at the same time will cause extra statistical fluctuations [111]. In this study we used $\epsilon_{th} = 10^{-6}$ with weight limit equal to 20. In order to speed up the simulation process as well as saving more disk space, a kinetic energy cut-off was applied for electrons and photons. For both electrons and photons 20MeV is the cut-off value, which is compatible with the Cherenkov threshold energy ($E_{th} = m_o c^2 (\frac{1}{\sqrt{1-n^{-2}}} - 1)$) for electron travel in air ($n \approx 1.0003$) of $E_{th} = 20.4$ MeV. On the other hand, the parameterizations used to produce the light in the analytical model uses only 1 MeV energy cut-off for the electrons. There is a big transition between 1 MeV and 20 MeV used in CORSIKA, however, the cut-off used in this study is a reasonable value as the particles with energies below 20 MeV do not produce Cherenkov light. The CURVED atmosphere option was not used as the simulated showers are inclined by $\theta \leq 60°$. Above this value the differences between a flat and a curved atmosphere become more and more important [109]. CORSIKA has a defined Cartesian coordinate system with positive x-axis points to the magnetic north, on the other hand it points to geographical east in Auger. With this in mind, a correction rotation angle (ARRANG = $-85.767°$) between the detector x-direction and magnetic north direction must be used. Other important parameter is the Earth's magnetic filed, which bent the charged particle paths. The magnetic field components at the Malargüe site ($B_x = 19.52\mu$T & $B_z = -14.17\mu$T) was used instead of the default location in Karlsruhe. The Cherenkov photons will be simulated with CORSIKA according to Auger telescope positions. The telescope positions are relative to the hight of the used observation level 1300m. In Table 5.1 the relative positions for HEAT and Coihueco telescopes at the hight of the observation level. All the geometry of this process in CORSIKA and in $\overline{Off\underline{line}}$ are in the reference-coordinate-system "ePampaAmarilla", which is at altitude of 1400 m above the sea level. Furthermore, only photons hitting an active sphere of radius 2.0 m around the HEAT telescopes, are saved. This spherical cut saves enormous amount of disk space and also CPU time. All these details are visualized in Fig. 5.1.

Table 5.1: The position of HEAT and Coihueco telescopes at the height of CORSIKA observation level 1300 m above the sea level.

| Telescope	position		
	x [cm]	y [cm]	z [cm]
HEAT	-3174112.43	1509557.42	161054.79
Coihueco	-3189575.93	1502612.80	161490.21
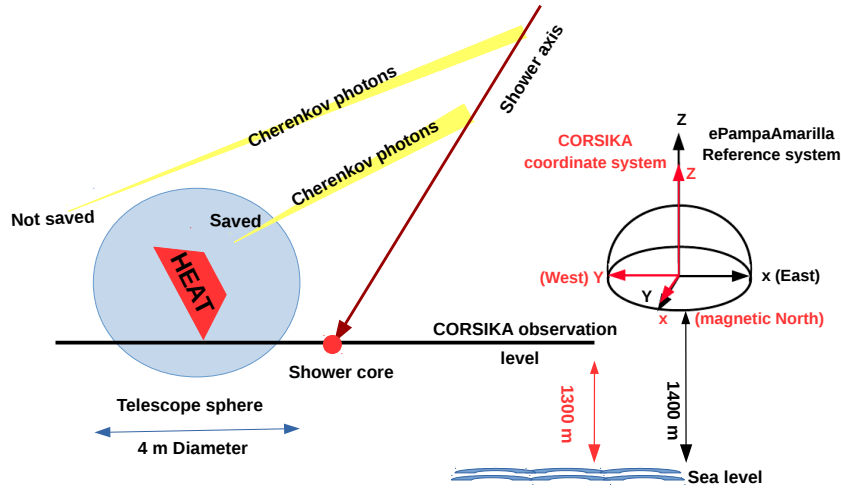
Figure 5.1: Layout describes the HEAT position at the CORSIKA observation level 1300 m above the sea level and the shower as reproduced in CORSIKA as well as the coordinate system in Off‾line‾ "ePampaAmarilla" at altitude of 1400 m (black) and CORSIKA (red).

5.1.2 Shower geometry generation

There is a strong correlation between the number of Cherenkov photons detected and the geometry of the air shower. In other words, running CORSIKA with Cherenkov option for random geometry is an extremely inefficient process. The thought is to use certain geometries, which already have a high Cherenkov fraction. Such geometries information could be taken from any ADST library. Based on that, this study is conducted in four steps: first producing a CONEX [52] ADST library. Then using this pool of showers to select the geometries of showers with high Cherenkov fractions. Thirdly is to simulate those geometries with CORSIKA and ended with reproducing the showers in Auger telescopes and reconstruct them with Off‾line‾. Fig. 5.2 summarize these steps.

A dedicated library for CONEX has been produced with around 2×10^6 proton shower at energy rang 10^{15}eV $<$ E $< 10^{17}$eV with slope index $\alpha = -1$. The shower cores can be within a circle of radius varying from 0 km to 10 km around HEAT and inclined by zenith angle below $\theta 60°$. All the showers were simulated with SIBYLL-2.3C hadronic interaction model. "ADST2CORSIKA " and "preselect" programs have been added to `StandardApplications/CherenkovCORSIKASimulation/adst2corsika`. These two program loop over the resulting ADST library and select the triggerd showers in HEAT with Cherenkov fraction more than 50% to extract the shower information: energy, core positions, zenith, θ, and azimuth, ϕ, angles, and finally automatically produce a CORSIKA steering card for each selected shower. A few correction must be taken into account to have the correct shower geometry identical to the one in CONEX and ADST. The core positions are recalculated to be in the reference-coordinate-system and at the hight needed for CORSIKA observation level. Also the zenith and azimuth angles are calculated in the same reference coordinate system. The azimuth is corrected by $-85.767° + 180°$, where $-85.767°$ takes into account the difference between CORSIKA and Off‾line‾ coordinate system and $180°$ consider the fact that the pointing direction is different in ADST than in CORSIKA. In ADST the shower points to where it comes from, however in CORSIKA it points to where it is going to. All the units are converted to be adapted CORSIKA units. From the CONEX library, 20760 showers were selected to be re-simulated in CORSIKA. These showers are selected based on having more

than 50% of light as Cherenkov seen by HEAT without any quality selection and more than 1000 photons arriving at the telescope aperture.

Now everything is ready to run CORSIKA: the input files with expected good geometries thought to produce enough Cherenkov photons and a proper CORSIKA executable file. Each shower runs as a single job on the cluster. In light of tracking the Cherenkov photons to 1300 m altitude and after using all possible proper thinning level, a single shower run for about 1dayin average and occupied around 30MB of disk space depending on its primary energy. CORSIKA produces six output files listed in Table 5.2. Coming to the final step in the process, $\overline{\text{Off}\underline{\text{line}}}$ reads CORSIKA output files and simulates the telescope response to each air shower. After that, the showers are reconstructed with PCGF, see Appendix B.2 for more details. At the end of that step a set of 3D Cherenkov light showers saved to ADST files. There are further details need to convert Cherenkov photons from CORSIKA to $\overline{\text{Off}\underline{\text{line}}}$. Photons within CORSIKA frame travel with speed of light divided by the reflective index while in $\overline{\text{Off}\underline{\text{line}}}$ they travel with speed of light neglecting the reflective index. Furthermore, CORSIKA can run with CERWLEN option or without it, which in turn can lead to slight change in the average number of the produced Cherenkov photons [112]. $\overline{\text{Off}\underline{\text{line}}}$ has been updated to include the reflective index in the speed with which photons travel as well as checking for the wavelength of the individual photons from CORSIKA. In case of CORSIKA was simulated without the CERWLEN option, $\overline{\text{Off}\underline{\text{line}}}$ itself will take into account the refractive index as a function of the photon wavelength. The configuration used to run $\overline{\text{Off}\underline{\text{line}}}$ with the Cherenkov simulations from CORSIKA coupled with a full example were added to the $\overline{\text{Off}\underline{\text{line}}}$ trunk at "StandardApplications/CherenkovCORSIKASimulation/SimWithCORSIKA".
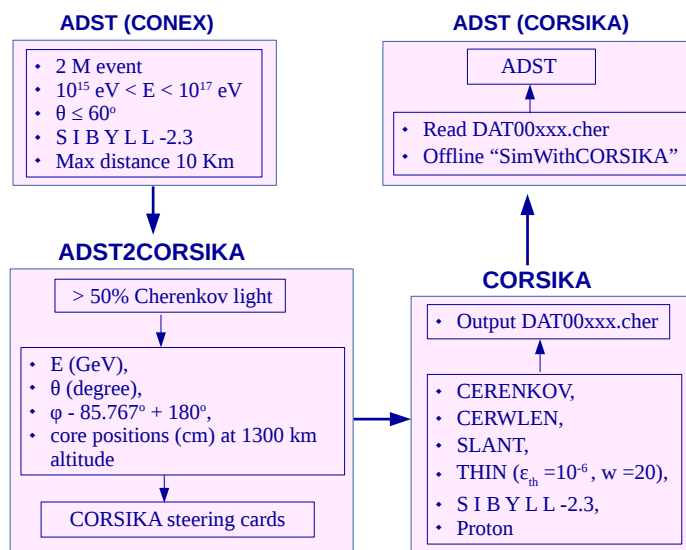
Figure 5.2: Summary of steps of producing the HEAT full Cherenkov CORSIKA library.

5.2 Results

In this work, about 20760 shower from the CONEX ADST library are selected to be simulated with CORSIKA and the same number of FD events are produced with $\overline{\text{Off}\underline{\text{line}}}$. Using the same reconstruction, PCGF, in the two Monte Carlo sets CONEX and CORSIKA, only 14173 event have a reconstructed PCGF profile for CONEX and 1413 event in case of CORSIKA. After applied significant cuts listed in Table 5.3 to keep reasonable statics for CORSIKA

Table 5.2: List of the CORSIKA output files for each single shower.

File name	Contains ..
DATxxxxxx	information about the particles reaching the observation level
DATxxxxxx.long	longitudinal development of the shower in the atmosphere
DATxxxxxx.cher	information on the Cherenkov photons
DATxxxxxx.cher-tel005	information on the Cherenkov photons at HEAT only
DATxxxxxx.lst	all the information of the shower simulation (a log file)
DATxxxxxx.inp	input parameters

showers, 6870 and 299 shower were selected in case of CONEX and CORSIKA respectively. For comparison between one of the selected shower from CONEX with its corresponding simulation in CORSIKA look to Fig. 5.3. This also shows how far the method used to extract the geometry from CONEX to CORSIKA is accurate. The number of reconstructed showers are less in CORSIKA then in CONEX and the reason behind that is the light produced for the same geometry in case of CONEX is attenuated in CORSIKA case. So for most of the CORSIKA showers the light was not enough to trigger the pixels. Fig. 5.4 shows a comparison between 299 shower selected from CORSIKA and the shower with the same geometry in CONEX. It is clear from Fig. 5.4a that the number of photons collected at the aperture are less for CORSIKA. Only for the showers with θ around $45°$ the light signal is Similar for CONEX and CORSIKA, one of those showers are in Fig. 5.3. Furthermore we check, the biases in the SDP[1] angles, shower axis parameters (χ_0, R_p, T_0) and the shower parameters $X_{\max}$ and energy. This is calculated and compared for each library. The bias is calculated for parameter A as the difference between the reconstructed ($A_{\rm rec}$) and the simulated ($A_{\rm gen}$) value. Also all energies used here are the calorimetric energies.

Table 5.3: Event selections used with both sets of CONEX and CORSIKA showers.

Cut	Cut value	Meaning
adst cuts version: 1.0		
eyeCut	10000	Select only HEAT events
minLgEnergyFD	1.e-20	Events with reconstructed energy
XmaxErrorLessThanXmax		Error in $X_{\max} < X_{\max}$ value
relativeEcalError	0.25	Error in the calorimetric energy $< 25\%$
xMaxError	100	Uncertainty in $X_{\max} < 100 \ {\rm g/cm}^2$
GHNdof	5	Reject events with low quality fit results
xMaxInFOV		$X_{\max}$ in FoV
!maxCFrac	70	Only showers with Cherenkove fraction $> 70\%$

5.2.1 Shower detector plane

The reconstructed biases in the two defined angles of the SDP Θ_{SDP} and Φ_{SDP} are shown in Fig. 5.5. Θ_{SDP} shows no bias and only angular resolution of $0.8°$ and $1.2°$ in CONEX and CORSIKA respectively. For Φ_{SDP}, also the bias has negligible size and the resolution is only $14.3°$ in CONEX and $20.7°$ in case of CORSIKA. Both CORSIKA and CONEX are consistent

---

[1]Shower detector plane
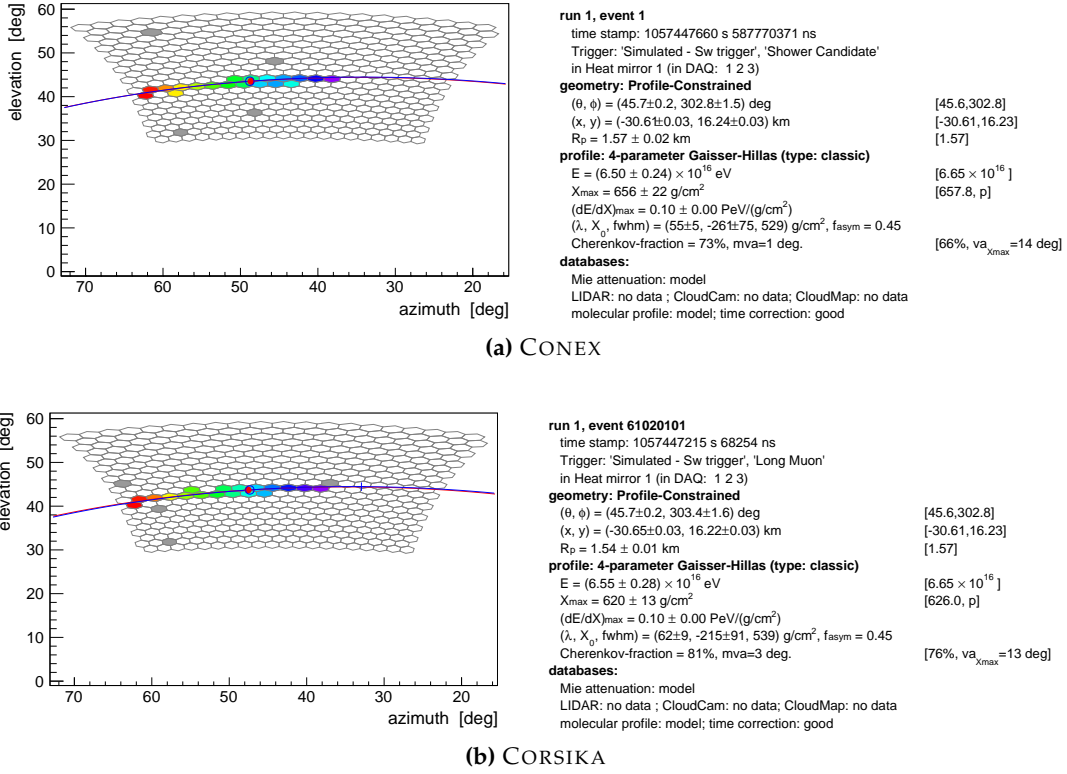
(a) CONEX

(b) CORSIKA

Figure 5.3: Camera view and information box for two showers with the same simulated geometry and energy 6.65×10^{16} eV (a) generated with CONEX and (b) generated with CORSIKA.

with each other very well which proofs that the high fraction of Cherenkov light and the analytical Cherenkov model do not cause a bias in the SDP angles.

5.2.2   Shower axis

The biases in the shower axis parameters χ_0, R_p, T_0 are shown in Fig. 5.6. The reconstructed bias in the shower axis for both Monte Carlo sets are compatible and the values are within the detector resolution. CORSIKA shows a bit higher statistical fluctuations. Also the biases in both χ_0 and T_0 are not dependent on the Cherenkov light in both Monte Carlo sets as it can be clearly seen from Fig. 5.7. On the other hand, R_p shows slight bias $\approx -11 \pm 4$ m in case of CORSIKA which is about 10 m more than in CONEX. The bias slightly depends on the energy of the shower as seen in Fig. 5.8. The bias in the R_p can be attributed to the different atmosphere modeling in CORSIKA than in $\overline{\textit{Off}}\underline{\textit{line}}$. In the end, 11 m bias in R_p, equivalent to only 38 ns, which can be neglected compared to the large time scale in which the shower takes place.

5.2.3   Shower parameters X_{max} and energy

In this section a special CORSIKA set is added, MC-axis, which is the same simulated CORSIKA showers but reconstructed with using the fixed simulated geometry, which mean no PCGF geometry is used here. The reason for that is to distinguish the effects from the geometry and profile reconstruction technique. The same selections in Table 5.3 is used for the CORSIKA MC-axis set. But for this section the selection was more than 70% Cherenkov light in the generated level not reconstructed level. The biases in X_{max} and energy were studied

(a)

(b)
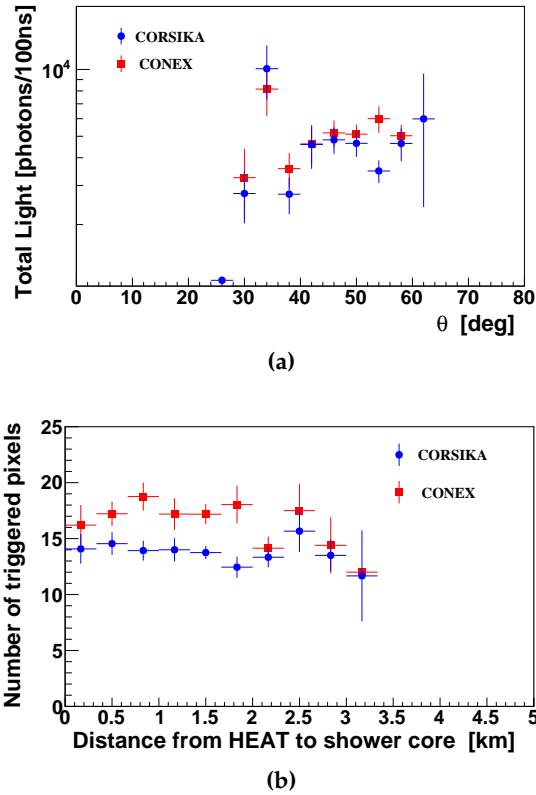
Figure 5.4: Shower to shower comparison for, the 299 shower selected in CORSIKA compared to the showers with the same geometry used to produced from CONEX. (a) The total light collected at aperture versus the zenith angle in degree for both CONEX (red) and CORSIKA (blue). (b) Number of triggered pixels versus the shower distance from HEAT telescopes for both CONEX (red) and CORSIKA (blue).

and how it is changing with the energy and the Cherenkov light fraction. The energy bias shows similar performance over the Cherenkov fraction and the energy in all Monte Carlo sets but with smaller bias in case of the CORSIKA MC-axis group. From Fig. 5.9 the average energy bias is $\approx 12\%$ for CONEX and CORSIKA and around 7% for the MC-axis, the two values are in the negative side and at average energy 2.5×10^{16} eV and 84% average Cherenkov fraction.

X_{max} in Fig. 5.10b has in general acceptable bias value for all sets less than $\approx 9\mathrm{g/cm}^2$ and similar behavior. On the other hand, in Fig. 5.10a CONEX shows notable bias with Cherenkov light but in average the bias value is $\approx 11\mathrm{g/cm}^2$ at 84% average Cherenkov fraction which is still acceptable. This bias in X_{max} as function of the generated Cherenkov light can be parametrized by, the red line in Fig. 5.10a,

$$\langle X_{\mathrm{bias}} \rangle = 3.8 + 3.1(C^{\mathrm{gen}} - 80) + 0.06(C^{\mathrm{gen}} - 80)^2, \tag{5.1}$$

where C^{gen} represent the generated Cherenkov fraction in percent. Furthermore, $\langle X_{\mathrm{max}} \rangle$ is investigated for dependence on the generated Cherenkov light in different energy bins, see Fig. 5.11. In all energy bins and at the three Monte Carlo sets, $\langle X_{\mathrm{max}} \rangle$ is independent of the generated Cherenkov light. For the lowest energy bin, $15.8 < \log_{10}\mathrm{E[E/eV]} < 16$, there was a drop in the statistics but the performance is still obvious good.

The validation of the analytical Cherenkov model uses within $\overline{\mathrm{Off}\underline{\mathrm{line}}}$ has been checked, by comparing two different Monte Carlo libraries one represent the analytical treatment of the Cherenkov light, CONEX, with second has more realistic Cherenkov light, CORSIKA.
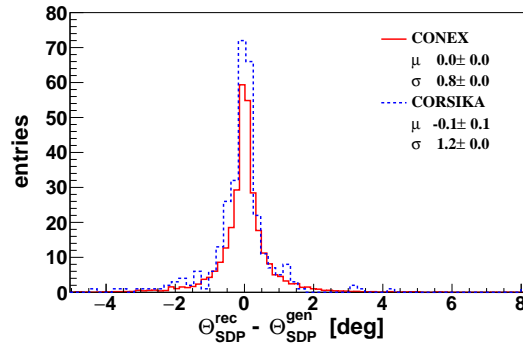
(a)
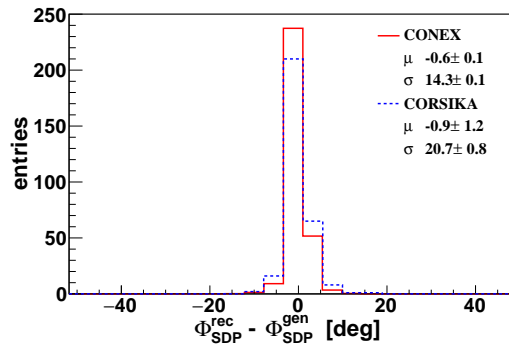
(b)

Figure 5.5: Bias in the shower axis parameters (a) Θ_{SDP} in degree, (b) Φ_{SDP} in degree, for both CONEX (red) and CORSIKA (blue dashed line). The SDP parameters are not biased by the high Cherenkov fraction. CONEX was rescaled to CORSIKA statistics.

The method introduced here to calculate the biases in the shower parameters and geometries in the two libraries shows a very good agreement in case of shower axis and energy. However, the analytical Cherenkov model shows an overestimating of the Cherenkov photons compared to CORSIKA. As well as X_{max} shows significant bias at Cherenkov fraction higher than 85% which would be considered as correction in any further calculations.
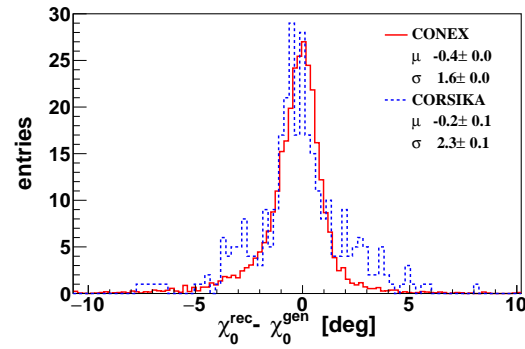
(a)
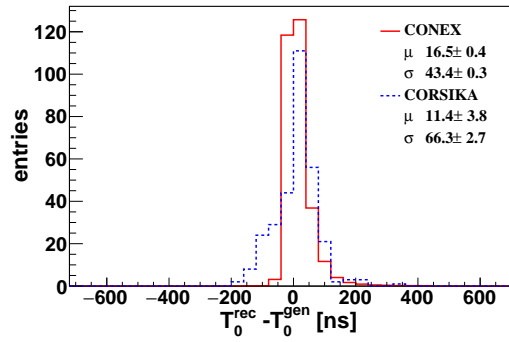
**(b)**
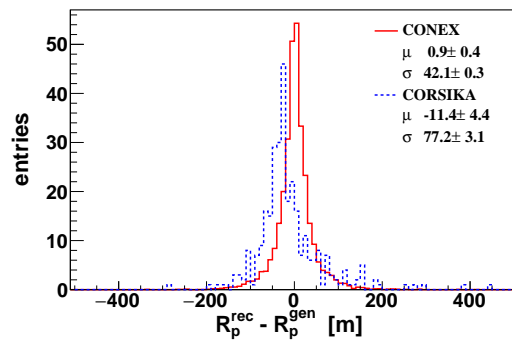
(c)

Figure 5.6: Bias in the shower axis parameters (a) χ_0 in degree, (b) T_0 in nanosecond and (c) R_p in meter for both CONEX (red) and CORSIKA (blue dashed line). CONEX was rescaled to CORSIKA statistics.
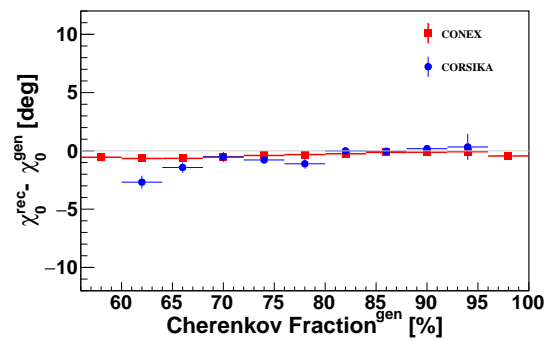
(a)
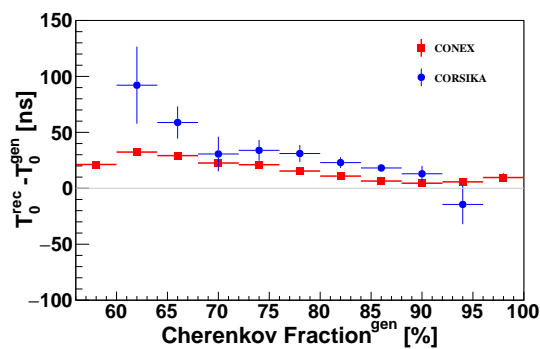
**(b)**

Figure 5.7: The bias in the shower axis parameters χ_0 and T_0 as a function of generated Cherenkov light for (a) χ_0 in degree, (b) T_0 in nanosecond for both CONEX (red) and CORSIKA (blue).
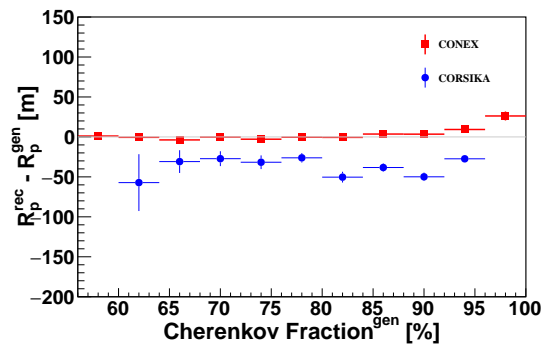
(a)
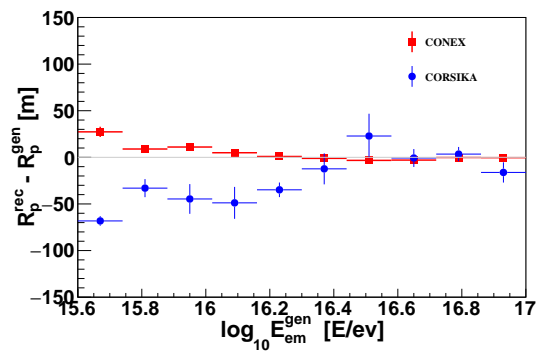
(b)

Figure 5.8: Changing in the R_p bias with (a) generated Cherenkov light and (b) generated electromagnetic energy for both CONEX (red) and CORSIKA (blue).
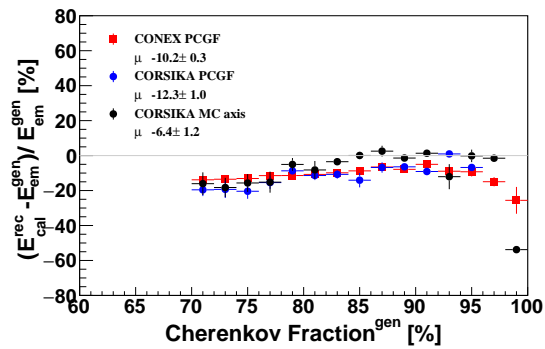
(a)
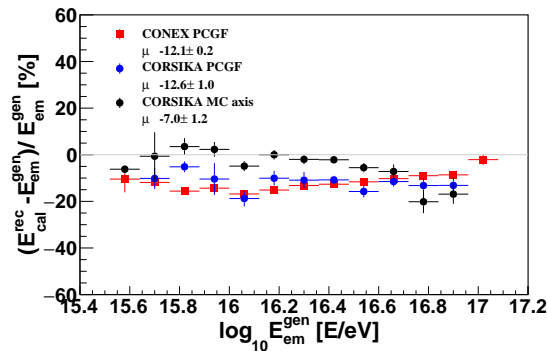
(b)

Figure 5.9: Energy bias in (%) plotted as a function of (a) simulated Cherenkov light and (b) simulated electromagnetic energy. For three different Monte Carlo sets for CONEX (red squares), and CORSIKA (blue circles) both reconstructed by PCGF, and finally CORSIKA using the exact MC-axis using the simulated geometry (black circles). The Cherenkov cut is applied on the generated measurements.

(a)

(b)
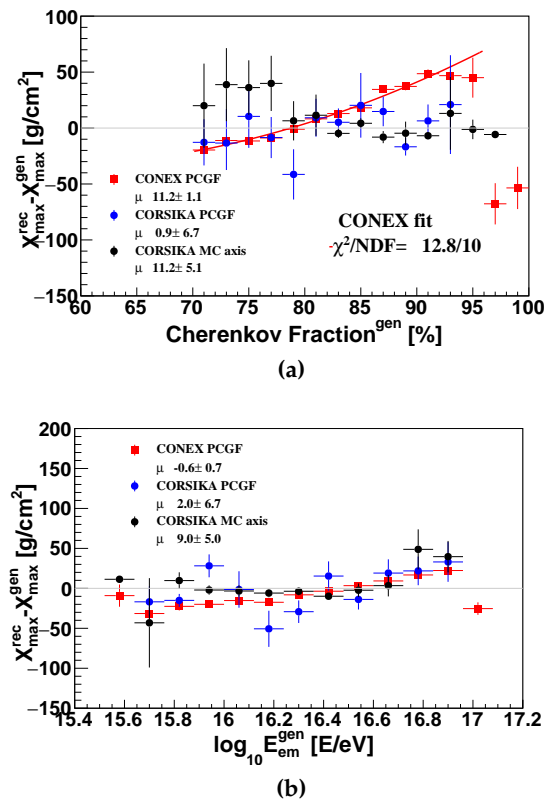
**Figure 5.10:** X_{max} bias plotted as a function of (a) simulated Cherenkov light and (b) simulated electromagnetic energy. For three different Monte Carlo sets: CONEX (red squares), CORSIKA (blue circles), both reconstructed by PCGF, and finally CORSIKA MC-axis using the simulated geometry (black circles). The Cherenkov cut is applied on the generated measurements.
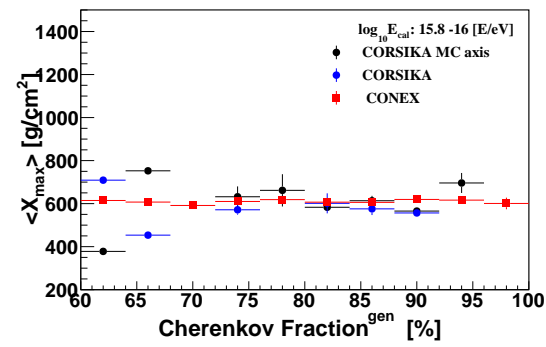
(a)
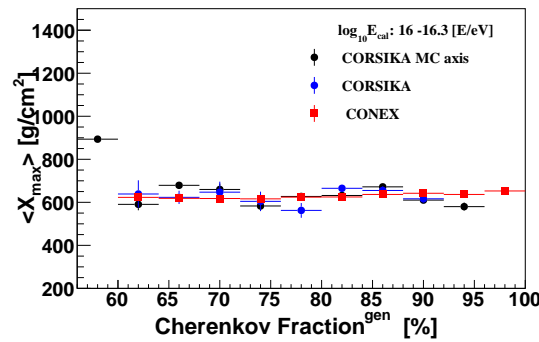
(b)
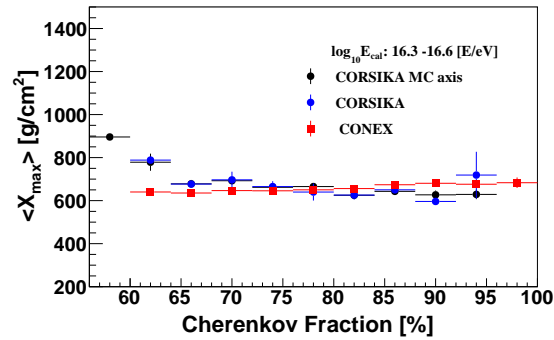
(c)

(d)
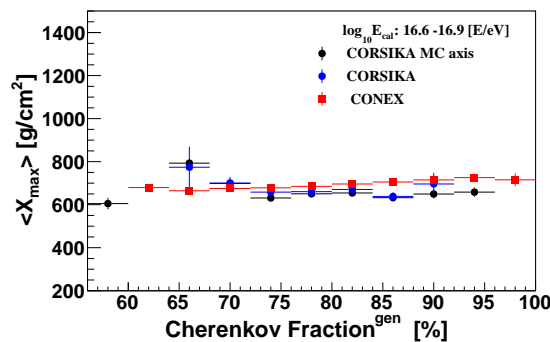
Figure 5.11: Mean X_{max} as function of Cherenkov light for different energy bins (a) $15.8 <$ $\log_{10}E[E/eV] < 16$, (b) $16 < \log_{10}E[E/eV] < 16.3$, (c) $16.3 < \log_{10}E[E/eV] < 16.6$ and (d) $16.6 < \log_{10}E[E/eV] < 16.9$. For three different sets: CONEX (red squares), CORSIKA (blue circles), and finally CORSIKA MC-axis (black circles).

CHAPTER 6

Event reconstruction and selection

For this thesis, the data collected with the HEAT telescopes of the Pierre Auger Observatory from 1st of January 2012 to 31st December 2015 are analyzed. The Profile Constrained Geometry Fit, PCGF, technique is used to reconstruct the HEAT data, which is described in Section 3.4. This technique makes it possible to reconstruct showers at energies much below 10^{17} eV with high statistics and good quality in comparison to the hybrid and HeCo reconstructions, as can be seen in Fig. 6.1. In order to study the mass composition of cosmic rays, only the highest quality showers are considered. Therefore, a series of selection criteria are applied to the dataset. Additionally, a special study was performed to analyze the effect of the limited field of view on detection a particular type of showers. Both fluorescence and Cherenkov showers are equally considered in the calculations. After this kind of study, the dataset will be free from the bias concerning the telescopes FoV limitations. All these selection cuts are described in details in this chapter.

6.1 Data production

This analysis is based on a special data production reconstructed in particular for low energies studies of Auger data. It is a special data production not only because it is the first dataset for Auger of Cherenkov dominated showers reconstructed at such lower energies, but also because it is a time-consuming process and required special procedures to be done. In contrast to the normal hybrid reconstruction, reconstruction the raw data files with PCGF is an expensive process. In order to reconstruct one shower, you need in average about 8 minutes, which is significantly more compared to the required time in the standard reconstruction of 1 minute per event. That means you need more than one week on a single CPU to reconstruct only one day of data. For that reason a new program has been introduced to split the raw data file of one day into smaller files and distribute the load to a computer cluster. The reconstruction configuration used together with the required splitting code are added to the $\overline{\text{Off}}\underline{\text{line}}$ trunk available to the Auger collaboration as well as the ADST library was added to the public Observer server.

6.2 Event Selection

This section describes the selection criteria applied to the dataset in order to have showers with authoritative quality. Based in these selections the X_{max} resolution is calculated from
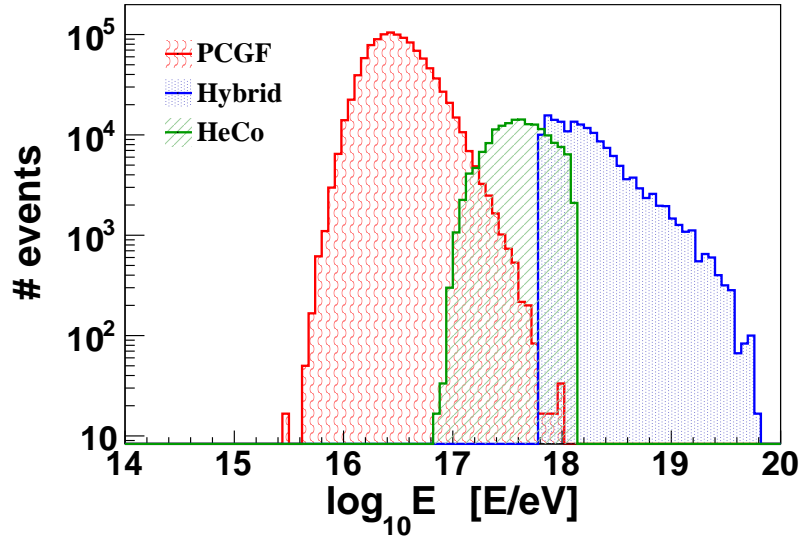
Figure 6.1: Distribution of the energy of the selected dataset reconstructed in light three different technique: PCGF, HeCo, and hybrid. Thanks to the PCGF the showers with energies lower than 10^{17} eV were reconstructed with high quality.

the RealMC to be about $40\mathrm{g}/\mathrm{cm}^2$ at energy of $10^{16.8}$ eV. In this analysis, the cuts are grouped into three groups one building on the other. The first group contains essentially selections, which are commonly used in most of the FD analyses. The most important cuts are within the second group, where the geometry and the profile quality selections are done. This group actually has a sensitive impact on the analysis results. In the end, the field of view cuts are applied directly after the second group quality selections. Table 6.1 summarized the number of event after applying each group of cuts. All the cuts and their efficiencies when applied on the dataset are grouped in Table 6.2. The technical cut list used within the $\overline{\mathrm{Off}\underline{\mathrm{line}}}$ framework is given in Appendix C.

Table 6.1: Number of the total reconstructed showers in the dataset and the number of the selected showers after each group of the applied cuts.

Selection steps	No. of events	Efficiency [%]
Total	981170	100%
Basics group	592120	60%
Quality group	84735	8%
FoV	49199	5%

6.2.1   The basics selections

This group of cuts checks for good atmospheric conditions as well as stable working condition of the detector plus general properties of the shower itself.

- Events recorded by HEAT only and when HEAT telescopes were orientated in the upward position are selected.

- Reject events obtained in the unstable working frame of the FD.

Table 6.2: Complete summary of all event selection study and their efficiencies when applied sequentially on the dataset.

	Cut	Cut value	Efficiency [%]
	eyeCut	10000	100
	heatOrientationUp	-	99.2
	badFDPeriodRejection	-	100
	skipSaturated	-	99.7
	noBadPixelsInPulse	-	100
Basics	hasMieDatabase	-	87.1
	LidarCloudRemoval	25 %	80.5
	MinCloudDepthDistance	(-50 ,50)	86.6
	MaxCloudThickness	100 g/cm^2	97.5
	maxVAOD	0.1 g/cm^2	96.4
	XmaxErrorLessThanXmax	-	75.2
	maxZenithFD	80°	100
	angleTrackLength	6°	70.8
Quality	Error in E_{cal}	15 %	53.8
	GHNdof	8	66.5
	min Cherenkov fraction	70 %	58.9
	xMaxInFOV	20 g/cm^2	97.2
FoV	expected FoV	($\zeta \leq 60$g/cm^2, mva $\geq 0^\circ$)	77.9
	fiducial FoV	-	74.6

- Reject events with saturated pixels, each PMT in the camera is characterized by a certain record range if the light signal is larger than this range the PMT is named saturated.

- No bad pixels in the pulse, this cut reject all the events with non-functioning pixels along the track.

- Select events which used the Measured Mie mode [1] during the reconstruction. This mean that the aerosol content had been measured in the atmosphere by the CLF[2]/XLF[3].

- Reject events with large cloud covers more than 25%, cloud thickness > 100 g/cm^2, and if there is no enough slant distance between the cloud and X_{max}.

- Events with low VAOD[4] [1] less than 0.1 g/cm^2 are selected. To avoid atmosphere contamination with aerosols.

- Select events which have energy. These events were fully reconstructed successfully.

- The X_{max} value must be bigger than the error in X_{max}.

---

[1]See Section Section 3.2.5

[2]Central laser facility

[3]Extreme laser facility

[4]Vertical aerosol optical depth
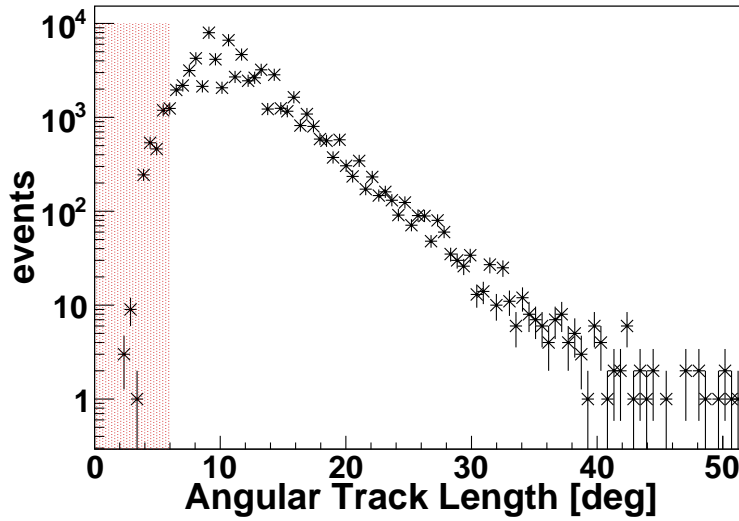
Figure 6.2: Distribution of the reconstructed angular track length for data. All events have track length $\geq 6^\circ$ are rejected.

6.2.2 The quality selections

This section focus on the quality of the showers. After applying the basics group of selection the dataset still contains a number of poor quality events. A combination of geometry and profile cuts can improve the quality of the dataset by avoiding the biased showers.

- Events tracks are chosen with length $\geq 6^\circ$. As came in [113] that the uncertainty of the reconstruction is more in case of the shower with small track length. And as shown in Fig. 6.9 for PCGF reconstruction 6° is reasonable cut value. The distribution of the angular track length is in Fig. 6.2.

- Only events which have uncertainty on the reconstructed calorimetric energy $\leq 15\%$ are consider in the dataset, otherwise the event is rejected. Fig. 6.3 shows the relative calorimetric energy error distribution.

- The fit of the shower profile are defined the quality of the Gaisser-Hillas fit. The best profile must have fit with at least 8 degree of freedom, dof, to be selected. See Fig. 6.4.

- The minimum Cherenkov light is 70%. This cut selects only the events which hitting directly the telescopes. See 6.5 for the event distribution of the direct Cherenkov fractions.

- Selected events must have their shower maximum within the FoV and at least $20\,\text{g}/\text{cm}^2$ distance from the borders of the FoV. This cut will reduce the systematic uncertainty as well as select high quality showers. The distribution of the $X_{\max}$ distance from the borders of the FoV are in Fig. 6.6.

Some of the used cuts are only secured selections to get rid of unwanted showers early and to make sure that no misshapen event will pass. This cuts such as:

- The estimated error in $X_{\max}$ are less than the $X_{\max}$ value.

- Remove the very inclined events with zenith angle $\leq 80^\circ$.
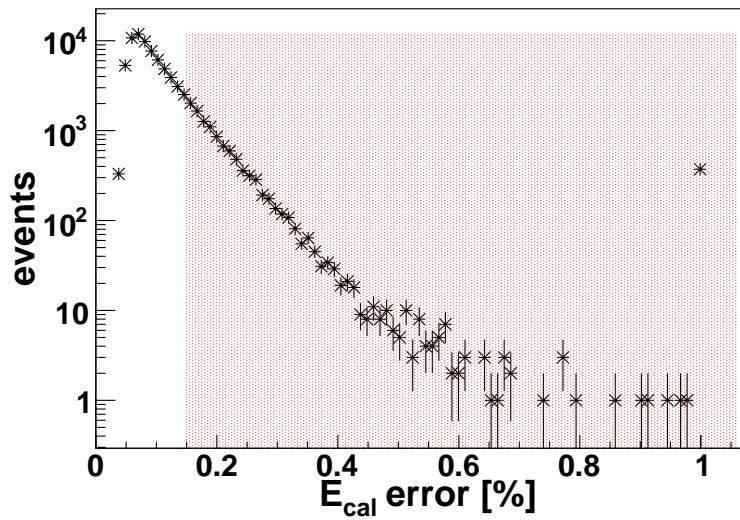
Figure 6.3: Distribution of the reconstructed E_{cal} error for data. All events in the red dots area are rejected ($\leq 15\%$).
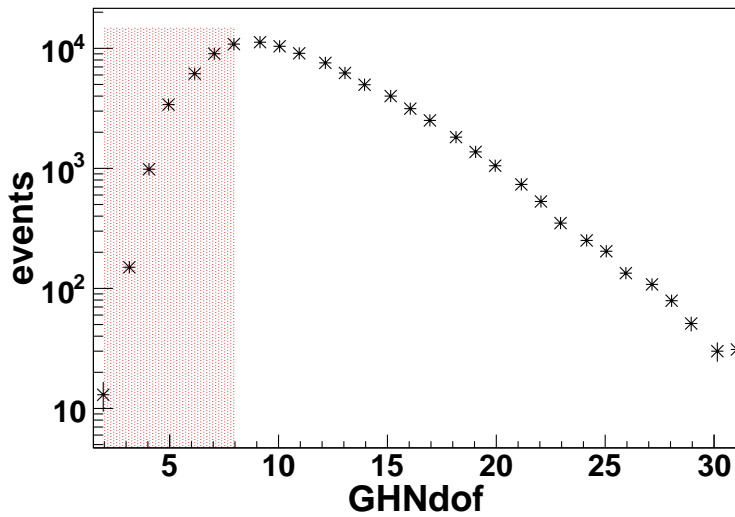

Figure 6.4: Distribution of the number of points in the profile fit. Profile with ≥ 8 points are passed the selection.

6.3 Field of view

The shower maximum can occur high or low in the atmosphere depending on the energy and inclination of the shower as well as the type of the primary particle. The field of view of the telescope does not go to infinity it is limited, so not all showers will have their X_{max} inside the FoV. Very shallow and very deep showers will have their X_{max} outside the FoV. These showers probably will not be reconstructed as the detected part of the profile can be very small. In case they pass the reconstruction, the uncertainty of the measured energy and X_{max} will be too large to trust these showers. For obtaining high quality results, X_{max} must be measured within the FoV. This restriction causes event selection bias. In this section, I will describe in details the method used to reduce this bias due to the limitation of the telescopes field of view. Starting from this point the field of view will be classified under three different
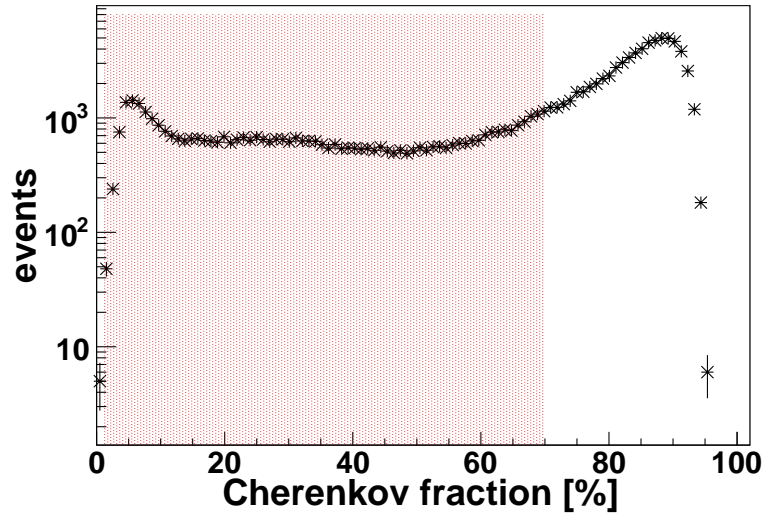
Figure 6.5: Distribution of the reconstructed Cherenkov light for data. All events in the red dots area are rejected ($\geq 70\%$).
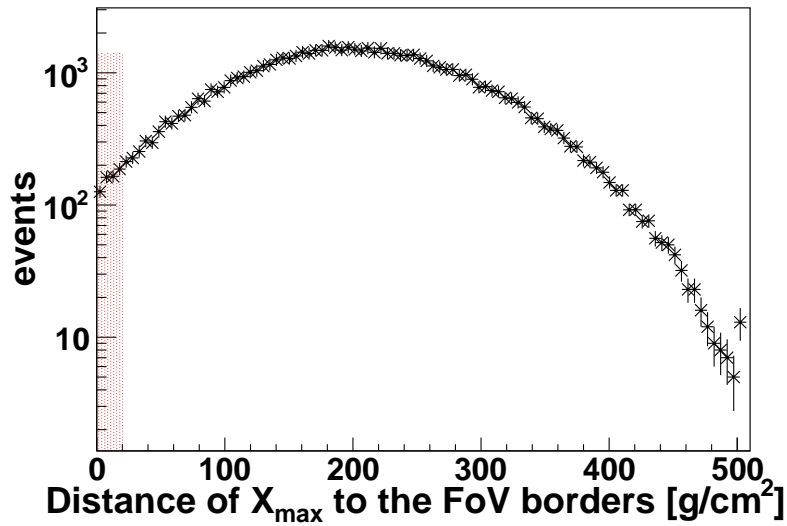

Figure 6.6: X_{max} distance to the borders of the field of view must be $\geq 20\mathrm{g/cm}^2$.

names: the geometry $\mathrm{FoV}^{\mathrm{geom}}$, the expected $\mathrm{FoV}^{\mathrm{exp}}$, and the fiducial $\mathrm{FoV}^{\mathrm{fidu}}$. The field of view selection can be summarized in two cuts: the first will guarantee high quality measured X_{max} this by selecting all events have X_{max} inside the $\mathrm{FoV}^{\mathrm{exp}}$. The second cut reject showers fall outside the $\mathrm{FoV}^{\mathrm{fidu}}$.

6.3.1 Geometrical field of view

Each telescope of the Pierre Auger Observatory has its own field of view depending on the direction and the angle of elevation of the telescope. HEAT telescopes differs from the standard telescopes as its elevation angle cover range of $30^{\circ} < \Omega < 60^{\circ}$. This means that HEAT observes more the showers developed high in the atmosphere and can see the edge of the atmosphere. At this point, I can imagine the geometrical FoV as an area of the atmosphere falls in front of the telescope and tilted with the same elevation angles of the

telescope. And $X_{\text{up}}^{\text{geom}}$ and $X_{\text{low}}^{\text{geom}}$ can be defined as the points in which the projected shower detector plane intersect with the camera borders [114]. The Shower track distance, h_v, which can be observed within the FoV$^{\text{geom}}$ changes as function of R, the distance from the shower core to the telescope, in the range $R\tan\Omega_1 < h_v < R\tan\Omega_2$. And $X_{\text{up}}^{\text{geom}}$ is the largest observed slant depth and $X_{\text{low}}^{\text{geom}}$ is the shortest observable slant depth. In Fig. 6.7a a layout simply describes the HEAT FoV$^{\text{geom}}$ and how observed track depth changes depending on how closer the showers are from the telescope.

6.3.2 Expected field of view

From the previous Section 6.3.1, we understand that a shower must have its X_{max} in the FoV$^{\text{geom}}$ in order to be reconstructed. However, this does not guarantee that every shower with X_{max} inside FoV$^{\text{geom}}$ will be reliably reconstructed. In case a shower with X_{max} in the FoV$^{\text{geom}}$ but it is far away from the telescope, the light that reach the telescope aperture will not be enough to reconstruct the shower with high quality. This explains an important fact that the FoV$^{\text{geom}}$ is not describing the active FoV in which a shower can be reconstructed. For that reason the expression FoV$^{\text{exp}}$ is introduced and can be defined as the region inside the FoV$^{\text{geom}}$ in which we are sure that all showers with X_{max} in this region are high quality showers. Fig. 6.7b simply illustrates the concept of the FoV$^{\text{exp}}$. Now the question how we can figure out this region for each shower. Actually, the maximum distance inside the FoV$^{\text{geom}}$ from which the telescope will be able to detect enough light to reconstruct a shower, depends on the energy, and the geometry of this shower as well as the atmospheric conditions. It is a fatigued and complicated process to include all these observables in one function and recalculate it for each shower. For that I will use the same approach used in the past in [114].

The idea behind this approach is to predict the maximum depth range $[X_{\text{low}}, X_{\text{up}}]$ in which the X_{max} is reconstructed with a certain resolution value or better. This is done by using virtual showers with the same reconstructed geometries and total energies as the measured showers but not the same X_{max} values. Where X_{max} is replaced by the Gaisser-Hillas maximum ,$X_{\text{max}}^{\text{GH}}$, for a given energy. The shower axis is divided into equal space depth bins inside the geometrical FoV $[X_{\text{low}}^{\text{geom}}, X_{\text{up}}^{\text{geom}}]$ and $X_{\text{max}}^{\text{GH}}$ is then moved at each depth length X_{i} along the shower axis to cover very large range in slant depth. At each position i, a predicted signal and the number of triggered pixels are estimated with a dedicated approximation using the light yield and the light transmission through the atmosphere. Then the uncertainty in the profile is estimated as well as the uncertainty in the reconstructed geometry. Using both uncertainties in the estimated profile and the reconstructed geometry the expected uncertainty in X_{max}, named $\zeta(X_{\text{i}})$, at depth X_{i} is calculated as the standard error propagation from the profile plus the geometry uncertainties. These steps are repeated for each depth X_{i} along the shower axis to get the expected uncertainty in X_{max} at different depths, which is shown in Fig. 6.8. Now it is clear at which depth X_{max} can be reconstructed with a certain uncertainty for a given energy and geometry.

In the past this approach worked successfully but only for the hybrid reconstruction where the Cherenkov light contribution was entirely neglected and only the fluorescence light was considered. In order to be able to use the same approach with the PCGF, I adapt this method to be a general method that also takes into account the Cherenkov light next to the fluorescence. Also PCGF event reconstruction is considered during the geometry uncertainty calculations. The uncertainty in the profile is mainly the uncertainty in the predicted signal. At this point, I managed to include the signal contribution from the Cherenkov light which was ignored in the previous studies. Now each depth X_{i} is expected to produce

$$n_i = n_i^F + n_i^{Ch},\tag{6.1}$$

where n_i is the number of photo-electrons expected to produce in the PMT[5]s of the camera, n_i^f and n_i^{ch} are the contributions from the fluorescence and Cherenkov light respectively which are given by

$$n_i^F = \frac{A}{4\pi r_i^2} c_{tel} \Delta X_i \omega_i \sum_f \epsilon(\lambda_f) T_i(\lambda_f) Y_i^F(\lambda_f) \tag{6.2}$$

$$n_i^{Ch} = \frac{A}{4\pi r_i^2} c_{tel} \Delta X_i \frac{\omega_i}{\alpha_i} \sum_c \epsilon(\lambda_c) T_i(\lambda_c) Y_i^{Ch}(\lambda_c), \tag{6.3}$$

where r is the distance to the telescope, A is the area of the telescope aperture, c_{tel} conversion factor from photons to photo-electron, ΔX_i bin length, and ω_i is the energy deposit per unit depth. For the wavelength dependence, the summation is performed over all fluorescence and Cherenkov wavelengths. The detector efficiency is represented by ϵ, T_i is transmission coefficients represent the Rayleigh and Mie attenuations, and Y_i^F and Y_i^{Ch} are the fluorescence and Cherenkov light yield respectively. And α_i is the average energy deposit per unit depth per electron. After adding also the background signal the variance in the energy deposit can be predicted and the uncertainty in the expected profile is known.

During the geometry uncertainty, there was an assumption that the uncertainty in the reconstructed geometry is constant along the shower axis. For that reason the uncertainty in the reconstructed geometry is rescaled with angular track length depending function. This function is parametrize the dependence of the space angle [6], $\Delta\Omega$, of simulated showers on the angular track length, α. I add a consideration for the type of the reconstruction used. So the geometry uncertainty will be rescaled by one of Eq. (6.4) equations depending on the reconstruction technique used to reconstruct the shower.

$$\Delta\Omega = \begin{cases} 0.18 + 0.21\left(\frac{30°}{\alpha}\right)^{2.1} & \text{for hybrid} \\ \\ 0.27 + 0.27\left(\frac{30°}{\alpha}\right)^{0.5} & \text{for PCGF} \end{cases} \tag{6.4}$$

In Fig. 6.9 the dependence of the space angle on the angular track length for both hyprid and PCGF reconstructions is shown. The performance of the updates I did to the calculation of the expected field of view can be seen in Fig. 6.10 where it shows comparison between the expected uncertainty $\zeta(X)$ at depth X_{max} and the calculated σX_{max} from the reconstructed profile, before and after adding the contributions from Cherenkov light and PCGF. First there was no correlation at all between $\zeta(X_{max})$ and σX_{max} (left panel) but after the updates the two quantities are in a good matching upto 100 g/cm^2 and above this value $\zeta(X_{max})$ is systematically lower (left panel).

Now and after the very good performance which can be seen in Fig. 6.10b, this approach can be used successfully with th PCGF reconstruction to select the high quality showers which will preserve a good X_{max} resolution. This selection is named "xMaxObsInExpected-FOV" and has two parameters first is the value of $\zeta(X_{max})$ you want to cut on and the second parameter is the value of minimum viewing angle[7], mva. In this analysis, 60g/cm^2 was chosen to be the cut value for the expected uncertainty of X_{max} and without restriction on the minimum viewing angle. This cut value will keep enough statistics as well as good X_{max} resolution. The acceptance of this selection as function of the distance from the telescope for energies between $10^{16.4}$ eV and $10^{16.6}$ eV can be seen in Fig. 6.11 and in Appendix E.1 all the energy bins are shown. From now on, the FoV will refer to the FoV^{exp}.

---

[5]Photo-multiplier tube

[6]The space angle defined the width angle between the simulated and the reconstructed shower axis.

[7]The angle between the pixels field of view direction and the shower axis.

(a)

(b)
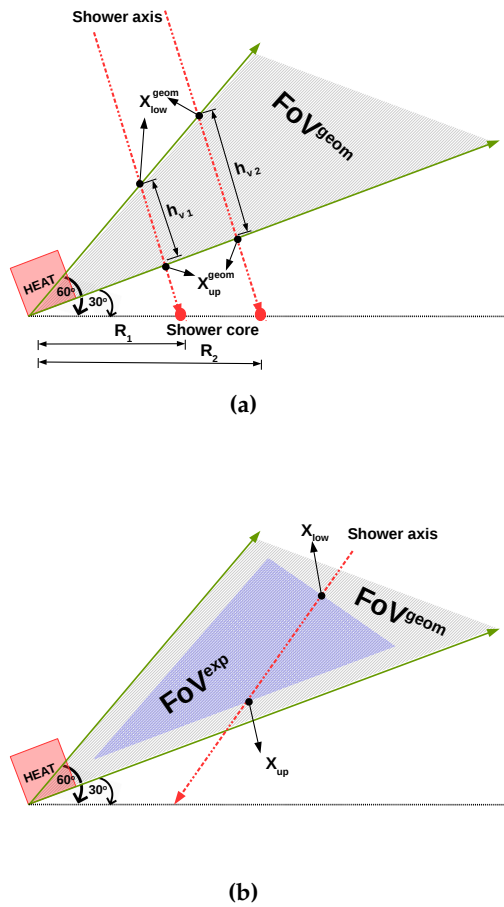
Figure 6.7: Simplified diagrams show the difference between the FoV$^{\text{geom}}$ and the FoV$^{\text{exp}}$ where (a) shows the HEAT geometric FoV as the shaded area with black lines and defined by the $30°$ and $60°$ elevation limits. The observable height (h_v) of the shower track changes as a function of the distance between the shower core and the telescope (R). The closer the shower from the telescope is the shorter the observable track. And (b) shows the expected FoV (blue dashed area) which represents the part of the FoV$^{\text{geom}}$ in which the showers have a certain X_{max} uncertainty. X_{up} and X_{low} characterize the new depth in the FoV$^{\text{exp}}$.

6.3.3 Fiducial field of view

So far the effective field of view in which the showers can be observed and reconstructed with high quality is known under the name of FoV$^{\text{exp}}$ but there is still a bias due to the limitation of this FoV. The heavy primaries showers develop high in the atmosphere, represented by the red shallow shower A in Fig. 6.12 and the light primaries showers penetrate the atmosphere more deeply than the heavy primaries. Shower type B in Fig. 6.12 represents the light-induced showers. Suppose that there is a group of showers with nearby energies and geometries but produced from different primaries. The FoV will not equally observe these showers, however, they have the same energy and geometry. This means that the FoV would prefer one type of the primaries over the other, which leads to distortion in the X_{max} distribution. The X_{max} distribution can truncated from the left side for large values of X_{low} as the shallower showers will be filtered and X_{up} small values will filter the deep showers and truncate the X_{max} distribution from the right side.

The FoV study is critical for the mass composition study. The aim is getting rid of this distortion in the X_{max} distribution so that the mass composition results are as close as
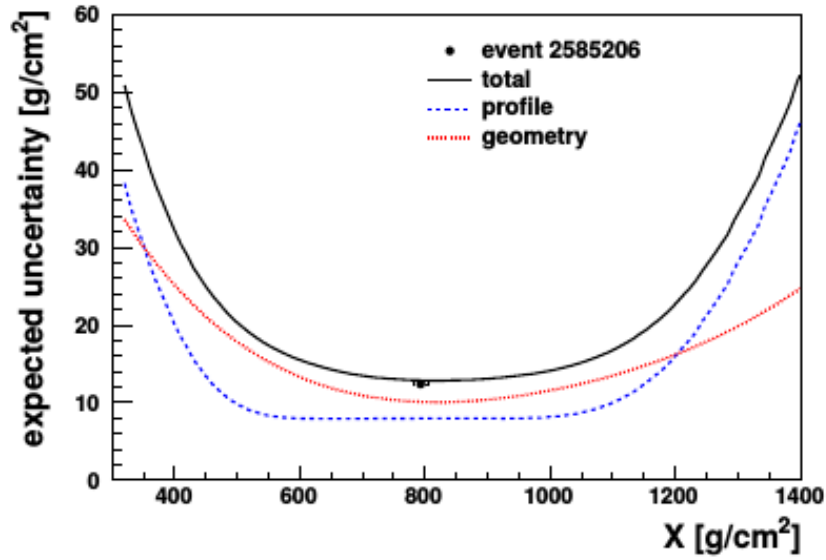
Figure 6.8: The expected uncertainty in X_{max} for one shower at different depth along the shower axis inside the FoV^{geom}. The black curve is the standard error propagation from both uncertainties in the estimated profile (blue curve) and the reconstructed geometry (red curve). The black dot is the reconstructed X_{max} value. As long as X_{max} is reconstructed away from the FoV^{geom} boundaries its uncertainty decrease. Figure from [114].
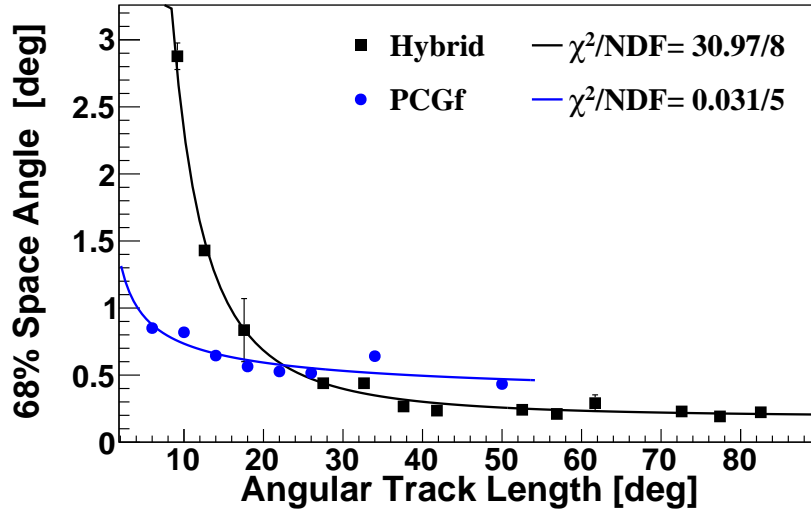

Figure 6.9: The space angle between the generated and the reconstructed shower axis that contains 68% of the reconstructed events as a function of the angular track length for hybrid (black) and PCGF (blue) reconstructions. The hybrid data points (black squares) was taken from [115].

possible to the reality. This is achieved by defining the largest range of the FoV in which the showers are observed with 100% efficiency regardless of their primary particles, and this is what is named the fiducial filed of view, FoV^{fidu}. All showers falling outside this range are not selected.

Giving an illustration of how the FoV^{fidu} is defined, first we assume that the exponential modified Gaussian distribution, EMG, can perfectly describe the X_{max} distribution, see Eq. (D.5) for the mathematical expression. Then the changes in the mean of this distribution as a function of the FoV boundaries, X_{low} and X_{up}, are studied. For the best result, the data

(a)

(b)
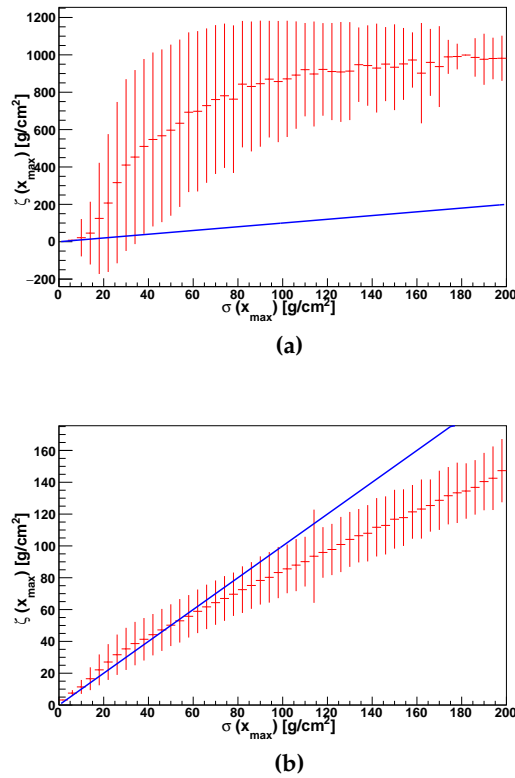
Figure 6.10: Performance of $\zeta(X_{max})$ before (a) and after (b) improving the calculations for the PCGF reconstruction. Error bars represent the RMS spread around the mean value. Blue lines are expectation in case of perfect correlation.
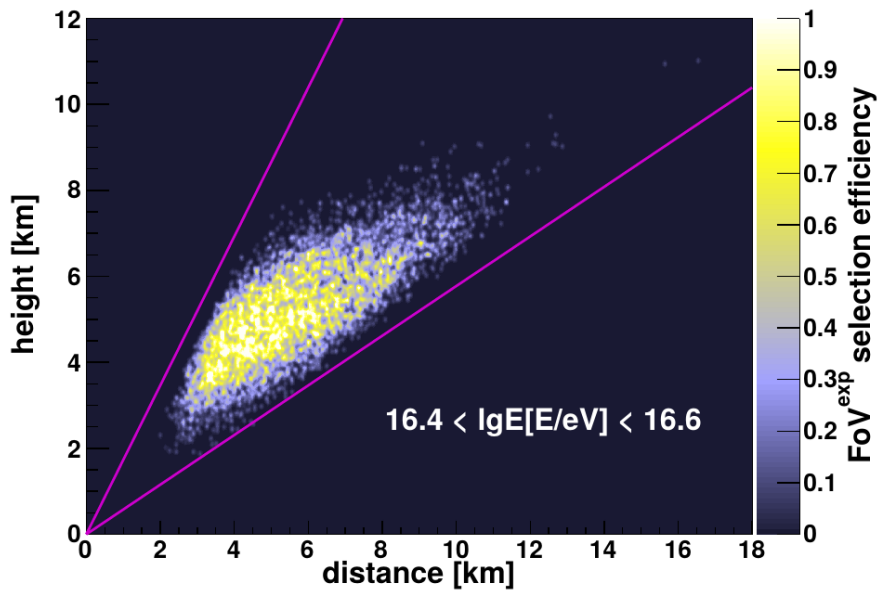

Figure 6.11: The expected field of view for data showers with energies between $10^{16.4}$ eV and $10^{16.6}$ eV. On the x-axis the ground distance from the shower X_{max} to the HEAT and on y-axis the height of X_{max} above the telescope. The magenta lines define the FoV^{geom} for HEAT. The color scale describes the efficiency of selected quality showers.

sample are divided into small energy bins each bin with width of 0.1 in $\log(E_{cal}/\text{eV})$ and for each energy bin the truncated mean of the X_{max} distribution is calculated. Fig. 6.13 shows one example of the truncated mean for bin $15.9 \leq \log_{10}(E_{cal}/\text{eV}) < 16$. The results for all energy bins can be seen in Appendix E. The mean of the shower maximum must be independent of the FoV boundaries. Eq. (6.5) represents the mean of X_{max} distribution in infinity FoV. In reality, X_{max} distribution can be unbiased only in a given range of the FoV $[x_1, x_2]$, where x_1 have values along the X_{low} ranges and x_2 changes along the X_{up}. So Eq. (6.5) will replaced by the truncated mean Eq. (6.6) and fitted simultaneously to the data points of Fig. 6.13. A detailed calculation for the truncated mean function is given in Appendix D.

$$\langle X_{max} \rangle^\infty = \frac{\int_0^\infty x G(x) \otimes E(x) dx}{\int_0^\infty G(x) \otimes E(x) dx} \tag{6.5}$$

$$\langle X_{max} \rangle^{trun} = \mu^{trun}(x_1, x_2) = \frac{\int_{x_1}^{x_2} x G(x) \otimes E(x) dx}{\int_{x_1}^{x_2} G(x) \otimes E(x) dx}. \tag{6.6}$$

The changes in the mean of X_{max} as a function of the upper and lower boundaries of the FoV are clearly seen in Fig. 6.13, where one can observe two main features. First, the plateau region in which $\langle X_{max} \rangle^{trun} \approx \langle X_{max} \rangle^\infty$ and the edges of the X_{max} distribution are far enough from the FoV limits. Second feature represents the deviation of the $\langle X_{max} \rangle^{trun}$ from the $\langle X_{max} \rangle^\infty$ where FoV boundaries start to cut on the X_{max} distribution. From that the fiducial field of view is selected to be the region which fulfill the condition

$$|\langle X_{max} \rangle^{trun} - \langle X_{max} \rangle^\infty| \leq \Delta, \tag{6.7}$$

where Δ is the systematic uncertainty that define the maximum acceptable deviation in $\langle X_{max} \rangle^{trun}$ from the plateau. Here $\Delta = 5\text{g}/\text{cm}^2$ was selected consistent with the study done in [114] for which the systematic uncertainty is small as well as saving the event statistics. Fig. 6.14 shows all the fiducial cuts for all the energy bins which parameterized as

$$\text{FoV}^{fidu}(\log_{10}E_{cal}) = \begin{cases} 405 + 103.5(\log_{10}E_{cal} - 16)^2 - 0.4(\log_{10}E_{cal} - E_o) & \text{the upper limit} \\ \\ 759.6 - 67.7(\log_{10}E_{cal} - 16)^2 - 0.9(\log_{10}E_{cal} - E_o) & \text{the lower limit.} \end{cases} \tag{6.8}$$

This FoV^{fidu} selection is applied depending on the calorimetric energy of the showers. This selection cut is a bit tricky as it changes depending on the other selections, so it rather important to apply all the quality selections first. Normally, the statistics heavily decrease after the FoV selection, but this was not in our case. The reason for that is most of the events remained after applying the selections in Table 6.2 are direct showers like shower C in Fig. 6.12. The effect of the FoV selection can be seen in Fig. 6.15, where there is a shift of $\approx 20\text{g}/\text{cm}^2$ in $\langle X_{max} \rangle$ as a function of calorimetric energy due to the FoV bias at the low energy bins.

At the end of the selection criteria, 49199 showers have been selected which represents around 8% of HEAT data taking in four years. This looks like a small fraction of events but actually it is a very good statistic at such low energies range accompanied by high quality. Those showers are used in this thesis to study the cosmic rays mass composition in the energy range $15.8 \leq \log_{10}E_{cal}/\text{eV} \leq 16.9$. In Fig. 6.16 a scattered plot shows the X_{max} values of the selected showers with their energies. The distribution of X_{max} in each energy bin can be seen in Appendix F.
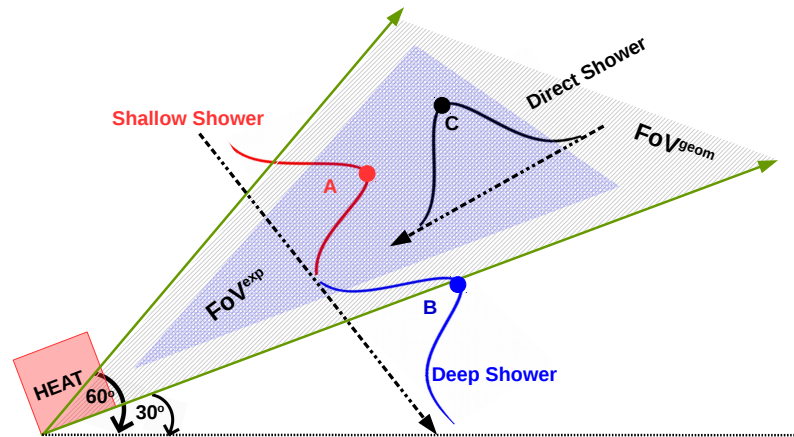
Figure 6.12: Sketch for three types of showers in the HEAT field of view indicating how the limited FoV can causes a bias in the X_{max} distribution by preferring observing one type over the other. Type A (red) represents a shallow shower can produce by heavy primary nuclei. Type B (blue) represents a deep shower can produce by light primary nuclei. Type C (black) is a direct shower which travels directly to the telescope most of the shower in that case fall in the FoV.
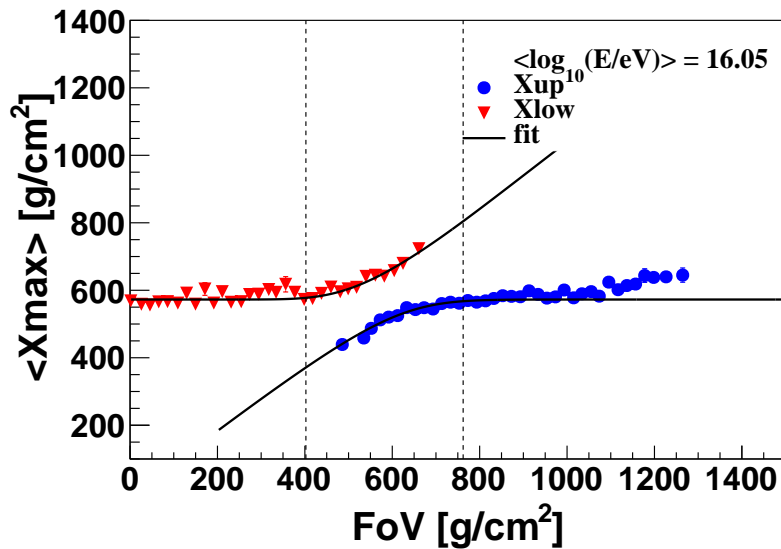

Figure 6.13: The dependence of $\langle X_{max} \rangle$ on the FoV boundaries for the energies range $15.9 \leq \log_{10} E_{cal}/eV < 16$. The red inverse triangles represents the change in $\langle X_{max} \rangle$ with X_{low} the upper limit of FoV and the blue dots represents change with X_{up} the lower limit of FoV. Both profiles are fitted with the μ^{trun} function shown in Eq. (6.6). The dashed lines represent the limit values of the FoV^{fidu}, where the truncated mean starts to deviate by more $\Delta = 5 g/cm^2$ from the plateau, $\langle X_{max} \rangle^{\infty}$.
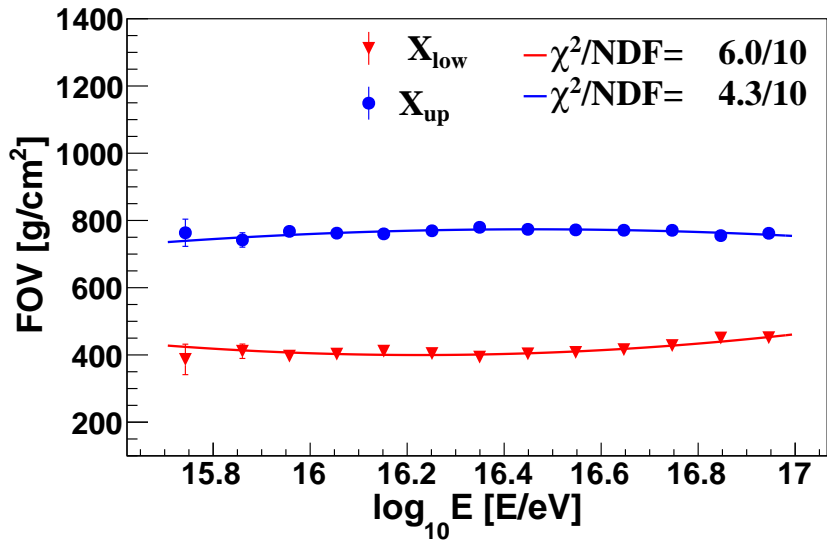
Figure 6.14: The fiducial FoV boundaries for our data sample. Each bin represent the change in the lower (red inverse triangles) and the upper (blue dots) FoV boundaries as a function of the logarithmic calorimetric energy of the shower. The red and the blue lines are the fit as parameterized with Eq. (6.8).
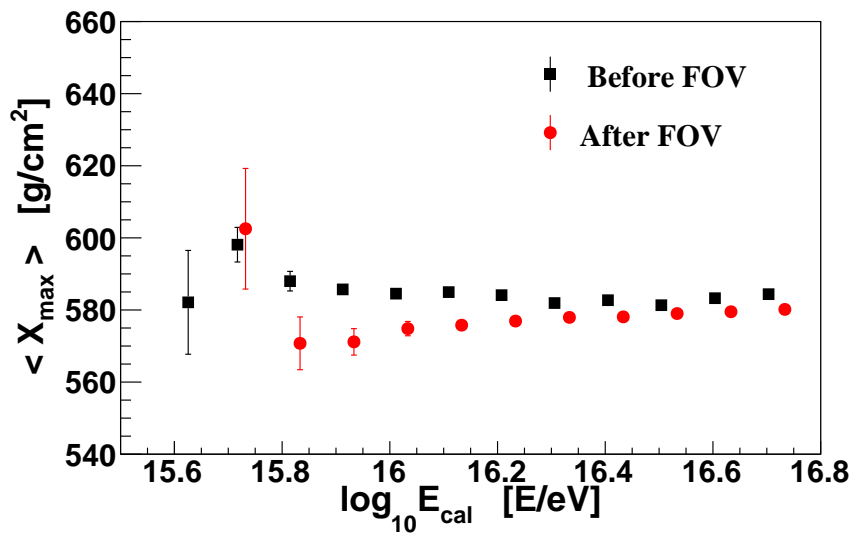

Figure 6.15: $\langle X_{max} \rangle$ before (black squares) and after (red dots) applying the FoV selections.
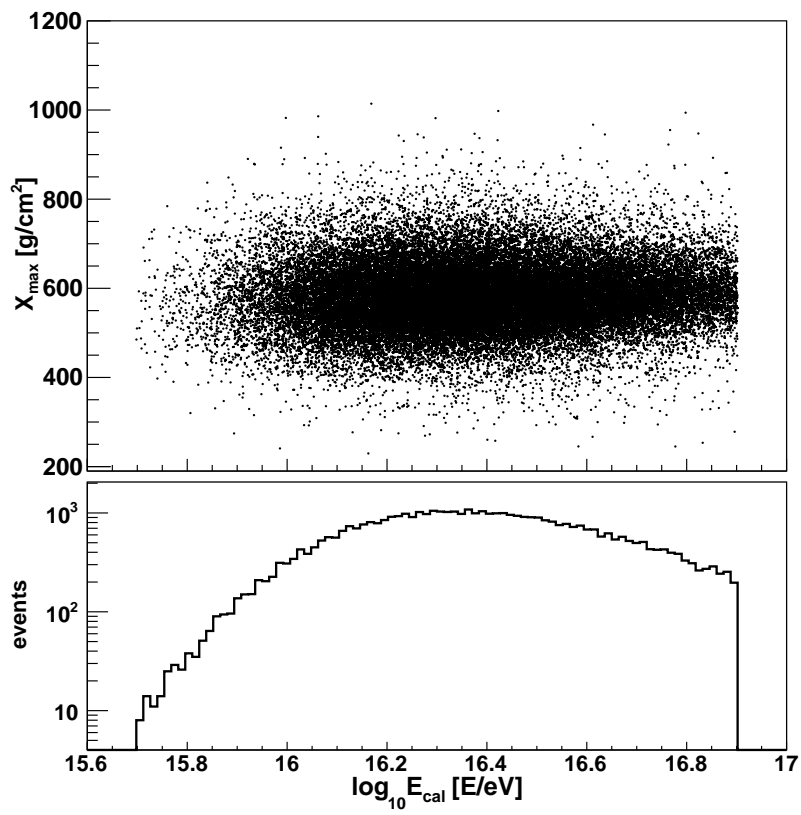
Figure 6.16: Remaining events after applying all the selection criteria. In the upper panel, the X_{max} and the energy and in the lower panel, the number of events in each energy bin.

CHAPTER 7

The analysis performance with RealMC simulation

This chapter will discuss the shower and the detector simulation library that was specifically produced for HEAT at low energies. This Monte Carlo library is used to study the performance and efficiency of the reconstruction technique used to reconstruct the data showers. From this study, the reconstruction biases and the detector resolution are calculated and used as corrections for these effects in the data sample. In order to have an accurate correction of the data, the detector must be simulated in realistic conditions. For that reason a time-dependent simulation is used, in which not only the showers and the detector are simulated but also the information for the atmospheric conditions and the detector calibration in a given time period are taken into account. This type of simulations is known as the "dynamic simulation" or the more common name "RealMC".

7.1   RealMC library

This RealMC was produced especially for studying the Cherenkov showers, which are reconstructed by PCGF. This simulation was done together with Vladimír Novotný to use for the Pierre Auger collaboration. The simulation process has mainly three parts, first, is the shower simulation, then the simulation of the detector response and at the end the reconstruction of the shower. The software framework of Auger, $\overline{\text{Off}}\underline{\text{line}}$ [101, 102], the same version used in the data reconstruction is used to simulate the detector response and for the showers reconstructions. CONEX [52] version 2r5.64.r6499 is used for generating the showers with SIBYLL-2.3C [59, 60] as a hadronic interaction model. This kind of simulations can be done in one single run by using the CONEX shower generator available within the $\overline{\text{Off}}\underline{\text{line}}$ framework, or in two runs. For the latter, the showers are first generated with CONEX, then $\overline{\text{Off}}\underline{\text{line}}$ reads the pre-generated CONEX files and simulates the detector response, and reconstruct the showers in the second run. Whatever method is selected for the simulation, the result will be identical. This simulation was done in one run. What really will affect the simulation is the controlling parameters, which are needed for each step of the simulating sequence. So carefully chosen parameters will save CPU time and will produce a good representative simulated showers for the data sample. This simulation is performed for a mixed composition of proton and iron primaries of 50% in the energy range 10^{15} eV to 10^{17} eV with spectral index -2. The simulated energy range is wider than the data range to

avoid the migration of the events at the border. All the showers were simulated in a circle of radius 7000 m around HEAT telescopes with inclination angles, θ, in the range $0°$ to $90°$.

As required for a time-dependent simulation, the same time range as when the data was recorded, 2012 till 2015, is chosen for simulating the HEAT telescopes. In order to simulate this long time period with enough statistics, each shower was recycled 100 times in the detector simulation by using different random positions. The simulation sequences have been done in the standard way [116, 117] the only difference is that the SD simulations are skipped. The PCGF reconstruction needs only the mono FD events. However, without further improvements, the RealMC for Cherenkov events is technically not really feasible. This is since Cherenkov showers prefer a very small part of the overall random phase space of possible geometries. Showers must be within a limited solid angle to the telescope viewing axis. Thus, I developed a geometry pre-selection to avoid simulating showers with no probability of being reconstructed by PCGF. An acceptance selection during the simulation is developed and added to the FD "simulation-checker" module. This acceptance cut is a parametrization of a function describing the dependence of the trigger efficiency on the X_{max} viewing angle[1] in logarithmic energy and in the core distance from the HEAT. The benefit of this selection is to increase the probability of the simulated showers to trigger. This acceptance selection was done using the same CONEX library described in Section 5.1.2. Adding this acceptance cut for the simulation process make it more efficiency and reducing the computing time used in simulating events which can not triggered at the end.

The showers are reconstructed using the PCGF reconstruction as used in the data production. The selection criteria used here are the same as that used for the data in Section 6.2. But the fiducial FoV analysis is performed also specifically for the RealMC showers. All the plots from the FoV study of the RealMC showers in the calorimetric energy range $10^{15.8}$ eV to $10^{16.9}$ eV are collected in Appendix E. The simulation parameters are adjusted to get simulated showers describing the data as well as possible. However, there is still some discrepancy between the data and the Monte Carlo. To reduce this discrepancy further the Monte Carlo library is re-weighted event-by-event to the data sample. An energy weighting factor is used so the Monte Carlo simulations follow the energy flux of the reconstructed data. This factor is calculated in two steps: first, divide the normalized $\log_{10}E_{cal}$ distribution of data by the Monte Carlo. Then, fit this ratio and the parametrization of the fit is representing the weight factor. The normalized data and Monte Carlo distributions are shown in the upper panel of Fig. 7.1, and in the lower panel is the ratio of both distributions together with the fit. The agreement between RealMC and data is checked using two geometry parameters, zenith angle and R_p. This investigation of the shower geometry from data and Monte Carlo showed a good agreement, which promote that the detector is well described by the simulation. In Fig. 7.2 is an example for the lowest energy bin $10^{15.7} - 10^{15.8}$ eV and in Fig. 7.3 another example at the largest energy bin $10^{16.8} - 10^{16.9}$ eV in the investigated energy range. Both data and Monte Carlo show a good a agreement for both R_p and zenith angle in the two examples of energy bins shown here. All the energy bins are shown in Appendix G.

7.2   Biases and resolution of Cherenkov dominated showers

As long as the same reconstruction and selection criteria are used for both Monte Carlo and data sets and after having the same energy flux in both by weighting, using the Monte Carlo library we can measure the detector resolution and the biases caused by the reconstruction in the energy and the X_{max}. Before going further in the biases and resolution calculations, X_{max}

---

[1]X_{max} viewing angle is the angle between the pixels field of view direction at X_{max} point and the shower axis.
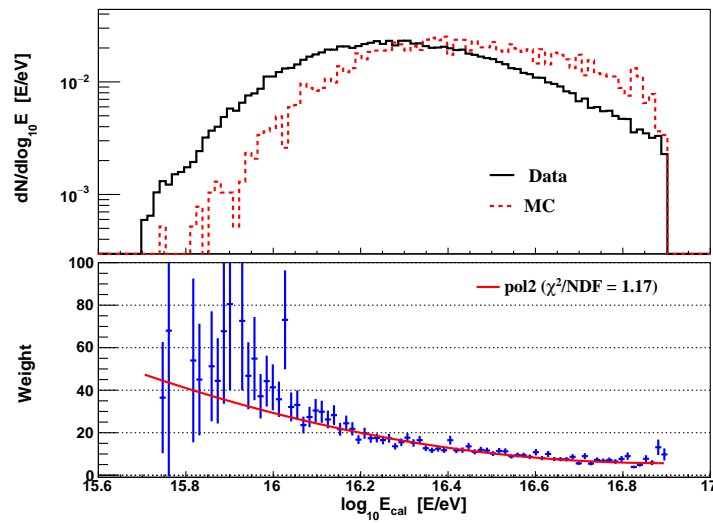
Figure 7.1: In the upper panel the $\log_{10}E_{cal}$ normalized distributions for both the data (black) and the Monte Carlo (red). The lower panel shows the ratio of the data to Monte Carlo and the red line represents the fit as used for the re-weighting.
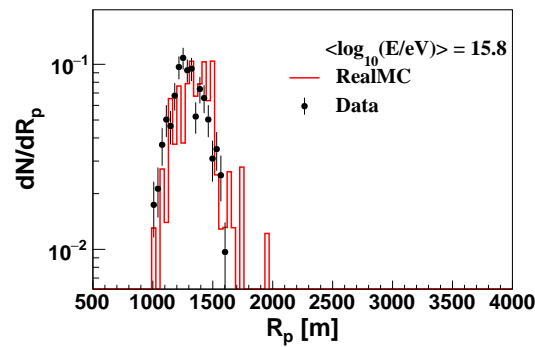

(a)
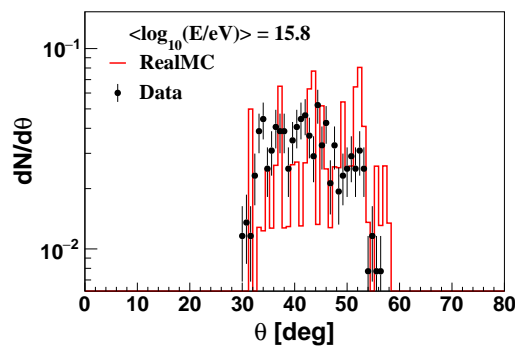
(b)

Figure 7.2: The distribution of (a) R_p and (b) zenith angle for showers with calorimetric energies in the range $10^{15.7} - 10^{15.8}$ eV compared for both data (black) and Monte Carlo (red).

needs to be corrected for the bias it shows as a function of the generated Cherenkov light comparing to the full CORSIKA simulation as can be seen in Fig. 5.10a. For all simulated

(a)

(b)
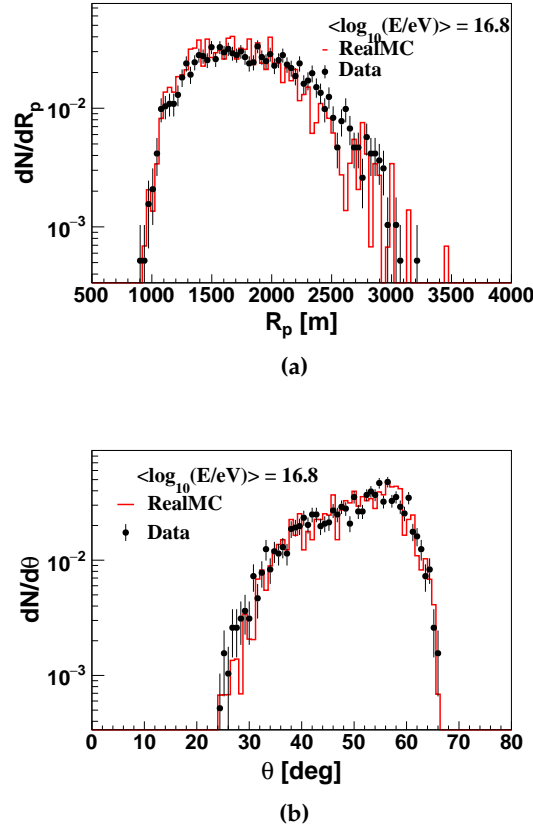
Figure 7.3: The distribution of (a) R_p (b) zenith angle for showers with calorimetric energies in the range $10^{16.8} - 10^{16.9}$ eV compared for data (black) and Monte Carlo (red) .

showers in the RealMC library with the generated Cherenkov fraction more than 85% X_{max} is shifted by the biased value calculated from Eq. (5.1). Then the biases and the resolutions for the reconstructed energy and X_{max} are calculated. In Section 4.4 the bias in the HEAT reconstructed energy and X_{max} are calculated using the showers observed by both HEAT-downward and Coihueco. The first two points at energies $10^{16.9}$ eV and $10^{17.1}$ eV from Fig. 4.11a, Fig. 4.11b, and Fig. 4.11c after selecting only the showers with 70% Cherenkov fraction are compared to what is determined using the RealMC.

7.2.1 Testing the energy reconstruction

The calorimetric energy is the first shower parameter investigated using the RealMC to calculate the effect of the reconstruction process on it. This is done by calculating how much the reconstructed calorimetric energy is shifted from the simulated value in percent, which is calculated as:

$$\langle E^{\text{bias}} \rangle = \left\langle \frac{(E_{\text{cal}}^{\text{rec}} - E_{\text{cal}}^{\text{gen}})}{E_{\text{cal}}^{\text{gen}}} \right\rangle [\%]. \tag{7.1}$$

In Fig. 7.4, the bias in the calorimetric energy as a function of $\log_{10}E_{\text{cal}}^{\text{rec}}$ is calculated using the RealMC simulations is compared to the first two points of the cross-calibration study for HEAT-downward and Coihueco. The bias in the calorimetric energy is parameterized as function of the $\log_{10}E_{\text{cal}}^{\text{rec}}$ by

$$\langle E_{\text{cal}}^{\text{bias}} \rangle [\%] = -6.15 + 1.9(\log_{10}E_{\text{cal}}^{\text{rec}} - 16). \tag{7.2}$$
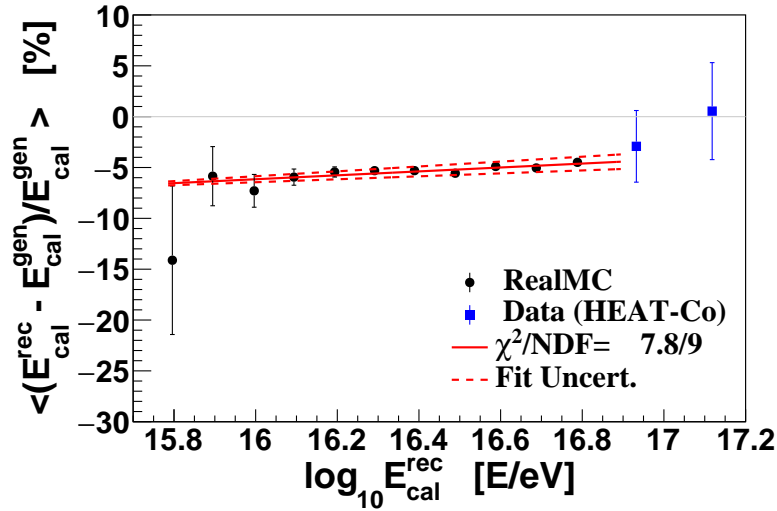
Figure 7.4: The bias in the calorimetric energy reconstructed by the PCGF reconstruction calculated using the RealMC weighted library as a function of $\log_{10}E_{cal}^{rec}$ is represented in the black points together with the parameterization fit (red line). The red dashed lines represent the error propagation of the fit. The two points (blue squares) from the cross-calibration study for HEAT-downward and Coihueco are comparable to the RealMC results.

The energy bias is checked furthermore as a function of different parameters: Cherenkov fraction, generated X_{max}, and the zenith angle. The energy bias is slightly dependent on the Cherenkov fraction and zenith angle. The average bias is around 5.4% at 85% Cherenkov fraction and is 5.2% at $42°$. For the generated X_{max} the bias fluctuates a little between 3% to 15%. The results are in Fig. 7.5, which show equivalent bias values in the same range as that in Fig. 7.4. So the correction of the reconstructed data with the parametrization in Eq. (7.2) is sufficient. The energy resolution is calculated as the standard deviation of the bias Eq. (7.1), as shown in Fig. 7.6.

7.2.2 Testing X_{max} reconstruction

The main investigation observable in this study is the X_{max}. It is a significant step in this analysis to estimate the bias caused by the PCGF reconstruction in the X_{max}. This bias represents the difference between the reconstructed and the generated X_{max}. The mixed composition RealMC, mixture of 50% proton and 50% iron, is used to estimate the bias in X_{max} that is shown in Fig. 7.7 together with the two points from the cross-calibration study for HEAT-downward and Coihueco. The data is corrected with the parametrization of the fit function shown as red line in Fig. 7.7 by

$$\langle X_{max}^{bias}\rangle[\mathrm{g/cm^2}] = 7.52 - 2.57(\log_{10}E_{cal}^{rec} - 16). \tag{7.3}$$

The X_{max} bias as a function of different shower parameters, Cherenkov fraction, generated X_{max}, and the zenith angle can be seen in Fig. 7.8. For the three parameters the bias is within the correction values, which are calculated from Eq. (7.3). Only at large zenith angles of $\geq 50°$, the bias starts to increase up to $\approx 20\,\mathrm{g/cm^2}$. This can be attributed to the incomplete performance of the analytical Cherenkov model used in $\overline{\mathrm{Off}\underline{line}}$ to reconstruct the Cherenkov light.

The X_{max} resolution is an important factor as it indicates the detector resolution, which is critically needed for example to correct the X_{max} fluctuations measured in the data. The
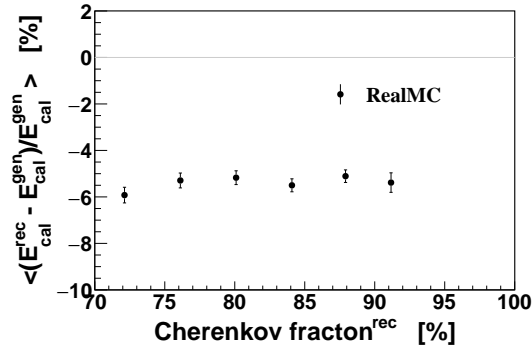
(a)
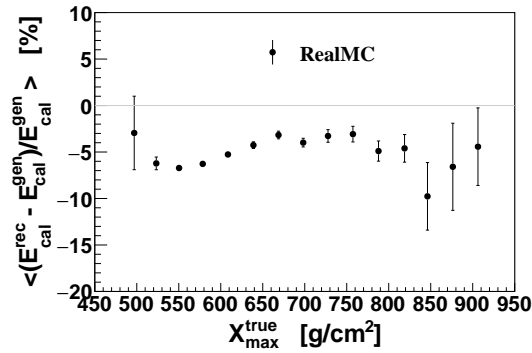
(b)
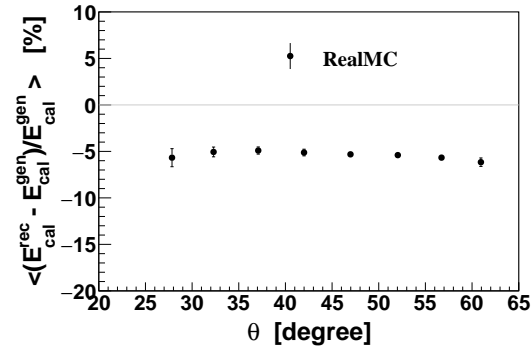
(c)

Figure 7.5: The calorimetric energy bias plotted as a function of (a) Cherenkov fraction, (b) true X_{max}, and (c) zenith angle.

resolution of the detector is simply the standard deviation of the difference between the reconstructed and the generated X_{max}. The detector resolution is shown in Fig. 7.9 evaluated in reconstructed calorimetric energy bins. In the lowest energy bin, $10^{15.8}$ eV, the resolution is about 67 g/cm^2 the resolution values improved with increasing the shower energy to reach 40 g/cm^2 at energy of $10^{16.8}$ eV. These values of the HEAT resolution calculated using the RealMC are comparable to what measured using HEAT in downward mode and Coihueco, which indicate how well the RealMC reproduce the reality of the data and correctly simulate the detector. The observed $\sigma(X_{\mathrm{max}})$ can be corrected for the detector resolution given by the function:

$$\mathrm{Res}_{\mathrm{det}}[\mathrm{g/cm}^2] = 61.6 - 24.5(\log_{10}\mathrm{E}_{\mathrm{cal}}^{\mathrm{rec}} - 16). \tag{7.4}$$
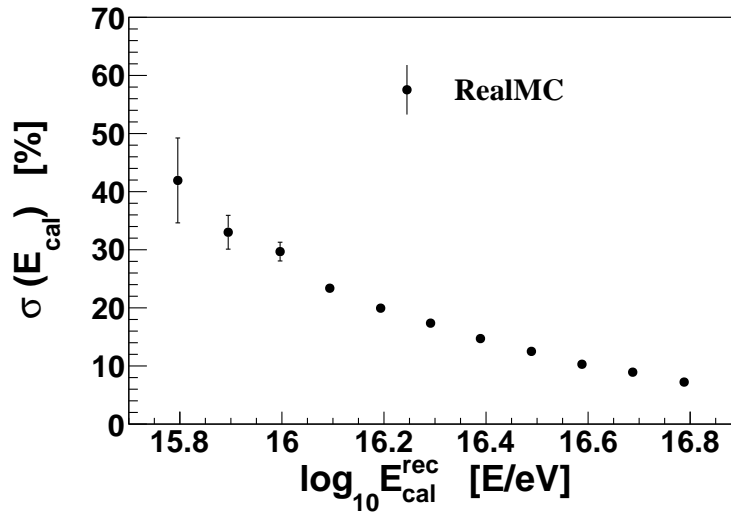
Figure 7.6: Energy resolution of the HEAT reconstructed by PCGF reconstruction as a function of $\log_{10} E_{cal}^{rec}$ calculated with the RealMC.
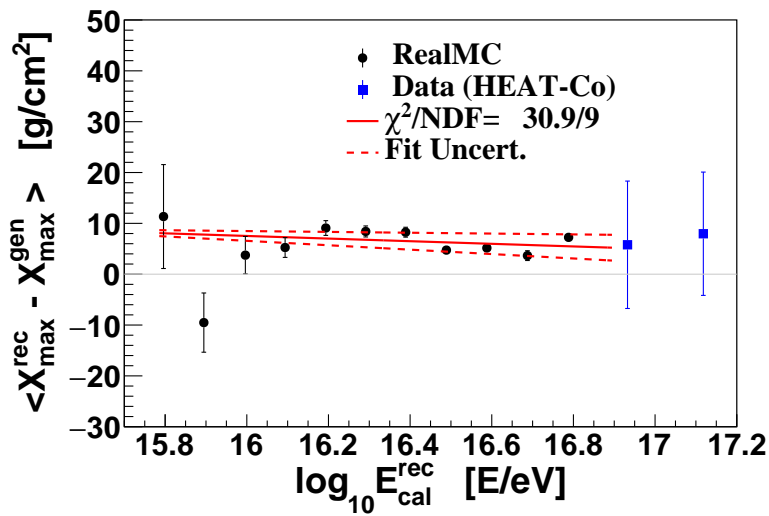

Figure 7.7: The bias in the shower maximum depth is estimated using the RealMC mixed composition weighted library as a function of $\log_{10} E_{cal}^{rec}$ is represented in the black points together with the parameterization fit (red line). The red dashed lines represent the error propagation of the fit. The two points (blue squares) from the cross-calibration study for HEAT-downward and Coihueco are comparable to the RealMC results.

The detector resolution is determined from RealMC using three samples with different mass composition, pure proton, pure iron, and mixture sample of 50% proton and 50% iron. In the three sample the resolution shows very close values in each energy bin, as seen in Fig. 7.10. This result reflect the power of the used FoV selection developed for this study, where the different nuclei from light to heavy are selected without bias and with the same efficiency.
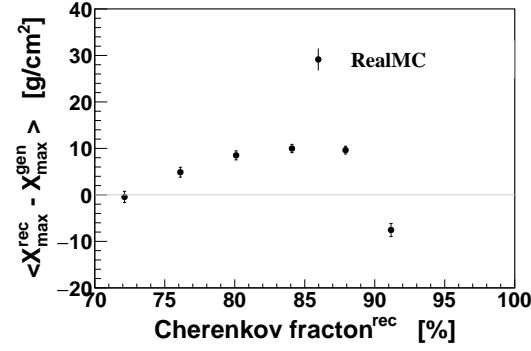
(a)
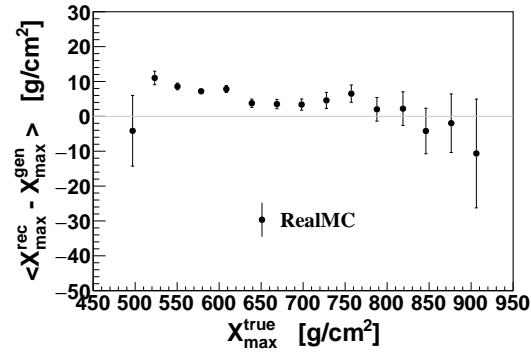
(b)
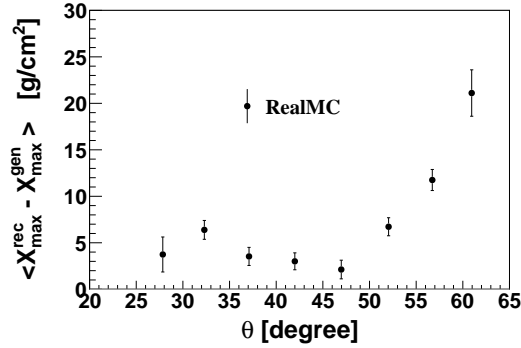
(c)

Figure 7.8: The bias in the reconstructed X_{max} plotted as a function of (a) Cherenkov fraction, (b) true X_{max}, and (c) zenith angle.

7.3 End-to-end analysis cross-check

The stability of the analysis sequence can be cross-checked using the Monte Carlo simulation by estimating the $\langle X_{max} \rangle$ and $\sigma(X_{max})$ in both reconstructed and generated level and compare the results. This is done by splitting the Monte Carlo library into three segments: the first sample consists of pure proton showers, the second consists of pure iron, and in the third one a mixture of half proton half iron. Each sample go through the same selection used with the data but each sample has its own fiducial FoV selections, which are determined by re-tuning the FoV analysis specifically for each sample. The fiducial FoV boundaries for the
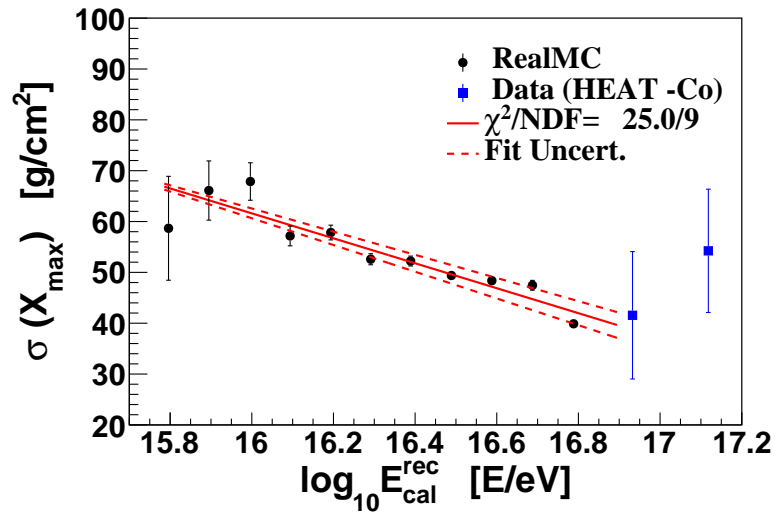
Figure 7.9: The detector resolution is estimated using the RealMC mixed composition weighted library as a function of $\log_{10}E_{cal}^{rec}$ is represented in the black points together with the parameterization fit (red line). The red dashed lines represent the error propagation of the fit. The two points (blue squares) represent the detector resolution calculated from the cross-calibration study for HEAT-downward and Coihueco. The points from RealMC results and HEAT-downward are comparable to each other.
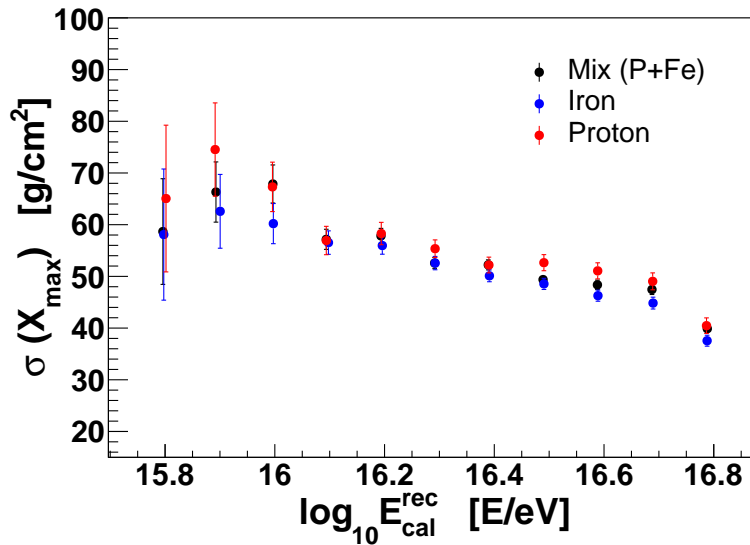

Figure 7.10: The detector resolution as estimated using the RealMC with different composition the black points is a mixture of 50% proton and 50% iron, the red dots represent the pure proton, and the blue dots represent a pure iron calculations. The resolution has similar values in the three samples.

pure proton, pure iron, and mixture are shown in Fig. 7.11. Testing the whole analysis, each sample is corrected for the X_{max} and energy bias as well as the detector resolution.

The estimated $\langle X_{max} \rangle$ and $\sigma(X_{max})$ for the three different composition samples compared to the moments of the generated level from CONEX simulations with SIBYLL-2.3C before and after the detector simulations are shown in Fig. 7.12 and Fig. 7.13. First for the $\langle X_{max} \rangle$ and within the detector level, the measured and generated values shows a good agreement in case of pure proton and agree within $5 \, \text{g/cm}^2$ for pure iron sample. For the mixed sample,
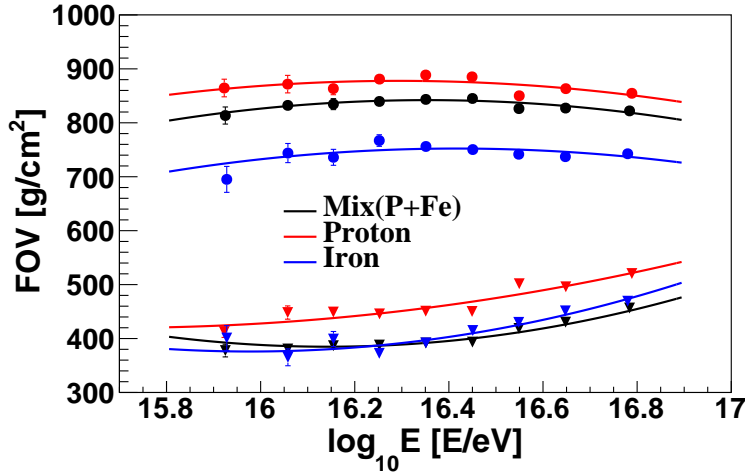
Figure 7.11: The fiducial FoV boundaries as calculated for different mass composition samples, proton (red), iron (blue) and mixture of 50% proton and 50% iron (black).

there are indications for a slight deviation between the reconstructed and the generated $\langle X_{\max} \rangle$ with residuals values between $-5\text{g}/\text{cm}^2$ and $+10\text{g}/\text{cm}^2$. For the $\sigma(X_{\max})$ there is a $5\text{g}/\text{cm}^2$ agreement between the measured and the generated values in both pure proton and pure iron sample. A slightly larger bias is observed for the mixed composition of about $-5\text{g}/\text{cm}^2$. In the pure CONEX comparison level, before the detector simulation, iron showers showed better performance than the proton especially in case of $\sigma(X_{\max})$. The deviation between the reconstructed and the true CONEX simulation shows a mass and energy dependence. This observed bias can assigned to the uncertainty in the invisible energy correction see Section 8.2 and/or neglecting the acceptance correction in the analysis. The analysis sequence works well within the detector level, however, in the true CONEX level there is an increasing bias with the energy. The bias can be described for $\langle X_{\max} \rangle$ by

$$\Delta X_p \, [\text{g}/\text{cm}^2] = \left(X_{\max}^{\text{rec}} - X_{\max}^{\text{conex}} \right)_p$$
$$= 2.9 + \frac{15.17(\log_{10}E_{\text{cal}} - 16)}{0.1129 \, log_{10}^2 E_{cal} - log_{10}E_{cal} - 16}, \tag{7.5}$$

$$\Delta X_{Fe} \, [\text{g}/\text{cm}^2] = \left(X_{\max}^{\text{rec}} - X_{\max}^{\text{conex}} \right)_{\text{Fe}} = 152.6 - 8.77 \log_{10}E_{\text{cal}}. \tag{7.6}$$

For $\sigma(X_{\max})$ residuals values for iron almost zero and for proton about $-10\text{g}/\text{cm}^2$. The average bias of the proton and iron compositions, $(\Delta X_p + \Delta X_{Fe})/2$, for both $\langle X_{\max} \rangle$ and $\sigma(X_{\max})$ in CONEX level are fully taken into account as systematic uncertainties.
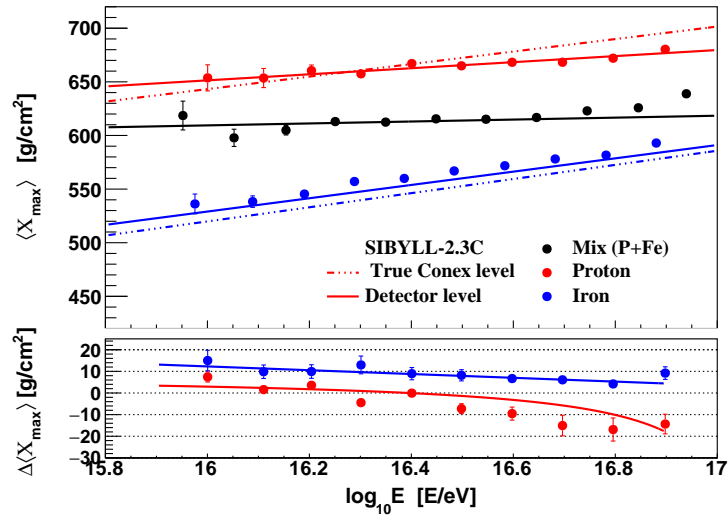
Figure 7.12: The first moment of the X_{max} distribution for the reconstructed showers (dots) compared to the one of the generated showers in the detector level (sold lines) for three different mass compositions: pure proton (red), pure iron (blue), and mixture of proton and iron (black). Further cross-check with the true CONEX values before the detector simulation (dashed lines). This simulation is based on CONEX with SIBYLL-2.3C as hadronic interaction model. In the lower panel is the residuals between the measured and the CONEX generated values for the proton and iron samples.
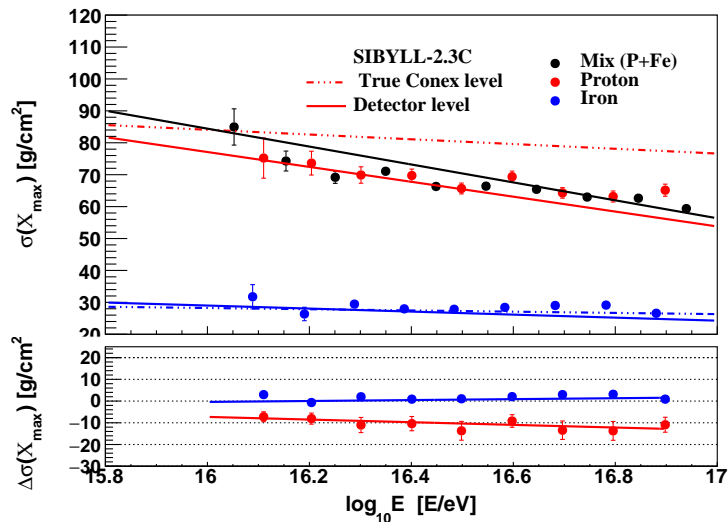
Figure 7.13: The width of the X_{max} distribution for the reconstructed showers (dots) compared to the one of the generated showers (sold lines) for three different mass compositions: pure proton (red), pure iron (blue), and mixture of proton and iron half of each (black). Further cross-check with the true CONEX values before the detector simulation (dashed lines). This simulation is based on CONEX with SIBYLL-2.3C as hadronic interaction model. In the lower panel is the residuals between the measured and the CONEX generated values for the proton and iron samples.

CHAPTER 8

Stability and systematic uncertainty of $X_{\mathbf{max}}$

This chapter covers the last step in this analysis where the data is corrected with the calculated biases estimated using the RealMC simulations. Then the two moments of the $X_{\max}$ distribution $\langle X_{\max} \rangle$ and $\sigma(X_{\max})$ are measured for the reconstructed showers observed by HEAT telescopes of Pierre Auger Observatory. Also the stability of determining the mean of the $X_{\max}$ distribution and the systematic uncertainty are studied.

8.1 Stability of $\langle X_{\mathbf{max}} \rangle$

Here I want to study and quantify remaining imperfections of the PCGF simulation and reconstruction chain based on a data-driven approach. For that, the dependence of the measurements on the zenith angle of the showers is studied in energy bins. The selected data sample has been split depending on the Cherenkov light and the zenith angle into four subsamples: the first sample contains all showers inclined by angles less than or equal $44°$ and have Cherenkov light $\leq 84\%$ and in the second subsample the same inclination as the showers of the first sample $\leq 44°$ but at higher Cherenkov light, more than 84%. The other two samples are the complementary of these two samples,where the more inclined showers have Cherenkov light less than 84% in the third sample and the more inclined and higher Cherenkov showers are grouped in the last sample. The Table 8.1 summarize the four samples together with their color code. The values of $44°$ and 84% are the median of the zenith angles distribution and Cherenkov fraction light distribution respectively. This cross-check considers both the zenith angle and Cherenkov fraction together to study the dependence of the moments of $X_{\max}$ distribution on them as both parameters are correlated and the parameterization of the Cherenkov model used in the $\overline{\text{Off}}\underline{\text{line}}$ is not perfect in describing this dependence. It is acceptable to neglect this correlation in case of the hybrid reconstruction as the standard hybrid selections subtract most of the Cherenkov light as background and is not used in the measurements at all. But for the PCGF reconstruction this is more complex. For that reason and for simplicity, the data split into four subsample depending on both zenith and Cherenkov light fraction. In Fig. 8.1 a description for the splitting of the data sample on the scattered plot of zenith and Cherenkov events, in which each subsample has an indicator using a different letter and color. The result of this cross-check can be seen in Fig. 8.2 and Figure 8.3, for both $\langle X_{\max} \rangle$ and $\sigma(X_{\max})$ respectively. For $\langle X_{\max} \rangle$, the
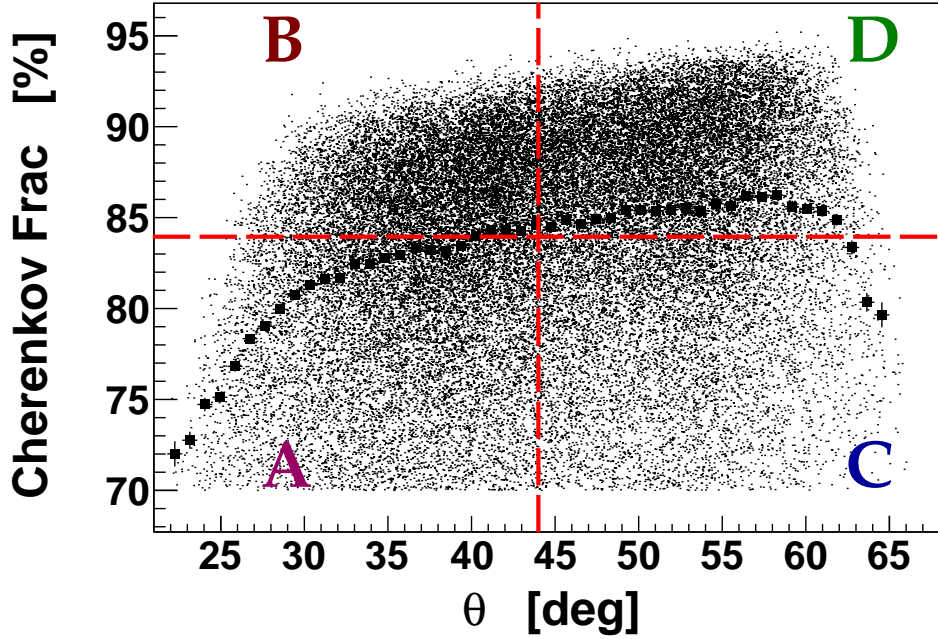
Figure 8.1: The correlation between the zenith angle and the Cherenkov light fraction. The selected data sample is split into four subsamples A, B, C, and D in the Cherenkov - zenith phase space to study the stability of $\langle X_{\text{max}} \rangle$.

four samples show dependence on the inclination and the Cherenkov light fraction of the shower. This dependence is obvious in the energies lower than $10^{16.6}$ eV for both observed data showers and the RealMC showers. The dependence is very significant in the case of $\sigma(X_{\text{max}})$ for both, data and the Monte Carlo events, which show the same behavior in all the energy bins. The cause of this large dependence on the inclination of the shower and its changes with the fraction of Cherenkov light points to remaining problems of the Cherenkov model used during the reconstruction and simulation. The investigation in this way will certainly be possible only if there is a new comprehensive model simulate and reconstruct the Cherenkov shower in $\overline{\text{Off}}\underline{\text{line}}$. Until then, $\langle X_{\text{max}} \rangle$ and $\sigma(X_{\text{max}})$ are used as measured in the detector for data and Monte Carlo, and a comparison on CONEX level is subject to extra uncertainties. For $\sigma(X_{\text{max}})$ we will at this moment not quantify those extra uncertainties, and, thus, refrain from showing $\sigma(X_{\text{max}})$ on CONEX level.

Table 8.1: The data sample is split into four subsamples depending on the zenith angle and Cherenkov light. Here is a brief description of these subsamples together with its color code as used in Fig. 8.2 and Fig. 8.3.

Sample	Representing	
	Zenith [deg]	Cherenkov fraction [%]
● A	≤ 44	≤ 84
● B	≤ 44	> 84
● C	> 44	≤ 84
● D	> 44	> 84
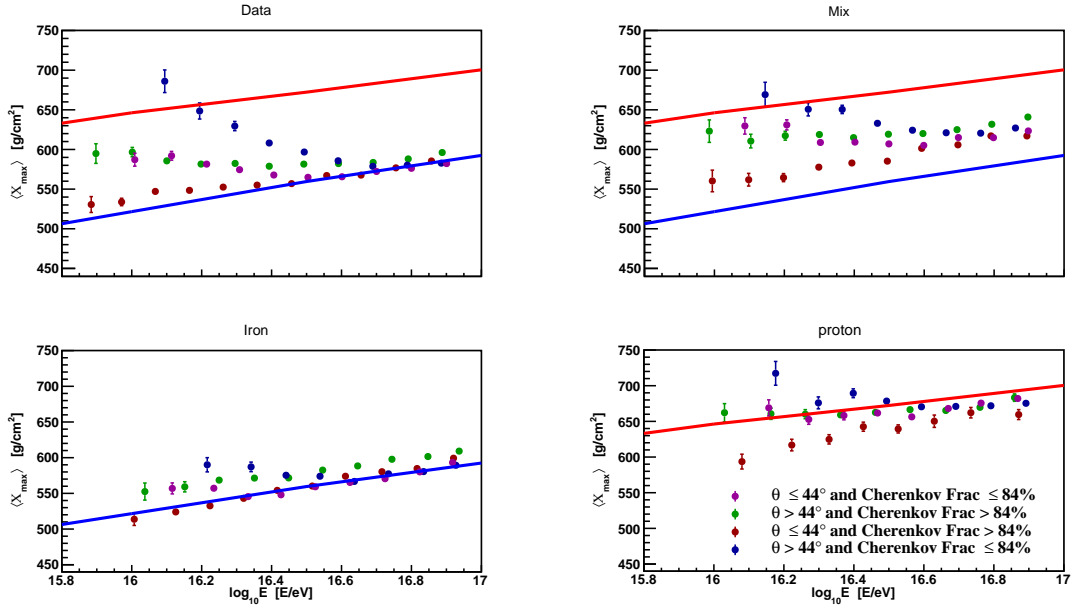
Figure 8.2: The dependence of $\langle X_{\max} \rangle$ on the inclination of the shower and the Cherenkov light for four subsamples, see Table 8.1, are studied in data and the RealMC for different mass compositions proton, iron and mixture of 50%P : Fe. The results from data and RealMC are compared to the true proton (red line) and iron (blue line) $\langle X_{\max} \rangle$ values from CONEX simulations with SIBYLL-2.3C before the detector simulation. There is a difference between the four subsamples this difference appears mostly for energies lower than $10^{16.6}$eV. The dependence of $\langle X_{\max} \rangle$ on the zenith angle and the Cherenkov light shows the same behavior in the data and the RealMC.
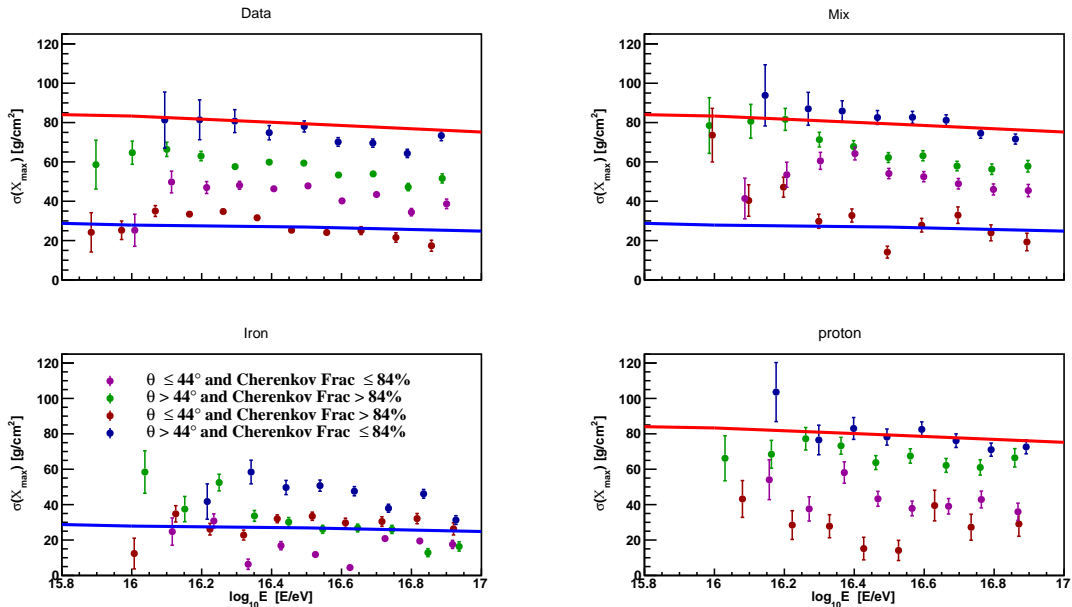

Figure 8.3: The width of $X_{\max}$ distribution, $\sigma(X_{\max})$, is highly depending on the inclination and the Cherenkov light of the shower. This discrepancy equally appears in data and MC over all energy bins in the four studied subsamples, see Table 8.1.

8.2 Data correction

The reconstructed energy of the shower is always incomplete as the reconstructed energy represents only the calorimetric energy, E_{cal}, which is the total deposited energy in the atmosphere, while the part of energy carried by the neutrinos, the high energy muons and used to break nuclei in the atmosphere is missing. In order to calculate the true energy of the primary particle, the calorimetric energy is scaled by a factor representing the invisible energy f_{inv} [118–121] as

$$E_{\text{true}} = f_{\text{inv}} E_{\text{cal}}. \tag{8.1}$$

This invisible factor is depending on the mass and energy of the primary particle. For this reason simulated showers are used in the calculation in the same energy range as the measurements $10^{15.7}$ eV to $10^{16.9}$ eV. The invisible energy factor, which will be used to calculate the total energy is shown in Fig. 8.4 for three different compositions: pure proton, pure iron, and mixture of proton and iron (50% for each). The missing energy fraction is then calculated as the average of both proton and iron, $f_{\text{inv}} = (f_{\text{inv}}^{\text{p}} + f_{\text{inv}}^{\text{I}})/2$.

   The showers observed by HEAT and reconstructed by the PCGF are corrected shower by shower for the biases and the detector resolution, which are calculated using the RealMC. The energy is first corrected, then the X_{max}. For the energy, the unbiased true energy is calculated as

$$E_{\text{true}}[\text{unbiased}] = E_{\text{cal}} f_{\text{inv}} f_{\text{bias}}, \tag{8.2}$$

where

$$f_{\text{bias}} = 1 - \langle E_{\text{cal}}^{\text{bias}} \rangle, \tag{8.3}$$

and the bias in the calorimetric energy is given by Eq. (7.2). Secondly, the X_{max} is corrected for the bias that is observed between the reconstructed and generated X_{max} using the RealMC showers as discussed in Section 7.2.2. The bias shows positive values as function of $\log_{10} E_{\text{cal}}^{\text{rec}}$, which mean that the reconstructed values of X_{max} are higher than the true value. For that reason, all the observed shower maximum are shifted by the value given in Eq. (7.3) as

$$X_{\text{max}}^{\text{corr}} = X_{\text{max}}^{\text{rec}} - \langle X_{\text{max}}^{\text{bias}} \rangle. \tag{8.4}$$

The width of the X_{max} distribution, $\sigma(X_{\text{max}})$, is corrected for the effect of the detector resolution that is calculated in Section 7.2.2 with help of time dependent Monte Carlo simulation. The $\sigma(X_{\text{max}})$ of the observed showers after subtract the detector resolution is given by

$$(\sigma(X_{\text{max}}))^{\text{corr}} = \sqrt{((\sigma(X_{\text{max}}))^2 - Res_{det}^2)}, \tag{8.5}$$

where Res_{det} is given by Eq. (7.4). All these corrections are considered within the calculations and for the extreme case, are fully included in the systematic uncertainty, which discusses in the next section.

8.3 Systematic uncertainties

The uncertainty of determining the X_{max} of showers observed by HEAT telescopes is estimated form the most potential sources. The contribution of each source is calculated in X_{max} as well as for $\sigma(X_{\text{max}})$. Some of these sources required re-reconstruct the selected data set to calculate their effects.
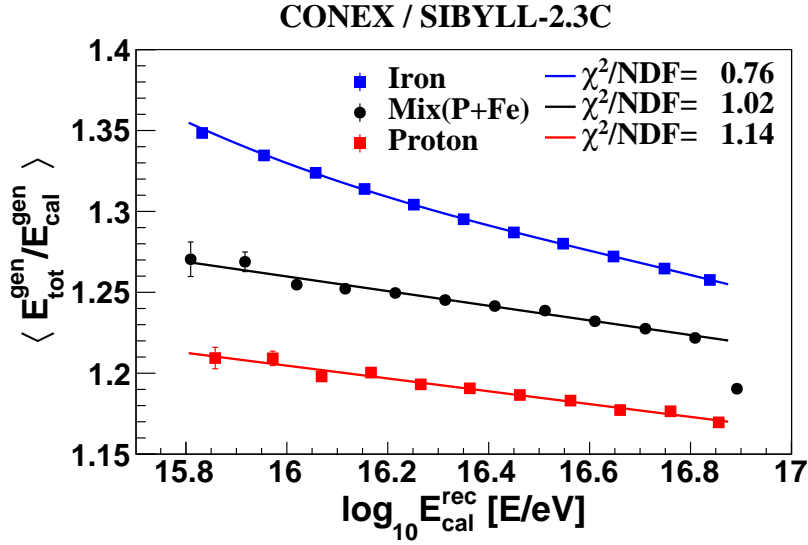
Figure 8.4: The invisible energy factor calculated using CONEX simulated showers with SIBYLL-2.3C for different primary compositions. In red is proton, in blue is iron, and 50% mixed proton and iron is black.

8.3.1 Energy uncertainty

The systematic uncertainty of the energy scale of Pierre Auger Observatory is 14% [120], which is sum of different contributions. In Section 7.2.1 the RealMC shows an energy bias parametrized as Eq. (7.2), the true energy of the showers are corrected for the effect of this bias during the analysis, however, this energy bias will also be fully considered as systematic uncertainty. The total uncertainty of the energy is the quadratic sum of both energy scale and energy bias as

$$\delta E_{tot} = \sqrt{\delta E_{scale}{}^2 + \delta E_{bias}{}^2}. \tag{8.6}$$

8.3.2 Systematic uncertainties of X_{max} and resolution

The most important source of systematic uncertainties for the measurement have been studied. Here is a description of the individual effects.

Reconstruction

The reconstruction used to reconstruct the observed showers is tested by using the RealMC and the bias observed between the reconstructed and the generated X_{max} considered as correction for the observed events. But the source of this bias can be a failure in the simulation/reconstruction sequence. For that reason, this bias is considered as a systematic uncertainty in X_{max} on one side as:

$$\delta X_{max}^{bias} = {}^{+\langle X_{max}^{bias}\rangle}_{-0} \, [g/cm^2], \tag{8.7}$$

where $\langle X_{max}^{bias}\rangle$ is given by Eq. (7.3). This represents by the blue dashed lines in Fig. 8.6. For the detector resolution, the contribution of the reconstruction counts only from the uncertainty of the parametrization in Eq. (7.4) so the uncertainty in the detector resolution is given as:

$$\delta Res_D = {}^{+\delta fit}_{-\delta fit} \, [g/cm^2]. \tag{8.8}$$

This effect is very small and can be seen in Fig. 8.7 as the dashed blue band. No more contributions from the reconstruction are counted, where the reconstruction was already

tested many times for different configurations and the reconstruction used here is the most stable and accurate one. So the estimated bias from the Monte Carlo is sufficient to quantify the remaining uncertainty.

Analysis cross-check

The analysis chain was cross-checked for different mass compositions from the RealMC and compared to ones from the generated level before the detector simulation. This end-to-end cross-check results are shown in Fig. 7.12 and Fig. 7.13. There was a slight deviation in the case of iron composition which increases in case of proton. For that an average bias will be considered here as an potential additional mass-sensitive systematic error from the analysis chain for both $\langle X_{\mathrm{max}} \rangle$ and $\sigma(X_{\mathrm{max}})$ as:

$$\delta X_{\mathrm{max}}^{\mathrm{anal}} = \pm (\Delta X_p + \Delta X_{Fe})/2 \,[\mathrm{g/cm^2}], \text{ and} \tag{8.9}$$

$$\delta(\sigma(X_{\mathrm{max}}))_{\mathrm{anal}} = {}^{+5}_{-0} \,[\mathrm{g/cm^2}], \tag{8.10}$$

where ΔX_p and ΔX_{Fe} are given by Eq. (7.5) and Eq. (7.6) respectively. This end-to-end cross-check has a contribution to the systematic uncertainty represented by the dotted violet lines in Fig. 8.6. These two lines cross each other at point $\log_{10}E = 16.7$ but this does not mean that the uncertainty is zero at this point.

Atmosphere description

For this analysis, which is based only on the observations of HEAT telescopes where the energies of the observed showers are less than 10^{17} eV, which means typical showers are at very close distance to the telescopes, the error in measuring X_{max} due to the atmospheric fluctuations is expected to be very small. The effect of the aerosols on X_{max} measurements is studied by shifting the Vertical Aerosol Optical Depth, VAOD, by its uncertainty and calculate the effect on $\langle X_{\mathrm{max}} \rangle$ and $\sigma(X_{\mathrm{max}})$. The selected data set is re-reconstructed twice with VAOD $\pm \sigma$ the effect can be seen as the green solid lines in Fig. 8.6 and the green shaded area in Fig. 8.7. As expected, the impact on X_{max} measurements is very small, it is about $\pm 4 \mathrm{g/cm^2}$ at 10^{17} eV and $\approx \pm 1 \mathrm{g/cm^2}$ at $10^{15.8}$ eV for the mean reconstructed X_{max}. The contribution in the detector resolution can be neglected it is about $0.6 \mathrm{g/cm^2}$ at lowest energy bin and $\approx 1 \mathrm{g/cm^2}$ in the highest energy bin. These changes can be only a reconstruction fluctuations, however, as extrema case they are fully included as systematic uncertainty in $\langle X_{\mathrm{max}} \rangle$ and $\sigma(X_{\mathrm{max}})$.

Cherenkov model

The performance of the Nerling-Cherenkov model used to reconstruct the Cherenkov light in this analysis is cross-checked using another available model in $\overline{\text{Off}}\underline{\text{line}}$, Giller-model. Unsurprisingly, there is a deviation in the X_{max} which increase with energy and for $\sigma(X_{\mathrm{max}})$ the effect was higher. This divination is considered as systematic uncertainty as

$$\delta X_{\mathrm{max}}^{\mathrm{Cher}} = \pm \frac{1}{2}(-83.8 + 5.68 \log_{10}E) \,[\mathrm{g/cm^2}], \text{ and} \tag{8.11}$$

$$\delta(\sigma(X_{\mathrm{max}}))_{\mathrm{Cher}} = {}^{+\frac{1}{2}(-86.4+5.9\log_{10}E)}_{-0} \,[\mathrm{g/cm^2}]. \tag{8.12}$$

This contribution to the systematic represented by the orange line in Fig. 8.6 and the orange doted baned in Fig. 8.7 for $\langle X_{\mathrm{max}} \rangle$ and $\sigma(X_{\mathrm{max}})$ respectively.

Telescope alignment

The uncertainty of the telescope alignment is considered as one of the most important and direct source that can cause bias in the $X_{\max}$ reconstruction. In order to calculate the contribution of alignment of the telescopes into the $X_{\max}$ uncertainty, the data set is re-reconstructed twice with the optical alignment of HEAT telescopes is shifted by $\pm 0.1°$ [114] which is an estimate based on octocopter flights and star tracking. The contribution of this shift represented by the red dashed line in Fig. 8.6 and the red shaded baned in Fig. 8.7 for $\langle X_{\max} \rangle$ and $\sigma(X_{\max})$ respectively. If a shower is closer to the telescope, the effect caused by alignment decreases. Expectedly, the higher energies have the biggest contribution to this systematic uncertainty.

Cloud coverage

A high percentage of clouds obscures the light of the shower and act as a filter for the shallower showers, which is causing a shift in the $\langle X_{\max} \rangle$ towards the lighter components. Using the cloud cut is mandatory for the analysis. For more accuracy, the effect of using different version of the cloud selection is tested and, as expected, this shows zero impact on the $X_{\max}$ uncertainty. This means that the cloud selections used in this analysis, see Table 6.2, are accurate enough and perform the desired task.

8.3.3 Total systematic uncertainties

The total uncertainty in measuring $X_{\max}$ is estimated from combining the most important contributions. The total systematic uncertainty in $X_{\max}$ summed up in quadrature is given by

$$\delta X_{\max}^{\text{tot}} = \sqrt{(\delta X_{\max}^{\text{bias}})^2 + (\delta X_{\max}^{\text{anal}})^2 + (\delta X_{\max}^{\text{cher}})^2 + (\delta X_{\max}^{\text{atmo}})^2 + (\delta X_{\max}^{\text{align}})^2}, \qquad (8.13)$$

The detector resolution is also corrected for these uncertainty, the total detector resolution is given by

$$\delta \text{Res}_{\text{tot}} = \sqrt{(\delta \text{Res}_{\text{D}})^2 + (\delta(\sigma(X_{\max}))_{\text{anal}})^2 + (\delta(\sigma(X_{\max}))_{\text{Cher}})^2 + (\delta \text{Res}_{\text{atmo}})^2 + (\delta \text{Res}_{\text{align}})^2}. \qquad (8.14)$$

All the contributions discussed here are summarized in Table 8.2 for the average energy of $10^{16.4}$ ev.
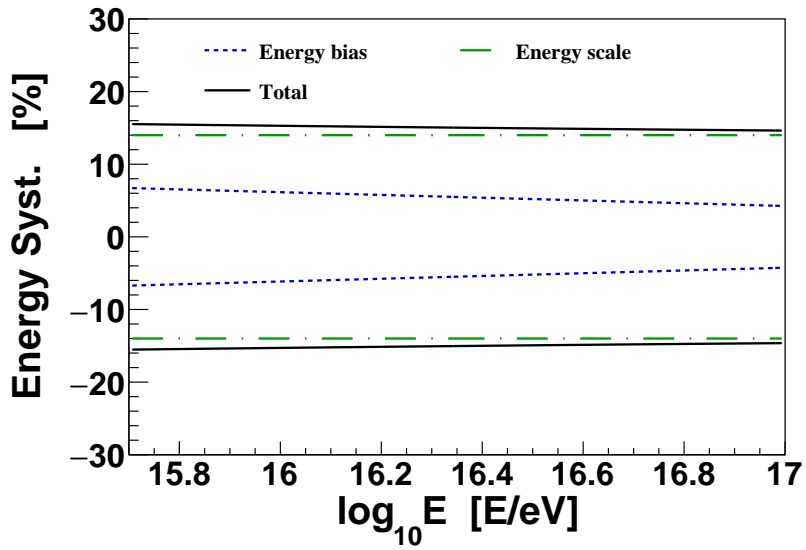
Figure 8.5: Systematic uncertainties in the total energy of the observed showers as a function of $\log_{10}E/eV$. The black solid line represents the quadratic sum of all contributions.
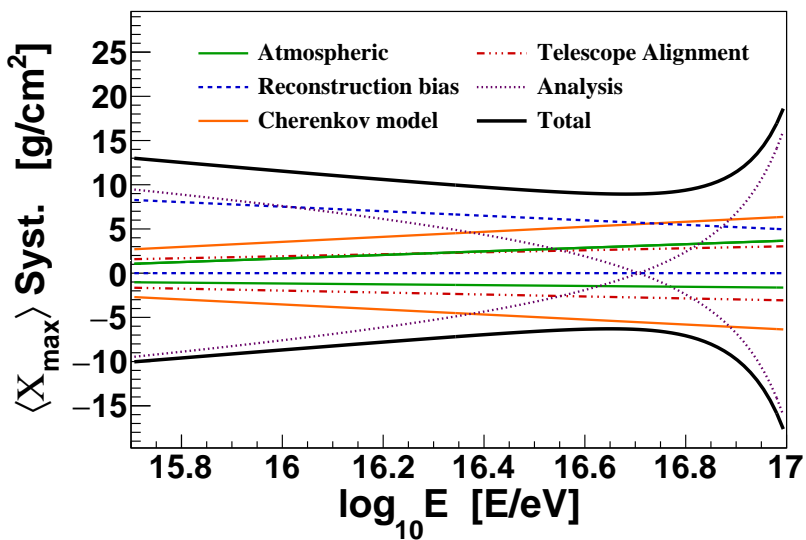

Figure 8.6: Systematic uncertainties in the X_{max} as a function of $\log_{10}E/eV$ are estimated from different contributions: atmospheric, analysis cross-check, telescope alignment. The black solid line represents the quadratic sum of all contributions.
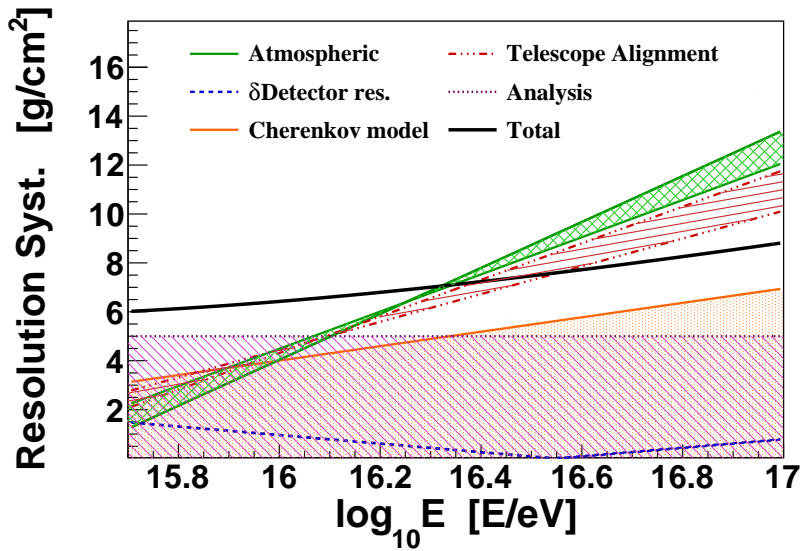
Figure 8.7: Uncertainty of the detector resolution as a function of the logarithmic total energy, estimated from different contributions: atmospheric, analysis cross-check,telescope alignment. The shaded bands denote the estimated systematic uncertainties and the black solid line represents the quadratic sum of all contributions.

Table 8.2: Summary of systematic uncertainties in energy, X_{max}, and resolution corrections at the average energy of $10^{16.4}$ eV.

Type	Value at $10^{16.4}$ eV
Energy systematics in %	
Reconstruction bias	5.39
Energy scale	14
Total	**15**
$\langle X_{max} \rangle$ systematics in g/cm^2	
Reconstruction bias	$+6.49$ -0
Analysis cross-check	$+4.34$ -4.34
Cherenkov model	$+4.6$ -4.6
Telescope Alignment	$+2.36$ -2.41
Atmospheric	$+2.46$ -1.35
Total	**$+9.68$ -6.9**
Resolution systematics in g/cm^2	
Reconstruction	0.02
Analysis cross-check	5
Cherenkov model	5.18
Telescope Alignment	0.58
Atmospheric	0.26
Total	**7.22**

CHAPTER 9

Results

The following chapter describes the results of the cosmic ray mass composition measured by HEAT telescopes of Pierre Auger Observatory in the energy range from $10^{15.8}$eV to 10^{17}eV, using the Profile Constrained Geometry Fit, PCGF, to reconstruct the observed showers. The showers are selected depending on the selection criteria that are discussed in Section 6.2. The selected showers are corrected to the biases as determined using a RealMC simulations as described in Section 7.2 and Section 8.2. The results are presented in energy bins using step of 0.1 of $\log_{10}E/eV$. The total number of events in each bin is shown in Fig. 9.1

9.1 Moments of X_{max}

The moments of the X_{max} distribution, $\langle X_{max} \rangle$ and $\sigma(X_{max})$, were calculated in each energy bin as

$$\langle X_{max} \rangle = \frac{1}{N} \sum_{i=1}^{N} (X_{max,i}^{corr}), \quad \sigma(X_{max}) = \sqrt{\frac{\sum_{i=1}^{N} (X_{max,i}^{corr} - \langle X_{max} \rangle)^2}{N}}. \tag{9.1}$$

Since all bins have sufficient number of events, the statistical error in $\langle X_{max} \rangle$ and $\sigma(X_{max})$ is simply the standard error. First, the measurements of $\langle X_{max} \rangle$ and $\sigma(X_{max})$ are compared on the detector level to the RealMC measurements for pure proton and pure iron compositions. This is very useful since it was found in Section 8.1 that the moments of X_{max} distribution show dependence on the zenith angles and Cherenkov light in both observed data and RealMC showers, which has been discussed in Section 8.1.

9.1.1 The mean depth of the shower maximum

The result of the mean of the shower maximum, $\langle X_{max} \rangle$, as a function of the logarithmic primary energy can be seen in Fig. 9.2 compared to pure proton and pure iron compositions from the RealMC. Both data points and Monte Carlo lines are corrected for the same effects i.e. X_{max} bias. Since the correlation between the Cherenkov light and the zenith angle and the dependence of X_{max} on them is seen in the data as well as in the Monte Carlo, this effect was not added to the uncertainty of the X_{max} nor was it corrected for. The shaded area in Fig. 9.2 represents the systematic uncertainty in the X_{max} scale as displayed in Fig. 8.6, which is dominated by the uncertainty in the reconstruction and the analysis procedures. The error bars represent the statistical uncertainties. The measurements indicate a heavy cosmic ray composition at energies around 10^{17} eV, which become lighter towards lower energies.
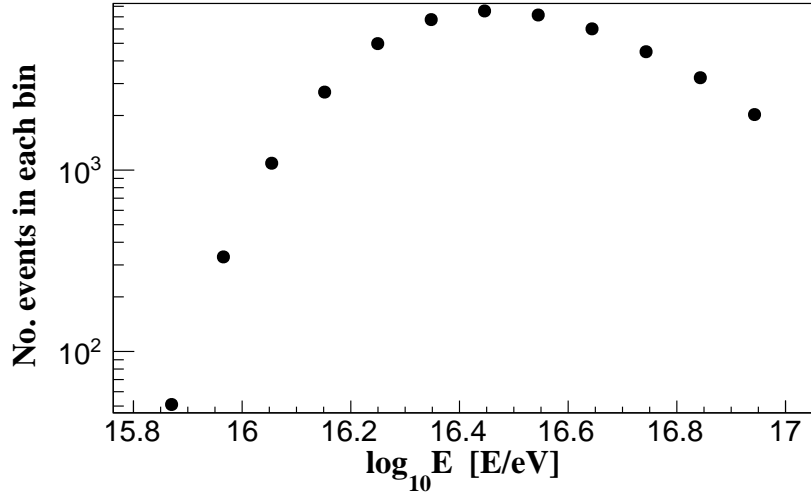
**Figure 9.1:** Number of events in each energy bin.
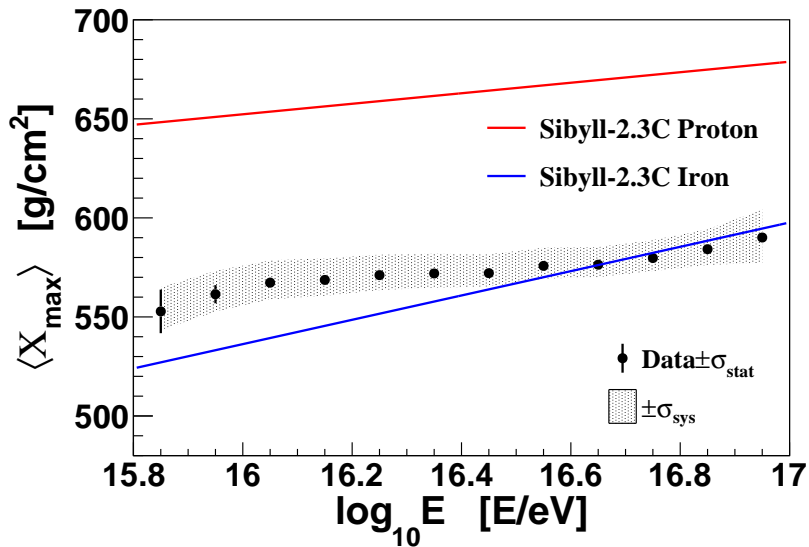
Figure 9.2: The result of $\langle X_{\mathrm{max}} \rangle$ on detector-level after bias correction as a function of the logarithmic energy compared to the reconstructed RealMC simulations of pure proton (red lines) and iron (blue lines) simulated using the hadronic interaction model SIBYLL-2.3C. The dashed area represents the systematic uncertainty.

9.1.2 Fluctuations of the depth of shower maximum

The width of the observed X_{max} distributions at different logarithmic energies is drawn in Fig. 9.3. Where the detector resolution has not been subtracted, and thus is included in the measurements as well as in the reference lines from the Monte Carlo of pure proton and iron. The uncertainties of this measurement are substantial, covering about half the difference between proton and iron. Also the relatively large zenith angle and Cherenkov fraction dependence found both in data and simulations prevents at this moment a detailed interpretation of fluctuations in terms of mass compositions. However the data indicate that there is a tension between the interpretation of the two X_{max} moments results, that is a typical sign for mixed mass composition scenarios in the full range of the analysis. To fully understand these data and to draw more information from the $\sigma(X_{\mathrm{max}})$ measurement, it is
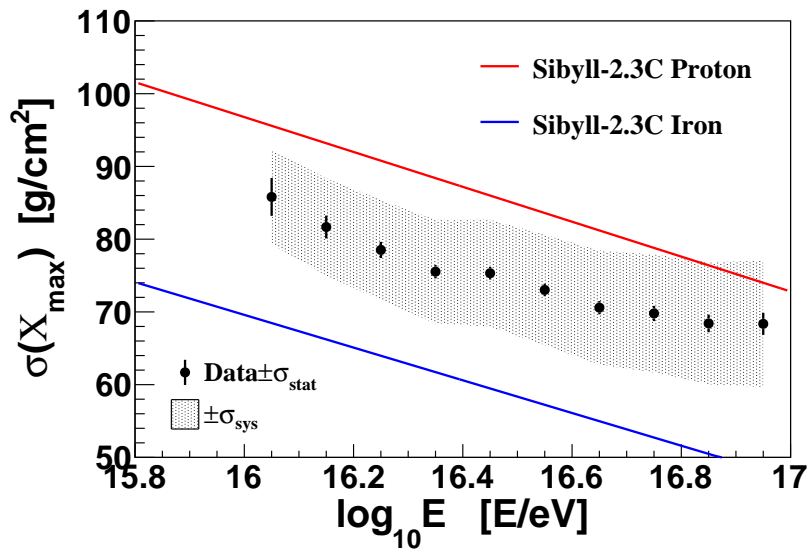
Figure 9.3: The fluctuations of X_{max} on detector-level as a function of the logarithmic energy compared to simulation of pure proton (red lines) and iron (blue lines) simulated using SIBYLL-2.3C as a hadronic interaction model. The detector resolution effect is not subtracted for both data points and simulated lines. The shaded area represents the systematic uncertainty.

required to first fully resolve the underlying limitation of the Cherenkov description in the data reconstruction.

9.2 Comparison to other cosmic ray experiments

In order to compare the results to other experimental data, and arbitrary composition models the $\langle X_{\mathrm{max}} \rangle$ is also shown with all corrections. As a final step it is necessary to determine the size of the remaining zenith dependence and add this to the data. To further study zenith-angle systematics effect, the data is divided into two sets of zenith angles with consideration of keeping the same number of events in the two subsets. Considering that the measurements change as a function of the zenith angle and in order to get an accurate correction of this dependence, I defined an angle θ_m, which is subdivided the data in each energy bin into two equally subsets. By this, there will be no underestimation of the error for different shower energies. The values of θ_m at each energy bin are presented in Table 9.1. And in Fig. 9.4 the dependence of $\langle X_{\mathrm{max}} \rangle$ on the zenith angle of the shower at different primary energies. At maximum, there is about $52 \pm 12.8 \mathrm{g/cm}^2$ at the lowest energy bin difference between the $\langle X_{\mathrm{max}} \rangle$ measured in the two zenith subsets. This difference decreases to only $2.3 \pm 2 \mathrm{g/cm}^2$ at the higher energies. The residuals between the two subsets are parameterized by $(-725.3 + 43.1 \log_{10}\mathrm{E})$, which will be added to the systematic uncertainty of the average X_{max} as $\pm \frac{1}{2}\delta$.

Now after the $\langle X_{\mathrm{max}} \rangle$ corrected for the detection biases and the remaining imperfections are added as systematic uncertainty, the unbiased $\langle X_{\mathrm{max}} \rangle$ can be compared directly with the predictions from air shower simulations. Here I used three different hadronic interaction models which have been tuned to the LHC data EPOS-LHC [57, 122], QGSJET-II.04 [58, 123], and SIBYLL-2.3C [59, 60] to simulate proton and iron induced air showers. The comparison is depicted in Fig. 9.5. The result indicates heavy cosmic ray composition at the heavy knee energy around $8 \times 10^{16}\mathrm{eV}$, and the proton fraction increasing towards lower energies slightly before the knee. In Fig. 9.6 the $\langle X_{\mathrm{max}} \rangle$ measurements of the Pierre
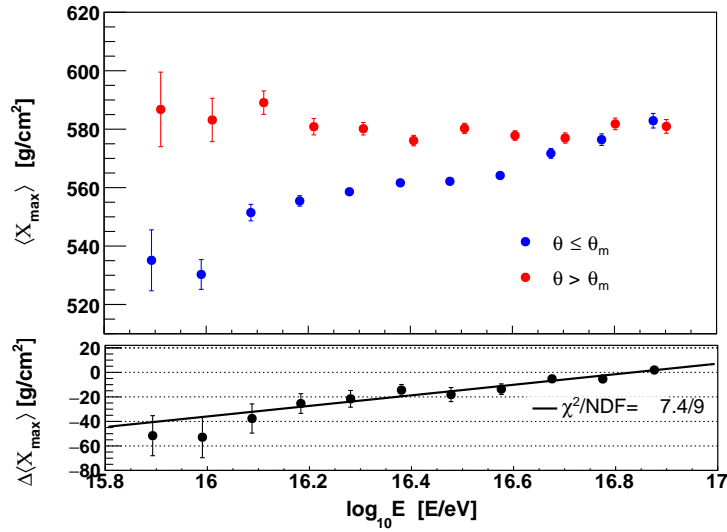
Figure 9.4: The dependence of $\langle X_{\max} \rangle$ on the inclination of the shower at different primary energies. The data is divided into two subsets $\theta > \theta_m$ and $\theta \leq \theta_m$ in each energy bin. In the lower panel the residual between the two sets is shown.

Auger Observatory using two different reconstructions, the hybrid reconstruction in the energy range from $10^{17.2}$eV to $10^{19.6}$eV [124] and the PCGF reconstruction frame, this thesis, in the range from $10^{15.8}$eV to 10^{17}eV are compared. There is a small gap between the hybrid and the PCGF measurements. Most of showers in this energy gap are not dominated by the Cherenkov light nor the fluorescence light. An improved reconstruction technique, which could successfully reconstruct both Cherenkov and fluorescence together is needed to cover this gap in the energy, and to resolve the underlying cause for the observed tension between the two techniques.

Table 9.1: The values of θ_m, which subdivide the data in each energy bin into two equal subsets.

$\log_{10}$(E/eV) bin	θ_m°
15.8 - 15.9	42.2
15.9 - 16.	41.9
16. - 16.1	41.6
16.2 - 16.3	41.9
16.3 - 16.4	42.7
16.4 - 16.5	43.54
16.5 - 16.6	44.85
16.6 - 16.7	46.37
16.7 - 16.8	47.5
16.8 - 16.9	48.89
16.9 - 17	49.48

An overview of the measurement of the mean depth of shower maximum from this analysis and several other experiments can be seen in Fig. 9.7. The experiments consider for the comparison are Telescope Array,TA, [125, 126], HiRes [127], HiRes/MIA [128], Tunka [129], CASA-BLANCA [130], and Yakutsk [131, 132]. The result of this analysis shows a good agreement with Tunka measurements which based also on Cherenkov showers.
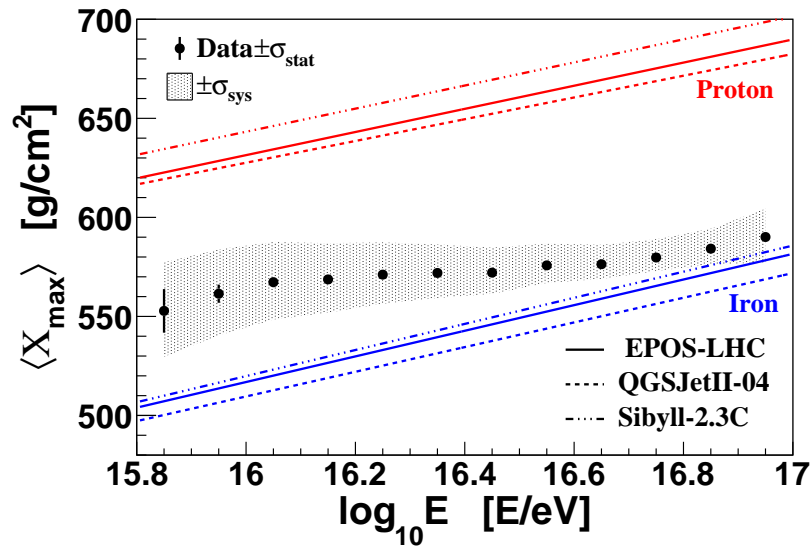
Figure 9.5: Fully corrected $\langle X_{\max} \rangle$ measured by HEAT telescopes compared to the expectation of proton (red lines) and iron (blue lines) compositions using CONEX and different hadronic interaction models.
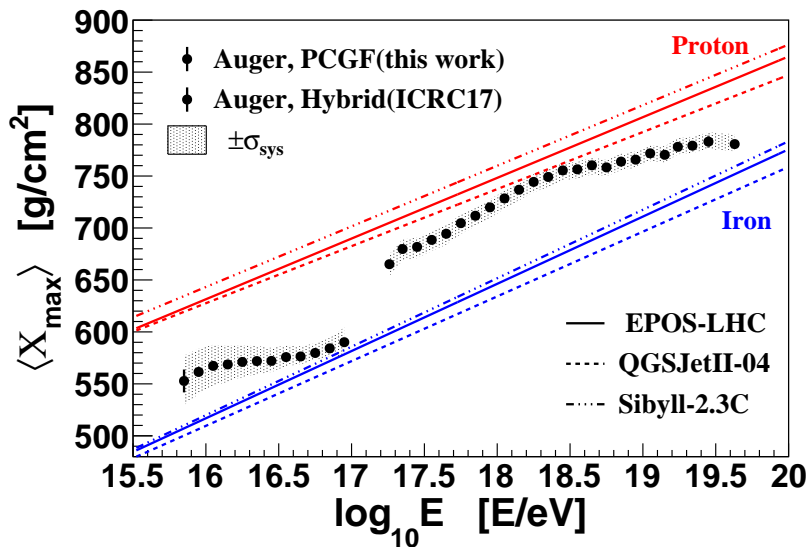

Figure 9.6: The results of the $\langle X_{\max} \rangle$ measured by standard as well as HeCo Auger telescopes in the energy range from $10^{17.2}$eV to $10^{19.6}$eV, and measured by HEAT telescopes alone in the range from $10^{15.8}$eV to 10^{17}eV. The lines indict the expectation of proton (red) and iron (blue) compositions using different hadronic interaction models.

9.3 Average logarithmic mass

Exploiting the superposition model of air showers, which allow linear dependence between the average depth of shower maximum, the logarithmic of the primary energy, and logarith-
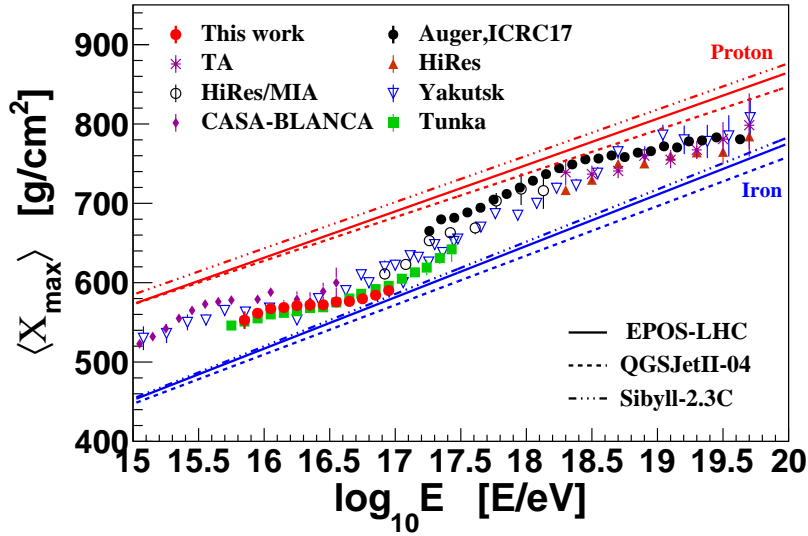
Figure 9.7: $\langle X_{\max} \rangle$ as measured by several experiments compared to the result of this analysis. All points are compared to the values from the hadronic interaction models SIBYLL-2.3C, EPOS-LHC, and QGSJET-II.04 for pure proton and pure iron compositions.

mic mass as described in [55, 56], the $\langle X_{\max} \rangle$ is used to deduce the average logarithmic mass, $\langle \ln A \rangle$, using:

$$\langle \ln A \rangle = \frac{\langle X_{\max} \rangle - \langle X_{\max} \rangle_P}{f_E}, \tag{9.2}$$

$$f_E = \xi - \frac{D}{\ln 10} + \delta \log_{10}(\frac{E}{E_o}), \tag{9.3}$$

where $\langle X_{\max} \rangle_P$ is the mean $X_{\max}$ of proton showers, f_E is energy-dependent parameter, D is the elongation rate[1] [133–135], and ξ and δ are parameters depend on the used hadronic interaction model. These parameters are strongly depending on the interaction model, in Table 9.2 summarize their values for each model at setting $E_o = 10^{19}$eV.

The statistical uncertainty in the $\langle \ln A \rangle$ is calculated as

$$\sigma_{\langle \ln A \rangle}^{stat} = \frac{\sigma_{\langle X_{\max} \rangle}^{stat}}{f_E}, \tag{9.4}$$

where $\sigma_{\langle X_{\max} \rangle}^{stat}$ is the statistical error of $\langle X_{\max} \rangle$. Since $\langle \ln A \rangle$ is a function of the mean depth of shower maximum and the energy, its systematic uncertainty is propagated from the systematic uncertainty in $\langle X_{\max} \rangle$ and the energy as:

$$\delta \langle \ln A \rangle = \sqrt{(\langle \ln A \rangle_{\delta \langle X_{\max} \rangle} - \langle \ln A \rangle)^2 + (\langle \ln A \rangle_{\delta E} - \langle \ln A \rangle)^2}, \tag{9.5}$$

where

$$\langle \ln A \rangle_{\delta \langle X_{\max} \rangle} = \langle \ln A \rangle (\langle X_{\max} \rangle + \delta \langle X_{\max} \rangle), \tag{9.6}$$

$$\langle \ln A \rangle_{\delta E} = \langle \ln A \rangle (\log E + \log(1 + \delta E)). \tag{9.7}$$

The mean of $\ln A$ is shown in Fig. 9.8 using air shower simulations of three different interaction models. The data shows the same trend with the three models, the composition

---

[1]The change of $\langle X_{\max} \rangle$ with the logarithm of energy $D = \frac{d\langle X_{\max} \rangle}{d\log_{10}(E/eV)}$.

is heaviest around $10^{16.9}$ eV and get lighter towards lower energies till it becomes compatible with the $\ln A$ of nitrogen. The three models agree within the systematic uncertainty, however, the heaviest scenario is shown with SIBYLL-2.3C and the lightest average composition come with EPOS-LHC interpretation.

Table 9.2: Values expressed in g/cm^2 of the parameters in Eq. (9.3) for different hadronic interaction models at setting $E_o = 10^{19}$ eV. From [55, 56, 136].

parameter	SIBYLL-2.3C	EPOS-LHC	QGSJET-II.04
D	57.4	56.3	54.2
ζ	-0.56	0.35	-0.42
δ	0.68	1.04	0.69

9.4 Implications for proton-air cross section measurement

One goal of the study presented in this thesis is the measurement of the $\langle X_{\max} \rangle$ of the cosmic ray at lower energy range than the standard range of Pierre Auger Observatory. Extending the Auger energy range towards lower energies produces a new research opportunities between the cosmic ray experiments and the particle accelerators. This thesis opens a new bridge to this type of researches. Following from this, the measure of the cross-section of proton-air collisions, $\sigma_{\mathrm{p-air}}$, at the same energies of the Large Hadron Collider, LHC, can become possible. Measuring the proton-air cross-section at energies around 10^{16} eV from Auger data will be ultimately possible with HEAT-PCGF data. The measurements presented here are the first step in achieving this goal. In parallel, also standard hybrid Auger reconstruction has been used to extend the proton-air cross-section measurements towards lower energies this was demonstrated in my study shown at the ICRC 2015 [137]. In this study, I extended the measurement of the proton-air cross-section of the Pierre Auger Observatory with a new point at lower energies down to $10^{17.8}$ eV, which corresponds to a center-of-mass energy $\sqrt{S_{PP}} \approx 38.7$ TeV. This was performed using new hadronic interaction models available at this time, which have been tuned to the LHC data EPOS-LHC [57] and QGSJET-II.04 [58] as well as the available version of SIBYLL-2.1 [138]. The result of this study is shown in Fig. 9.9, where the two measured points with Auger data are compared to other experimental measurements. The determination of proton-air cross-section at 10^{16} eV will allow a direct comparison with LHC data, since the center-of-mass energies are comparable. It was shown in this thesis that the major remaining challenge for this goal is a better modeling of Cherenkov emission by air shower during the reconstruction. Furthermore, to disentangle the cross-section measurement from the relatively complicated mass composition scenario around 10^{16} eV will also require a complex analysis.

(a)

(b)

(c)
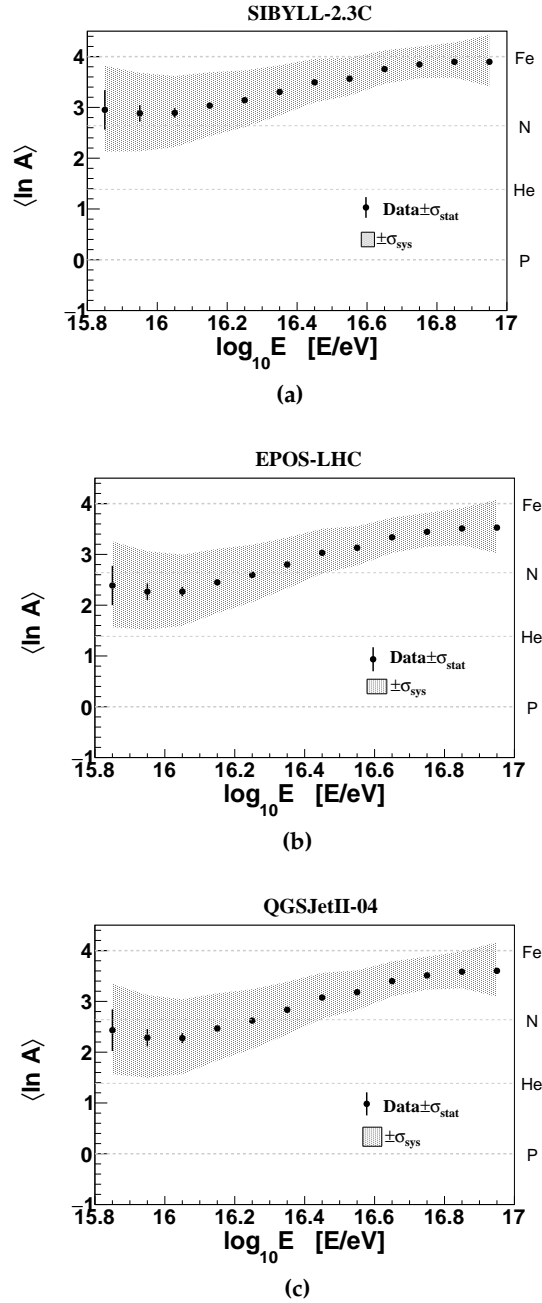
Figure 9.8: The average mass composition $\langle \ln A \rangle$ estimated using (a) SIBYLL-2.3C, (b) EPOS-LHC, and (c) QGSJET-II.04 as hadronic interaction models. The shaded areas represent the systematic uncertainty $\delta \langle \ln A \rangle$ that are propagated from the systematic uncertainty in $\langle X_{\text{max}} \rangle$ and the energy using Eq. (9.5).
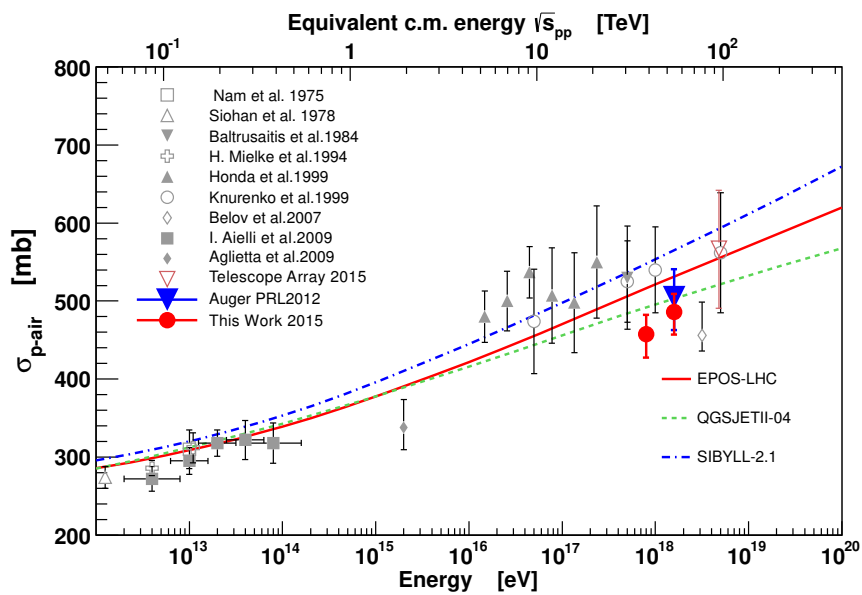
Figure 9.9: The result of extension the measurement of the $\sigma_{\mathrm{p-air}}$ with the Pierre Auger Observatory data compared to previous data and model predictions from EPOS-LHC, QGSJET-II.04, and SIBYLL-2.1.

CHAPTER 10

Summary

This thesis is mainly aimed to study the mass composition of cosmic rays at the low energy region of the UHECR spectrum, $10^{15.8}$eV $- 10^{17}$eV, where there are signatures of cosmic rays transition from galactic to an extragalactic origin. Knowing the composition of CRs at this distinctive energy region represents an important constraint on the galactic-extragalactic transition models. For this purpose, the shower maximum, $X_{\max}$, distributions at different energies have been analyzed and the mass composition has been deduced from the first two moments of the distribution, $\langle X_{\max} \rangle$ and $\sigma(X_{\max})$. This represents the first composition measurement of Pierre Auger Observatory at such low energies.

Reaching this result, I used the data collected by the High Elevation Auger Telescopes, HEAT. The unique thing about HEAT is its ability to observe the upper limit of the atmosphere where the low energy showers are developing and can be measured. Furthermore, HEAT can be tilted down and at this position, it has the same field of view of one of the standard Pierre Auger telescopes, Coihueco. This feature can be used in a fascinating way: to make a direct data-driven of cross-checking, and this what I did exploit to measure the detection resolution of the showers have been reconstructed by the PCGF reconstruction. The measured resolution was comparable to the value found by the Monte Carlo simulations. Furthermore, I also performed a cross-calibration of the hybrid reconstructed data, which were observed by both eyes Coihueco and HEAT in the downward position. This study measured approximately an 8% shift in the reconstructed energy in HEAT compared to that in Coihueco and about 19% in the data of 2014. This was an indication that there is a dependance on the time and the detector status e.g. mirrors and filters cleaning, which is shown to have a direct effect on the measured $X_{\max}$ or energy of the showers. The calibration time dependence of the reconstruction was found for the first time thanks to this study, which was instantly used by Pierre Auger Collaboration to improve the HeCo reconstruction. This study also highlighted the importance of HEAT downward campaigns and suggested a more regular schedule to monitor such effects.

Using the standard hybrid analysis technique was not an option for measuring the mass composition of CRs at such low energies since the showers of these energies are developing at low depths in the atmosphere and can only be observed if their core positions are at close distance to the telescope, where no SD station can be triggered. Fortunately, I can exploit the fact that low energy showers pointing towards the telescopes produce high fraction of the forward Cherenkov light to trigger the pixels of the camera. This is an important advantage with respect to showers of high fluorescence light fraction which are more likely absorbed in the atmosphere before triggering the telescopes. For these reasons, this thesis based on

Cherenkov dominated showers observed by HEAT telescopes and reconstructed using the special FD-based reconstruction, Profile Constrain Geometry Fit (PCGF).

The PCGF reconstruction combines the time fit of the light in the camera and the shape of the profile in a prudent way to constrain the geometries of the reconstructed shower to a good accuracy even without normal hybrid reconstruction. After a lot of improvements and validation in the scope of my thesis, PCGF showed a good stability to produce a full data production from the 1st of January 2012 to 31st December 2015. This was a special data production with high statistics and good quality in comparison to the hybrid and HeCo reconstructions at energies below 10^{17} eV. This data production was also used in the scope of measuring the cosmic rays energy spectrum below 10^{17} eV. A series of event selection criteria are applied to the dataset to ensure excellent quality of the showers used to measure the cosmic rays composition. The main aim of those selection cuts is to improve the analysis of the Cherenkov showers. It was one critical task to extend the determination of the field of view to include the Cherenkov light yield in the same way as the fluorescence light yield was considered before. This was necessary to properly calculate the bias in the measuring X_{max} that raises from the limited field of view of the telescopes.

Carrying out the analysis on Cherenkov showers at low energies required a careful validation, due to the increased importance of the parameterization of the Cherenkov model at low energies. For this task, a realistic full Cherenkov simulation using CORSIKA with SIBYLL-2.3C hadronic model is performed. This validation study was done with special customization to save CPU time that is usually extremely long in such types of simulations. This is mainly achieved by decreasing the random phase-space of the simulation by re-simulating showers of pre-selected geometries from a dedicated CONEX library. Only geometries known to produce more than 50% Cherenkov light and at least 1000 photons at the telescope are considered. The biases on the X_{max} and energy were investigated between the CONEX showers, using the Cherenkov model, and CORSIKA showers with realistic Cherenkov production as a reference. It was found in this study that the Cherenkov model overestimates the Cherenkov photons compared to CORSIKA, and especially at very high Cherenkov percentages, X_{max} showed a bias of about $35 g/cm^2$ at 90% Cherenkov light fraction. This was considered as a correction to tune the CONEX simulations used further in this thesis.

In addition to the CORSIKA library a time dependent simulation library, RealMC, was especially produced with high statistics to study the agreement between the measured and the generated parameters used in the PCGF reconstruction. This RealMC simulation was performed at the same time interval than the dataset, for a mixed composition of proton and iron primaries of 50%, and in the energy range from 10^{15} eV to 10^{17} eV, with spectral index -2. The energy distribution was exactly re-weighted to the measured data. The production of this RealMC library was done with some enhancements. Bearing in mind that the showers geometries must be within a limited solid angle to the telescope viewing axis to produce enough Cherenkov light, an acceptance selection was developed and added to the FD simulation sequence. The reconstruction biases and the detector resolution were estimated at average energy 2.5×10^{16} eV to be 5.4% in the calorimetric energy and $6.4 g/cm^2$ in X_{max} with a detector resolution of $51 g/cm^2$. The dataset is corrected for these reconstruction biases. Comparing the shower geometry parameters like zenith angles and R_p with the data, a very good agreement was found after applying all corrections.

The analysis chain has been successfully tested with the simulation of different mass compositions, which showed some residual deviations changing with the energy, which then have been considered in the systematic uncertainty of the final results. To test systematic effects of the results, the first two moments of the X_{max} distribution were cross-checked with different changes in the reconstruction configuration. The impact of using different

Cherenkov model in the reconstruction was checked, and confirmed the finding of the COR-SIKA study. The analysis is very sensitive to the Cherenkov light production model. Also, the uncertainty of the telescope alignment was checked. Moreover the effect of the atmospheric changes on X_{max} measurements is studied. All these effects were contributed to the systematic uncertainties of $\langle X_{\text{max}} \rangle$ and $\sigma(X_{\text{max}})$. At showers of energy 2.5×10^{16}eV the systematic uncertainty of X_{max} is about $^{+9.68}_{-6.9}$g/cm^2.

A further stability study was performed considering both the zenith angles and Cherenkov fraction together to study the impact on the measurements. This study is preformed for both the data and the RealMC. In general each sample was split into four subsamples at the median values of the zenith and Cherenkov distributions. This study revealed still some correlation between the investigated parameters on the subsamples especially in case of $\sigma(X_{\text{max}})$. This points to remaining inaccuracies of the Cherenkov model in the reconstruction, since this dependence was obviously clear in both data and RealMC samples. Due to this, $\sigma(X_{\text{max}})$ was not used for the final mass composition result, and only the first moment of the X_{max} distribution is considered. The dependence of $\langle X_{\text{max}} \rangle$ on the zenith angle of the shower was limited and in the range of about 18.5g/cm^2 at energy of 2.5×10^{16}eV. The remaining imperfections of this dependence are added as systematic uncertainty, when comparing the unbiased $\langle X_{\text{max}} \rangle$ directly to the predictions from air shower simulations using three different hadronic interaction models EPOS-LHC, QGSJET-II.04, and SIBYLL-2.3C.

The interpretation of the mass composition from the $\langle X_{\text{max}} \rangle$ indicates heavy cosmic ray composition at the second knee energy around 8×10^{16}eV, and getting lighter towards lower energies. This analysis reaches down in energy just before the knee. In light of this result, one can infer that the transition from galactic to extragalactic sources is more likely in the frame of the mixed composition scenario. The dip scenario is less favored or excluded in this context. At this point, one can conclude that the Pierre Auger Observatory mass composition measurements was successfully extended to low energies, almost extending to the knee.

The cosmic ray mass composition study for Pierre Auger Observatory in this energy range is a very important milestone. It was found as one of the results of this thesis that indeed at the moment there is still a lack of availability of comprehensive Cherenkov models to realistically simulate and reconstruct Cherenkov light within the $\overline{\text{Off}\underline{\text{line}}}$ framework. It is an important task to further the Cherenkov models. This will reduce the systematic dependence of the measurements on the zenith angle and Cherenkov light fraction.

The results of this thesis are the first contribution of Pierre Auger Observatory at low energy to ultimately resolve the mystery of the cosmic rays transition from galactic to extragalactic sources. The presence of heavy primaries just before the second knee was unambiguously shown, and the transition to a light composition at the lower energies are very important results. The determination of mass composition at energies corresponding to the Large Hadron Collider (LHC) collisions will enable an exciting test of hadronic interactions in the multi TeV region of $\sqrt{s}$.

Acronyms

This is a list of acronyms used within this work sorted alphabetically according to the short version.

List of Tables

Acknowledgments

Bibliography

[1] V. F. Hess, Über Beobachtungen der Durchdringenden Strahlung bei sieben Freiballonfahrten, Phys. Z. 13 (1912) 1084–1091.

[2] A. Aab, et al., Pierre Auger, Observation of a Large-scale Anisotropy in the Arrival Directions of Cosmic Rays above 8×10^{18} eV, Science 357 (6537) (2017) 1266–1270. arXiv:1709.07321, doi:10.1126/science.aan4338.

[3] A. Aab, et al., Pierre Auger Collaboration, Depth of Maximum of Air-Shower Profiles at the Pierre Auger Observatory: Measurements at Energies above $10^{17.8}$ eV, Phys.Rev.D (2014)arXiv:1409.4809.

[4] R. U. Abbasi, et al., Study of Ultra-High Energy Cosmic Ray composition using Telescope Array's Middle Drum detector and surface array in hybrid mode, Astropart. Phys. 64 (2015) 49–62. arXiv:1408.1726, doi:10.1016/j.astropartphys.2014.11.004.

[5] H. R. F. E. Collaboration, R. Abbasi, T. Abu-Zayyad, M. Allen, J. Amman, G. Archbold, K. Belov, J. Belz, S. B. Zvi, D. Bergman, et al., First observation of the greisen-zatsepin-kuzmin suppression, Physical Review Letters 100 (10) (2008) 101101.

[6] R. Abbasi, M. Abe, T. Abu-Zayyad, M. Allen, R. Azuma, E. Barcikowski, J. Belz, D. Bergman, S. Blake, R. Cady, et al., The cosmic-ray energy spectrum between 2 pev and 2 eev observed with the tale detector in monocular mode, arXiv preprint arXiv:1803.01288 (2018).

[7] C. D. Anderson, Cosmic-ray positive and negative electrons, Physical Review 44 (5) (1933) 406.

[8] Y. Nishina, M. Takeuchi, T. Ichimiya, On the nature of cosmic-ray particles, Physical Review 52 (11) (1937) 1198.

[9] C. M. G. Lattes, G. P. Occhialini, C. F. Powell, Observations on the tracks of slow mesons in photographic emulsions, Nature 160 (4067) (1947) 486.

[10] K. Niu, E. Mikumo, Y. Maeda, A possible decay in flight of a new type particle, Progress of theoretical physics 46 (5) (1971) 1644–1646.

[11] T. Gaisser, F. Halzen, Long-lived tracks in emulsions: New hadrons or background?, Physical Review D 14 (11) (1976) 3153.

[12] J. Blümer, R. Engel, J. R. Hörandel, Cosmic Rays from the Knee to the Highest Energies, arXiv astro-ph/0904.0725 (2009).

[13] E. Mocchiutti, Direct detection of cosmic rays: through a new era of precision measurements of particle fluxes, Nuclear Physics B-Proceedings Supplements 256 (2014) 161–172.

[14] G. Kulikov, G. Khristiansen, On the size spectrum of extensive air showers, Sov. Phys. JETP 35 (8) (1959) 441–444.

[15] D. R. Bergman, J. W. Belz, Cosmic Rays: The Second Knee and Beyond, J. Phys. G34 (2007) R359. arXiv:0704.3721, doi:10.1088/0954-3899/34/10/R01.

[16] W. D. Apel, et al., KASCADE Grande, Kneelike structure in the spectrum of the heavy component of cosmic rays observed with KASCADE-Grande, Phys. Rev. Lett. 107 (2011) 171104. arXiv:1107.5885, doi:10.1103/PhysRevLett.107.171104.

[17] S. P. Knurenko, Z. E. Petrov, R. Sidorov, I. Ye. Sleptsov, S. K. Starostin, G. G. Struchkov, Cosmic ray spectrum in the energy range 1.0E15-1.0E18 eV and the second knee according to the small Cherenkov setup at the Yakutsk EAS array (2013)arXiv:1310.1978.

[18] J. Linsley, Primary cosmic rays of energy 10**17 to 10**20-eV: The energy spectrum and arrival directions, in: 8th International Cosmic Ray Conference (ICRC 1963) Jaipur, India, 1963, Vol. 4, 1963, p. 77.

[19] R. Engel, D. Heck, T. Pierog, Extensive air showers and hadronic interactions at high energy, Ann. Rev. Nucl. Part. Sci. 61 (2011) 467–489. doi:10.1146/annurev.nucl.012809.104544.

[20] A. R. Bell, The Acceleration of cosmic rays in shock fronts. I, Mon. Not. Roy. Astron. Soc. 182 (1978) 147–156.

[21] A. R. Bell, The acceleration of cosmic rays in shock fronts. II., Mon. Not. Roy. Astron. Soc. 182 (1978) 443–455.

[22] M. G. Baring, Diffusive shock acceleration: The Fermi mechanism, in: Very high-energy phenomena in the universe. Proceedings, 32nd Rencontres de Moriond, Les Arcs, France, January 18-25, 1997, 1997, pp. 97–106. arXiv:astro-ph/9711177.

[23] R. Aloisio, Acceleration and propagation of ultra high energy cosmic rays, PTEP 2017 (12) (2017) 12A102. arXiv:1707.08471, doi:10.1093/ptep/ptx115.

[24] G. Navarra, et al., KASCADE-Grande: A large acceptance, high-resolution cosmic-ray detector up to 10**18-eV, Nucl. Instrum. Meth. A518 (2004) 207–209. doi:10.1016/j.nima.2003.10.061.

[25] M. Dova, Ultra-high energy cosmic rays, arXiv preprint arXiv:1604.07584 (2016).

[26] K. Greisen, End to the cosmic-ray spectrum?, Physical Review Letters 16 (17) (1966) 748.

[27] G. T. Zatsepin, V. A. Kuzmin, Upper limit of the spectrum of cosmic rays, JETP Lett. 4 (1966) 78–80, [Pisma Zh. Eksp. Teor. Fiz.4,114(1966)].

[28] C. T. Hill, D. N. Schramm, The Ultrahigh-Energy Cosmic Ray Spectrum, Phys. Rev. D31 (1985) 564. doi:10.1103/PhysRevD.31.564.

[29] F. W. Stecker, M. Salamon, Photodisintegration of ultra-high-energy cosmic rays: A new determination, The Astrophysical Journal 512 (2) (1999) 521.

[30] D. Allard, Extragalactic propagation of ultrahigh energy cosmic-rays, Astroparticle Physics 39 (2012) 33–43.

[31] R. Aloisio, D. Boncioli, A. Di Matteo, A. Grillo, S. Petrera, F. Salamida, Cosmogenic neutrinos and ultra-high energy cosmic ray models, Journal of Cosmology and Astroparticle Physics 2015 (10) (2015) 006.

[32] R. A. Batista, M. Erdmann, C. Evoli, K.-H. Kampert, D. Kuempel, G. Müller, G. Sigl, A. van Vliet, D. Walz, T. Winchen, Crpropa: a public framework to propagate uhecrs in the universe, in: EPJ Web of Conferences, Vol. 99, EDP Sciences, 2015, p. 13004.

[33] A. M. Hillas, The origin of ultra-high-energy cosmic rays, Annual review of astronomy and astrophysics 22 (1) (1984) 425–444.

[34] K. Kotera, A. V. Olinto, The astrophysics of ultrahigh-energy cosmic rays, Annual Review of Astronomy and Astrophysics 49 (2011) 119–153.

[35] D. Allard, A. Olinto, E. Parizot, Signatures of the extragalactic cosmic-ray source composition from spectrum and shower depth measurements, Astronomy & Astrophysics 473 (1) (2007) 59–66.

[36] T. Wibig, A. W. Wolfendale, At what particle energy do extragalactic cosmic rays start to predominate?, J. Phys. G31 (2005) 255–264. arXiv:astro-ph/0410624, doi:10.1088/0954-3899/31/3/005.

[37] V. Berezinsky, Dip in UHECR spectrum as signature of proton interactions with CMB, in: Particle physics at the year of 250th anniversary of Moscow University. Proceedings, 12th Lomonosov Conference on elementary particle physics, Moscow, Russia, August 25-31, 2005, pp. 87–95.

[38] D. Hooper, S. Sarkar, A. M. Taylor, The intergalactic propagation of ultrahigh energy cosmic ray nuclei, Astropart. Phys. 27 (2007) 199–212. arXiv:astro-ph/0608085, doi:10.1016/j.astropartphys.2006.10.008.

[39] R. Aloisio, V. Berezinsky, A. Gazizov, Transition from galactic to extragalactic cosmic rays, Astropart. Phys. 39-40 (2012) 129–143. arXiv:1211.0494, doi:10.1016/j.astropartphys.2012.09.007.

[40] M. Unger, Cosmic Rays above the Knee (2008)arXiv:0812.2763.

[41] D. Allard, G. Decerprit, A. Olinto, E. Parizot, et al., Implications of the cosmic ray spectrum for the mass composition at the highest energies, Journal of Cosmology and Astroparticle Physics 2008 (10) (2008) 033.

[42] B. Rossi, K. Greisen, Cosmic-ray theory, Reviews of Modern Physics 13 (4) (1941) 240.

[43] D. Heck, G. Schatz, T. Thouw, J. Knapp, J. Capdevielle, CORSIKA: A Monte Carlo code to simulate extensive air showers, Forschungszentrum Karlsruhe Report FZKA (1998) 6019.

[44] A. Haungs, H. Rebel, M. Roth, Energy spectrum and mass composition of high-energy cosmic rays, Reports on Progress in Physics 66 (7) (2003) 1145.

[45] W. Heitler, The Quantum Theory of Radiation, third ed. Edition, Oxford University Press, Oxford, 1954.

[46] J. Matthews, A heitler model of extensive air showers, Astropart. Phys. 22 (5-6) (2005) 387–397.

[47] G. Battistoni, S. Roesler, J. Ranft, C. Forti, Deviations from the superposition model in a dual parton model applied to cosmic ray interactions with formation zone cascade in both projectile and target nuclei, Tech. rep. (1996).

[48] G. Rodriguez Fernandez, Air fluorescence yield dependence on atmospheric parameters, in: Proceedings, 30th International Cosmic Ray Conference (ICRC 2007): Merida, Yucatan, Mexico, July 3-11, 2007, Vol. 5, 2007, pp. 933–936.
    URL http://indico.nucleares.unam.mx/contributionDisplay.py?contribId=387&confId=4

[49] G. Lefeuvre, P. Gorodetzky, J. Dolbeau, T. Patzak, P. Salin, Absolute measurement of the nitrogen fluorescence yield in air between 300 and 430 nm, Nucl. Instrum. Meth. A578 (2007) 78–87. arXiv:0704.1532, doi:10.1016/j.nima.2007.04.106.

[50] F. Nerling, J. Blümer, R. Engel, M. Risse, Universality of electron distributions in high-energy air showers—description of cherenkov light production, Astroparticle Physics 24 (6) (2006) 421–437.

[51] J. Jelley, Cerenkov Radiation and Its Applications, CHIZINE PUBN, 2015.
    URL https://books.google.de/books?id=reODswEACAAJ

[52] T. Bergmann, R. Engel, D. Heck, N. N. Kalmykov, S. Ostapchenko, T. Pierog, T. Thouw, K. Werner, One-dimensional Hybrid Approach to Extensive Air Shower Simulation, Astropart. Phys. 26 (2007) 420–432. arXiv:astro-ph/0606564, doi:10.1016/j.astropartphys.2006.08.005.

[53] D. H. Perkins, Particle astrophysics, no. 10, Oxford University Press, 2009.

[54] K.-H. Kampert, M. Unger, Measurements of the Cosmic Ray Composition with Air Shower Experiments, Astropart. Phys. 35 (2012) 660–678. arXiv:1201.0018, doi:10.1016/j.astropartphys.2012.02.004.

[55] P. Abreu, et al., Pierre Auger Collaboration, Interpretation of the Depths of Maximum of Extensive Air Showers Measured by the Pierre Auger Observatory, JCAP 1302 (2013) 026. arXiv:1301.6637, doi:10.1088/1475-7516/2013/02/026.

[56] Eun-Joo Ahn *et al.* (Pierre Auger Collab.), Inferences about the mass composition of cosmic rays from data on the depth of maximum at the Auger Observatory, in: Proc. 33rd Int. Cosmic Ray Conf., Rio de Janeiro, Brazil, 2013.

[57] T. Pierog, K. Werner, EPOS Model and Ultra High Energy Cosmic Rays, Nucl. Phys. Proc. Suppl. 196 (2009) 102–105. arXiv:0905.1198, doi:10.1016/j.nuclphysbps.2009.09.017.

[58] S. Ostapchenko, Monte Carlo treatment of hadronic interactions in enhanced Pomeron scheme: I. QGSJET-II model, Phys. Rev. D83 (2011) 014018. arXiv:1010.1869, doi:10.1103/PhysRevD.83.014018.

[59] F. Riehn, Contributions to the 34th International Cosmic Ray Conference, in: Proceedings, 34th International Cosmic Ray Conference (ICRC 2015): The Hague, The Netherlands,2015.

[60] A. Fedynitch, F. Riehn, R. Engel, T. K. Gaisser, T. Stanev, The hadronic interaction model Sibyll-2.3c and inclusive lepton fluxes (2018)arXiv:1806.04140.

[61] M. Unger, Pierre Auger, Highlights from the Pierre Auger Observatory, PoS ICRC2017 (2018) 1102. arXiv:1710.09478, doi:10.22323/1.301.1102.

[62] The Pierre Auger Observatory: Contributions to the 35th International Cosmic Ray Conference (ICRC 2017). arXiv:1708.06592.
URL http://inspirehep.net/record/1617990/files/arXiv:1708.06592.pdf

[63] A. Aab, et al., The Pierre Auger Collaboration, The Pierre Auger Cosmic Ray Observatory (2015)arXiv:1502.01323.

[64] I. Allekotte, A. Barbosa, P. Bauleo, C. Bonifazi, B. Civit, C. Escobar, B. García, G. Guedes, M. G. Berisso, J. Harton, et al., The surface detector system of the pierre auger observatory, Nuclear Instruments and Methods in Physics Research Section A: Accelerators, Spectrometers, Detectors and Associated Equipment 586 (3) (2008) 409–420.

[65] I. Allekotte, et al., Pierre Auger, The Surface Detector System of the Pierre Auger Observatory, Nucl. Instrum. Meth. A586 (2008) 409–420. arXiv:0712.2832, doi:10.1016/j.nima.2007.12.016.

[66] J. Abraham, et al., Pierre Auger, The Fluorescence Detector of the Pierre Auger Observatory, Nucl. Instrum. Meth. A620 (2010) 227–251. arXiv:0907.4282, doi:10.1016/j.nima.2010.04.023.

[67] D. Veberič, Maps of the Pierre Auger Observatory.
URL https://web.ikp.kit.edu/darko/auger/auger-array/

[68] J. Abraham, M. Aglietta, I. Aguirre, M. Albrow, D. Allard, I. Allekotte, P. Allison, J. A. Muniz, M. Do Amaral, M. Ambrosio, et al., Properties and performance of the prototype instrument for the pierre auger observatory, Nuclear Instruments and Methods in Physics Research Section A: Accelerators, Spectrometers, Detectors and Associated Equipment 523 (1-2) (2004) 50–95.

[69] A. Aab, A. Filipčič, G. K. Mezek, A. Saleh, S. Stanič, M. Trini, D. Veberič, S. Vorobiov, L. Yang, D. Zavrtanik, et al., The Pierre Auger Observatory Upgrade:" AugerPrime": Preliminary Design Report, Observatorio Pierre Auger, 2015.

[70] A. Cordero, et al., Proposal for the Optical System of the Fluorescence Detector of the Auger Project, GAP-note-039 (1996).

[71] M. Born, E. Wolf, Principles of optics: electromagnetic theory of propagation, interference and diffraction of light, Elsevier, 2013.

[72] R. Sato, J. Bellido, H. Reis, Improving the S=N Ratio for the Auger Fluorescence Detector, GAP-note-009 (2000).

[73] M. L. de Oliveira, V. de Souza, H. Reis, R. Sato, Manufacturing the schmidt corrector lens for the pierre auger observatory, Nuclear Instruments and Methods in Physics Research Section A: Accelerators, Spectrometers, Detectors and Associated Equipment 522 (3) (2004) 360–370.

[74] J. Zorn, K. Daumiller, M. D. Rio, R. Engel, H. J. Mathes, R. Smida, L. Tomankova, M. Unger, D. Veberic, The first measurement with the FD operated at a reduced PMT gain, GAP-note-021 (2015).

[75] H. M. for the Pierre Auger Collaboration, et al., The heat telescopes of the pierre auger observatory: Status and first data, in: Proceedings of the 32nd International Cosmic Ray Conference, 2011.

[76] S. Falk, D. Kruppke-Hansen, H.-J. Mathes, S. Müller, R. Ulrich, M. Unger, A First Look at HEAT Data, Auger internal note GAP-2010-123 (2010).

[77] P. A. Collaboration, et al., The pierre auger cosmic ray observatory. submitted to nucl. inst. meth. a, arXiv preprint arXiv:1502.01323 (2015).

[78] R. Knapik, P. Bauleo, B. Becker, J. Brack, R. Caruso, C. D. Fratte, A. Dorofeev, J. Harton, A. Insolia, J. Matthews, et al., The absolute, relative and multi-wavelength calibration of the pierre auger observatory fluorescence detectors, arXiv preprint arXiv:0708.1924 (2007).

[79] F. Arqueros, J. R. Hörandel, B. Keilhauer, Air fluorescence relevant for cosmic-ray detection—summary of the 5th fluorescence workshop, el escorial 2007, Nuclear Instruments and Methods in Physics Research Section A: Accelerators, Spectrometers, Detectors and Associated Equipment 597 (1) (2008) 1–22.

[80] P. Abreu, et al., Pierre Auger Collaboration, Techniques for Measuring Aerosol Attenuation using the Central Laser Facility at the Pierre Auger Observatory, JINST 8 (2013) P04009. arXiv:1303.5576, doi:10.1088/1748-0221/8/04/P04009.

[81] F. Arqueros, et al., Pierre Auger, The Central laser facility at the Pierre Auger Observatory, 2005. arXiv:astro-ph/0507334.
URL http://lss.fnal.gov/cgi-bin/find_paper.pl?conf-05-291-E-TD

[82] J. H. Seinfeld, S. N. Pandis, Atmospheric chemistry and physics: from air pollution to climate change, John Wiley & Sons, 2012.

[83] C. Tomasi, V. Vitale, B. Petkov, A. Lupi, A. Cacciari, Improved algorithm for calculations of rayleigh-scattering optical depth in standard atmospheres, Applied optics 44 (16) (2005) 3320–3341.

[84] J. Abraham, P. Abreu, M. Aglietta, C. Aguirre, E. Ahn, D. Allard, I. Allekotte, J. Allen, J. Alvarez-Muñiz, M. Ambrosio, et al., A study of the effect of molecular and aerosol conditions in the atmosphere on air fluorescence measurements at the pierre auger observatory, Astroparticle Physics 33 (2) (2010) 108–129.

[85] K. Louedec, M. Urban, Extracting the Aerosol Phase Function using the Central Laser Facility, Auger internal note GAP-2011-124 (2011).

[86] A. Filipcic, M. Horvat, D. Veberic, D. Zavrtanik, M. Zavrtanik, M. Chiosso, R. Mussa, G. Sequeiros, M. A. Mostafa, M. D. Roberts, Pierre Auger atmosphere - monitoring lidar system, in: Proceedings, 28th International Cosmic Ray Conference (ICRC 2003): Tsukuba, Japan, July 31-August 7, 2003, 2003, pp. 461–464, [1,461(2003)].
arXiv:astro-ph/0305389.
URL   http://www-rccn.icrr.u-tokyo.ac.jp/icrc2003/PROCEEDINGS/PDF/116.pdf

[87] S. Y. BenZvi, et al., The Lidar System of the Pierre Auger Observatory, Nucl. Instrum. Meth. A574 (2007) 171–184. `arXiv:astro-ph/0609063`, `doi:10.1016/j.nima.2007.01.094`.

[88] P. Abreu, et al., Pierre Auger, Identifying Clouds over the Pierre Auger Observatory using Infrared Satellite Data, Astropart.Phys. 50-52 (2013) 92–101. `arXiv:1310.1641`, `doi:10.1016/j.astropartphys.2013.09.004`.

[89] P. Abreu, et al., Pierre Auger Collaboration, The Rapid Atmospheric Monitoring System of the Pierre Auger Observatory, JINST 7 (2012) P09001. `arXiv:1208.1675`, `doi:10.1088/1748-0221/7/09/P09001`.

[90] B. Keilhauer, M. Will, Pierre Auger, Description of Atmospheric Conditions at the Pierre Auger Observatory Using Meteorological Measurements and Models, Eur. Phys. J. Plus 127 (2012) 96. `arXiv:1208.5417`, `doi:10.1140/epjp/i2012-12096-8`.

[91] P. Abreu, et al., Pierre Auger Collaboration, Description of Atmospheric Conditions at the Pierre Auger Observatory using the Global Data Assimilation System (GDAS), Astropart.Phys. 35 (2012) 591–607. `arXiv:1201.2276`, `doi:10.1016/j.astropartphys.2011.12.002`.

[92] D. Kuempel, K. H. Kampert, M. Risse, Geometry reconstruction of fluorescence detectors revisited, Astropart. Phys. 30 (2008) 167–174. `arXiv:0806.4523`, `doi:10.1016/j.astropartphys.2008.08.003`.

[93] M. Mostafa, The Hybrid Activities of the Pierre Auger Observatory, Nucl. Phys. Proc. Suppl. 165 (2007) 50–58, [,50(2006)]. `arXiv:astro-ph/0608670`, `doi:10.1016/j.nuclphysbps.2006.11.009`.

[94] T. K. Gaisser, A. M. Hillas, Reliability of the method of constant intensity cuts for reconstructing the average development of vertical showers, in: International Cosmic Ray Conference, Vol. 8, 1977, pp. 353–357.

[95] P. Lipari, The Concepts of 'Age' and 'Universality' in Cosmic Ray Showers, Phys. Rev. 79 (2008) 063001. `arXiv:0809.0190`.

[96] P. Lipari, Universality of cosmic ray shower development, Nucl. Phys. Proc. Suppl. 196 (2009) 309–318. `doi:10.1016/j.nuclphysbps.2009.09.060`.

[97] M. Plum, Measurement of the chemical composition of ultra high energy cosmic rays with the HEAT telescopes of the Pierre Auger Observatory, Ph.D. thesis, RWTH Aachen U. (2016).
URL `https://web.physik.rwth-aachen.de/~hebbeker/theses/plum_phd.pdf`

[98] T. Z. AbuZayyad, The Energy Spectrum of Ultra High Energy Cosmic Rays, Ph.D. thesis, Utah U. (2000).
URL `http://www.telescopearray.org/media/papers/tareq_thesis.pdf`

[99] A. Porcelli, Measurement of the Depth of Shower Maximum in the Transition Region between Galactic and Extragalactic Cosmic Rays with the Pierre Auger Observatory, Ph.D. thesis, KIT, Karlsruhe (2014).
URL `http://nbn-resolving.org/urn:nbn:de:swb:90-433535`

[100] FD slowcontrol actions.
URL `https://web.ikp.kit.edu/kai/Auger/SCS/logbrowser.html`

[101] S. Argiro, S. L. C. Barroso, J. Gonzalez, L. Nellen, T. C. Paul, T. A. Porter, L. Prado, Jr., M. Roth, R. Ulrich, D. Veberic, The Offline Software Framework of the Pierre Auger Observatory, Nucl. Instrum. Meth. A580 (2007) 1485–1496. `arXiv:0707.1652`, `doi:10.1016/j.nima.2007.07.010`.

[102] J. G. Gonzalez, Pierre Auger, The Offline Software of the Pierre Auger Observatory: Lessons Learned (2012)`arXiv:1208.2154`.

[103] Auger oracle, observer.
URL `https://web.ikp.kit.edu/augeroracle/doku.php?id=auger:observer`

[104] R. Engel, T. K. Gaisser, P. Lipari, T. Stanev, Contributions to the 26th International Cosmic Ray Conference, in: Proceedings, 26th26^{th} International Cosmic Ray Conference (ICRC 1999): Salt Lake City (USA),1999.

[105] AugerWiki, listofcleanings.
URL `https://www.auger.unam.mx/AugerWiki/ListOfCleanings`

[106] J. Debatin, Investigation of Optical Properties of the Fluorescence Telescopes of the Pierre Auger Observatory (2015).

[107] J. Bellido, Tracking HEAT and CO calibrations and the effects on X_{max} for the HeCo system, Presentation in Paris Analysis Meeting June 2017 (06 2017).

[108] F. Nerling, J. Bluemer, R. Engel, M. Risse, Universality of electron distributions in high-energy air showers: Description of Cherenkov light production, Astropart. Phys. 24 (2006) 421–437. `arXiv:astro-ph/0506729`, `doi:10.1016/j.astropartphys.2005.09.002`.

[109] D. Heck, T. Pierog, Extensive air shower simulation with CORSIKA: A user's guide, Institut für Kernphysik, Forschungszentrum Karlsruhe, Karlsruhe, Germany, guide for version 7.5601 (2016).

[110] H. Fesefeldt, Report **PITHA-85/02**, in: RWTH Aachen, 1985.
URL `http://cds.cern.ch/record/162911/files/CM-P00055931.pdf`

[111] D. Heck, J. Knapp, Upgrade of the Monte Carlo Code CORSIKA to Simulate Extensive Air Showers with Energies $> 10^{20}$ eV, Report FZKA 6097B, Karlsruhe (1998).

[112] L. Perrone, M. Risse, Comparison of Cherenkov Light Emission in GEANT and CORSIKA, GAP-note-060 (2002).

[113] P. Younk, B. Fick, On SDP Reconstruction Accuracy, GAP-note-086 (2006).

[114] E. J. Ahn, J. Bellido, S. BenZvi, R. Engel, F. Schüssler, R. Ulrich, M. Unger, Measurement of the Depth of Shower Maximum of Cosmic Rays above 10^{18} eV, GAP-note-078 (2009).

[115] M. Unger, J. Bellido, Private comunication.

[116] L. Prado, B. R. Dawson, S. Petrera, R. C. Shellard, M. G. do Amaral, R. Caruso, R. Sato, J. A. Bellido, Simulation of the fluorescence detector of the Pierre Auger Observatory, Nucl. Instrum. Meth. A545 (2005) 632–642. `doi:10.1016/j.nima.2005.01.346`.

[117] R. Ulrich, J. Bluemer, R. Engel, F. Schuessler, M. Unger, Manual of fluorescence detector simulation in Offline, GAP-note-014 (2008).

[118] H. M. J. Barbosa, F. Catalani, J. A. Chinellato, C. Dobrigkeit, Determination of the calorimetric energy in extensive air showers, Astropart. Phys. 22 (2004) 159–166. arXiv:astro-ph/0310234, doi:10.1016/j.astropartphys.2004.06.007.

[119] A. G. Mariazzi, P. A. Collaboration, et al., A new method for determining the primary energy from the calorimetric energy of showers observed in hybrid mode on a shower-by-shower basis, arXiv preprint arXiv:1107.4804 (2011).

[120] A. Aab, et al., Pierre Auger, The Pierre Auger Observatory: Contributions to the 33rd International Cosmic Ray Conference (ICRC 2013), in: Proceedings, 33rd International Cosmic Ray Conference (ICRC2013): Rio de Janeiro, Brazil, July 2-9, 2013, 2013. arXiv:1307.5059.
URL http://lss.fnal.gov/archive/2013/conf/fermilab-conf-13-285-ad-ae-cd-td.pdf

[121] F. Fenu, Pierre Auger, The cosmic ray energy spectrum measured using the Pierre Auger Observatory (2017) 9–16[PoSICRC2017,486(2018)]. doi:10.22323/1.301.0486.

[122] T. Pierog, K. Werner, Muon production in extended air shower simulations, Phys. Rev. Lett. 101 (2008) 171101. doi:10.1103/PhysRevLett.101.171101.
URL https://link.aps.org/doi/10.1103/PhysRevLett.101.171101

[123] S. Ostapchenko, Air shower development: impact of the LHC data, in: Proceedings, 32nd International Cosmic Ray Conference (ICRC 2011): Beijing, China, August 11-18, 2011, Vol. 2, p. 71. doi:10.7529/ICRC2011/V02/0681.

[124] J. Bellido, Pierre Auger, Depth of maximum of air-shower profiles at the Pierre Auger Observatory: Measurements above $10^{17.2}$ eV and Composition Implications, PoS ICRC2017 (2018) 506, [,40(2017)]. doi:10.22323/1.301.0506.

[125] R. Abbasi, M. Abe, T. Abu-Zayyad, M. Allen, R. Anderson, R. Azuma, E. Barcikowski, J. Belz, D. Bergman, S. Blake, et al., Study of Ultra-High Energy Cosmic Ray composition using Telescope Array's Middle Drum detector and surface array in hybrid mode, Astroparticle Physics 64 (2015) 49–62.

[126] C. C. Jui, T. A. Collaboration, et al., Cosmic ray in the northern hemisphere: Results from the telescope array experiment, in: Journal of Physics: Conference Series, Vol. 404, IOP Publishing, 2012, p. 012037.

[127] R. Abbasi, T. Abu-Zayyad, M. Al-Seady, M. Allen, J. Amman, R. Anderson, G. Archbold, K. Belov, J. Belz, D. Bergman, et al., Indications of proton-dominated cosmic-ray composition above 1.6 eev, Physical Review Letters 104 (16) (2010) 161101.

[128] T. Abu-Zayyad, K. Belov, D. Bird, J. Boyer, Z. Cao, M. Catanese, G. Chen, R. Clay, C. Covault, H. Dai, et al., Measurement of the cosmic-ray energy spectrum and composition from 1017 to 1018.3 ev using a hybrid technique, The Astrophysical Journal 557 (2) (2001) 686.

[129] N. Budnev, O. Chvalaiev, O. Gress, N. Kalmykov, V. Kozhin, E. Korosteleva, L. Kuzmichev, B. Lubsandorzhiev, R. Mirgazov, G. Navarra, et al., The Cosmic Ray Mass Composition in the Energy Range 10ˆ 15-10ˆ 18 eV measured with the Tunka Array: Results and Perspectives, arXiv preprint arXiv:0902.3156 (2009).

[130] C. Pryke, P. Sommers, A measurement of the cosmic ray spectrum and composition at the knee .

[131] S. Knurenko, A. Sabourov, The depth of maximum shower development and its fluctuations: cosmic ray mass composition at e_0>= 10ˆ 17 ev, arXiv preprint arXiv:1010.1185 (2010).

[132] S. P. Knurenko, A. Sabourov, Study of cosmic rays at the yakutsk eas array: energy spectrum and mass composition, Nuclear Physics B-Proceedings Supplements 212 (2011) 241–251.

[133] T. K. Gaisser, T. J. L. Mccomb, K. E. Turver, Elongation Rate of Air Showers and Implications for 10^{17}- 10^{18} eV Particle Interactions., in: 16th International Cosmic Ray Conference. Vol. 9. Conference Papers. EA Session II. Proceedings, Kyoto, Japan, 6-18 August 1979, 1979, pp. 275–280.

[134] J. Linsley, Structure of large air showers at depth 834 G/sq. cm. 3. Applications, Izv. Fiz. Inst. Bulg. Akad. Nauk. 12 (1978) 56–64.

[135] G. Schatz, T. Thouw, K. Werner, J. Oehlschlager, K. Bekk, Validity of the superposition model for extensive air showers, Journal of Physics G: Nuclear and Particle Physics 20 (8) (1994) 1267.
URL http://stacks.iop.org/0954-3899/20/i=8/a=017

[136] S. Petrera, F. Salamida, Update of the X_{max} parameterizations for post-LHC hadronic models, Auger internal note GAP-2018-021 (2018).

[137] R. Ulrich, Pierre Auger, Extension of the measurement of the proton-air cross section with the Pierre Auger Observatory, PoS ICRC2015 (2016) 401. doi:10.22323/1.236.0401.

[138] E.-J. Ahn, R. Engel, T. K. Gaisser, P. Lipari, T. Stanev, Cosmic ray interaction event generator SIBYLL 2.1, Phys. Rev. D80 (2009) 094003. arXiv:0906.4113, doi:10.1103/PhysRevD.80.094003.

[139] Wolfram MathWorld.
URL http://mathworld.wolfram.com/Convolution.html

APPENDIX A

$\overline{\text{Off}\underline{\text{line}}}$ configurations

Listing A.1: Configuration file shows the parameters used to reconstruct the showers with PCGF in $\overline{\text{Off}\underline{\text{line}}}$

```xml
<?xml version="1.0" encoding="iso-8859-2"?>
<!-- Configuration of Module FdProfileConstrainedGeometryFit-->
<FdProfileConstrainedGeometryFit
    xmlns:xsi="http://www.w3.org/2001/XMLSchema-instance"
    xsi:noNamespaceSchemaLocation='@SCHEMALOCATION@/FdProfileConstrainedGeometryFit.xsd'>

  <apLightMethod> eInternal </apLightMethod>
  <!--
    eExternal = aperture light based on mono time fit axis, FdApertureLightKG has to be
    ↪ called BEFORE the FdProfileConstrainedGeometryFit
    eInternal = internal aperture light calculator, FdApertureLightKG has to be called AFTER
    ↪  the FdProfileConstrainedGeometryFit
    eCallForEach = FdApertureLightKG called for each trial geometry, FdApertureLightKG has
    ↪ to be called AFTER the FdProfileConstrainedGeometryFit
  -->

  <checkUnderground> 1 </checkUnderground>
  <prescan> 1 </prescan>
  <scanOnly> 1 </scanOnly>
  <scanStep unit="degree"> 1. </scanStep>
  <scanStart unit="degree"> 10. </scanStart>
  <scanStop unit="degree"> 170. </scanStop>
  <leavingAtmoIsError> 0 </leavingAtmoIsError>
  <onlyDirectLight> 0 </onlyDirectLight>
  <delZeroLightFlux> 0 </delZeroLightFlux>
  <useLightFlux> 1 </useLightFlux>
  <useNoiseBins> 1 </useNoiseBins>
  <antiAliasingFilterCorrection> 1 </antiAliasingFilterCorrection>
  <!-- Select appropriate time fit model (GAP-2007-099):
       0 = using vacuum atmosphere
       1 = taking reduced speed of light...-->
  <TimeFitModel> 1 </TimeFitModel>
  <!-- ...and optionally de-excitation times into account (for fluorescence)-->
  <TimeFitDeexcitation> 0 </TimeFitDeexcitation>

  <profile>
    <gaisserHillasType>
```

```
      eClassic
  </gaisserHillasType>

  <gaisserHillasShapeParameters type="eClassic">
    <par id="1">
      <name> eX0 </name>
      <unit> g/cm2 </unit>
      <mean> -121*g/cm2 </mean>
      <sigma> 172*g/cm2 </sigma>
      <range unit="g/cm2"> -1000 500 </range>
      <step unit="g/cm2"> 10 </step>
    </par>
    <par id="2">
      <name> eLambda </name>
      <unit> g/cm2 </unit>
      <mean> 61*g/cm2 </mean>
      <sigma> 13*g/cm2 </sigma>
      <range unit="g/cm2"> 10 150 </range>
      <step unit="g/cm2"> 5 </step>
    </par>
  </gaisserHillasShapeParameters>
  <!-- b) width -->
  <gaisserHillasShapeParameters type="eWidth">
    <par id="1">
      <name> eFWHM </name>
      <unit> g/cm2 </unit>
      <mean>  525*g/cm2 </mean>
      <sigma>  100*g/cm2 </sigma>
      <range unit="g/cm2"> 1 2000 </range>
      <step unit="g/cm2"> 10 </step>
    </par>
    <par id="2">
      <name> eAsym </name>
      <unit> perCent </unit>
      <mean> 45.5*perCent </mean>
      <sigma>  1*perCent </sigma>
      <range unit="perCent"> 10 50 </range>
      <step unit="perCent"> 1 </step>
    </par>
  </gaisserHillasShapeParameters>

  <!-- c) USP -->
  <gaisserHillasShapeParameters type="eUSP">
    <par id="1">
      <!-- see Fig. 3 in APP 34(2011)360 -->
      <name> eUspL </name>
      <unit> g/cm2 </unit>
      <mean variables="Ecal"> 225*g/cm2 + (log10(Ecal/eV)-18.5) * 6*g/cm2 </mean>
      <sigma variables="Ecal">  15*g/cm2 </sigma>
      <range unit="g/cm2"> 1 1000 </range>
      <step unit="g/cm2"> 5 </step>
    </par>
    <par id="2">
      <name> eUspR </name>
      <unit> fraction </unit>
      <mean variables="Ecal"> 0.235*fraction - (log10(Ecal/eV)-18.5) * 0.02  </mean>
      <sigma variables="Ecal">  0.1*fraction </sigma>
      <range unit="fraction"> 0.005 0.995 </range>
      <step unit="fraction"> 0.01 </step>
    </par>
  </gaisserHillasShapeParameters>
```

```xml
      <kUnivConstrained>
        <constrained> 1 </constrained>
        <function variables="Ecal"> 332.6*g/cm2 + 13.67*g/cm2 * log10(Ecal/eV) </function>
        <ksigma unit="g/cm/cm"> 29. </ksigma>
      </kUnivConstrained>
  </profile>

  <zetaOptimization>
    <minZetaAngle unit="degree"> 0.5 </minZetaAngle>
    <maxZetaAngle unit="degree"> 4.5 </maxZetaAngle>
    <stepZetaAngle unit="degree"> 0.1 </stepZetaAngle>
    <safetyMargin unit="degree"> 0.5 </safetyMargin>
    <borderMargin unit="degree"> 0.7 </borderMargin>
  </zetaOptimization>

</FdProfileConstrainedGeometryFit>
```

APPENDIX B

CORSIKA

B.1 CORSIKA steering card

Each event produced by CORSIKA has a particular steering card in which the running parameters are controlled. Here is an example for one of the CORSIKA steering cards used to generated the shower in Fig. 5.3b. The primary particle is proton which has fixed energy, the maximum energy equal the minimum energy equal $6.65 \times 10^{16} eV$. The four standard Auger telescopes and HEAT were described at the observation level and in "ePampaAmarilla" reference coordinate system. The used units are the standard CORSIKA units, GeV for energy, cm for distance and degree for angles. In Section 5.1.1 an explanation for the important parameter and why it is used.

Listing B.1: CORSIKA steering card for the shower Fig. 5.3b

```
RUNNR   6102                          number of run
EVTNR   1                             number of first shower event
NSHOW   1                             number of showers to generate
PRMPAR  14                            primary particle code:proton(14)
ESLOPE  -1.0                          slope of primary energy spectrum
ERANGE 66481557.50655 66481557.50655  energy range of primary particle(GeV)
THETAP 45.33921 45.33921              range of zenith angle (degree)
PHIP   37.08723 37.08723              range of azimuth angle (degree)
SEED    18307   0   0                 seed for hadronic part
SEED    18308   0   0                 seed for EGS4 part
SEED    18309   0   0                 seed for Cherenkov part
MAGNET  19.52  -14.17                 magnetic field Malargue
HADFLG  0  0  0  0  0  2              flags hadr.interact.&fragmentation
ECUTS   0.3  0.3  0.02  0.02          energy cuts:hadr. mu elect. phot.(GeV)
MUMULT  T                             muon multiple scattering angle
ELMFLG  T   T                         em. interaction flags (NKG,EGS)
STEPFC  1.0                           mult. scattering step length fact.
RADNKG  200.E2                        outer radius for NKG lat.dens.distr.
LONGI   T  20.  T  T                  longit.distr. &step size &fit& out
ECTMAP  1.E11                         cut on gamma factor for printout
MAXPRT  1                             max. number of printed events
```

```
DIRECT  ./                              output directory
THIN    1.e-06  20.  0.                 thining parameters
THINH        1.        1.               relation between thin em. and had.
CERFIL 3
ARRANG -85.766999999999996             CONSISTENT WITH OFFLINE
OBSLEV 130000                          observation level (in cm)
CERSIZ 2                               size of Cherenkov bunches
* all TELESCOPES and COREPOS must be in the same coord. system
*        x-pos[cm]    y-pos[cm]   z-pos[cm]   radius[cm] ID  COMMENT
TELESCOPE  -1812835.56   -2730299.78  133185.01    200.0  0   Los Leones
TELESCOPE  2164866.58    -469089.88   137797.89    200.0  0   Los Morados
TELESCOPE  357609.92     3486753.85   138009.16    200.0  0   Loma Amarilla
TELESCOPE  -3189575.93   1502612.80   161490.21    200.0  0   Coihueco
TELESCOPE  -3174112.43   1509557.42   161054.79    200.0  0   Heat
*        x-pos                  y-pos
COREPOS  -3066178.2912411275 1631785.1431316866
*      nm      nm
CWAVLG  280.   430.
* this is adapted to Offline [280-430]
USER    alaa
EXIT
```

B.2   HEAT full CORSIKA simulation and reconstruction

A detailed description for how to move form full CORSIKA simulations to $\overline{\text{Off}\underline{\text{line}}}$ was mentioned in Section 5.1.2. Here is an example for the Module sequence Listing B.2 and boostrap file Listing B.3 used for reconstruct of the HEAT full CORSIKA showers.

Listing B.2: Module sequence for simulate and reconstruct CORSIKA in $\overline{\text{Off}}\underline{\text{line}}$

```xml
<!-- A sequence for HEAT full CORSIKA simulation and reconstruction -->
<!DOCTYPE sequenceFile [
  <!ENTITY % fd SYSTEM "@CONFIGDIR@/standardFdSequences.dtd">
  %fd;
  <!ENTITY % sd SYSTEM "@CONFIGDIR@/standardSdSequences.dtd">
  %sd;
] >
<sequenceFile
  xmlns:xsi="http://www.w3.org/2001/XMLSchema-instance"
  xsi:noNamespaceSchemaLocation='@SCHEMALOCATION@/ModuleSequence.xsd'>
  <enableTiming/>
  <moduleControl>
    <loop numTimes="unbounded" pushEventToStack="yes">
      <module> EventFileReaderOG </module>
      <module> MCShowerCheckerOG </module>
      <loop numTimes="unbounded" pushEventToStack="yes">
        <module> EventGeneratorOG </module>
        <!-- Simulation -->
        <try>
          &FdSimulation;
        </try>
        <try>
           <module> EventBuilderOG </module>
          <!-- export simulation in Offline format -->
          <module> EventFileExporterOG </module>
        </try>
        <!-- Reconstruction -->
        <try>
          <module> EventCheckerOG </module>
          <module> FdCalibratorOG </module>
          <module> FdPulseFinderOG              </module>
          <module> PixelSelectorOG              </module>
          <module> FdSDPFinderOG                </module>
          <module> FdAxisFinderOG               </module>
          <module> FdProfileConstrainedGeometryFit</module>
          <module> FdApertureLightKG            </module>
          <module> FdEnergyDepositFinderKG   </module>
        </try>
        <!-- export the ADST -->
        <module> RecDataWriterNG </module>
      </loop>
    </loop>
  </moduleControl>
</sequenceFile>
```

Listing B.3: boostrap.xml file shows the parameters used to simulate and reconstruct the Cherenkov photons fromCORSIKA in Off‾line‾

```xml
<?xml version="1.0" encoding="iso-8859-1"?>
<!DOCTYPE bootstrap [
  <!ENTITY myConfigFiles '.'>
  <!ENTITY standardSdIdealDetConfig SYSTEM '@CONFIGDIR@/standardSdIdealDetConfig.xml'>
  <!ENTITY standardSdSimModuleConfig SYSTEM '@CONFIGDIR@/standardSdSimModuleConfig.xml'>
  <!ENTITY standardSdRecModuleConfig SYSTEM '@CONFIGDIR@/standardSdRecModuleConfig.xml'>
  <!ENTITY standardFdIdealDetConfig SYSTEM '@CONFIGDIR@/standardFdIdealDetConfig.xml'>
  <!ENTITY standardFdSimModuleConfig SYSTEM '@CONFIGDIR@/standardFdSimModuleConfig.xml'>
  <!ENTITY standardFdRecModuleConfig SYSTEM '@CONFIGDIR@/standardFdRecModuleConfig.xml'>
  <!ENTITY standardHdRecModuleConfig SYSTEM '@CONFIGDIR@/standardHdRecModuleConfig.xml'>

  <!ENTITY defaultOfflineConfig '@CONFIGDIR@'>
]>

<bootstrap
  xmlns:xsi="http://www.w3.org/2001/XMLSchema-instance"
  xsi:noNamespaceSchemaLocation='@SCHEMALOCATION@/bootstrap.xsd'
  xmlns:xlink="http://www.auger.org/schema/types">

  &standardFdIdealDetConfig;
  &standardFdSimModuleConfig;
  &standardFdRecModuleConfig;
  &standardHdRecModuleConfig;

  <centralConfig>
    <configLink
      id        = "ModuleSequence"
      type      = "XML"
      xlink:href = "./ModuleSequence.xml"/>
    <configLink
      id        = "EventFileReader"
      type      = "XML"
      xlink:href = "./EventFileReader.xml"/>
    <configLink
      id        = "EventFileExporter"
      type      = "XML"
      xlink:href = "./EventFileExporter.xml"/>
    <configLink
      id        = "EventGenerator"
      type      = "XML"
      xlink:href = "./EventGenerator.xml"/>
    <configLink
      id        = "FdProfileConstrainedGeometryFit"
      type      = "XML"
      xlink:href = "./FdProfileConstrainedGeometryFit.xml"/>
    <configLink
        id        = "FdEnergyDepositFinder"
        type      = "XML"
        xlink:href = "./FdEnergyDepositFinder.xml"/>
     <configLink
      id        = "FdBackgroundSimulator"
      type      = "XML"
      xlink:href = "./FdBackgroundSimulator.xml"/>
    <configLink
        id        = "AnalyticalCherenkovModel"
        type      = "XML"
        xlink:href = "&defaultOfflineConfig;/AnalyticalCherenkovModel.xml"/>
  </centralConfig>
```

```xml
  <parameterOverrides>
    <configLink id="AnalyticalCherenkovModel">
      <analyticalCherenkovModel>
        <cherenkovDistribution> asymmetric </cherenkovDistribution>
        <wavelengthDepRefraction> 1 </wavelengthDepRefraction>
      </analyticalCherenkovModel>
    </configLink>
    <configLink id="LightAtDiaphragmSimulatorKG">
      <LightAtDiaphragmSimulatorKG>
        <cherDirect> 0 </cherDirect>
        <cherDirectCORSIKA> 1 </cherDirectCORSIKA>
      </LightAtDiaphragmSimulatorKG>
    </configLink>
    <configLink id="ShowerPhotonGenerator">
      <ShowerPhotonGenerator>
        <DirectCherenkovLDF> CORSIKA </DirectCherenkovLDF>
      </ShowerPhotonGenerator>
    </configLink>
    <configLink id="ShowerLightSimulatorKG">
      <ShowerLightSimulatorKG>
        <cherenkovFromCORSIKA> 1 </cherenkovFromCORSIKA>
      </ShowerLightSimulatorKG>
    </configLink>
    <configLink id="TelescopeSimulatorKG">
      <TelescopeSimulatorKG>
      <StoreLightComponentsAtPixels> 1 </StoreLightComponentsAtPixels>
      </TelescopeSimulatorKG>
    </configLink>
    <configLink id="Atmosphere">
      <AtmosphereInterfaceConfig>
        <ProfileModel> SimShower </ProfileModel>
      </AtmosphereInterfaceConfig>
    </configLink>
    <configLink id="FdSDPFinder">
      <FdSDPFinder>
        <minPixels> 4 </minPixels>
      </FdSDPFinder>
    </configLink>
  </parameterOverrides>
</bootstrap>
```

APPENDIX C

Cut list

This list of cuts are used with the program "selectEvents" avilable in the ADST package within the $\overline{\text{Off}}\underline{\text{line}}$ framework. These cuts are described in Section 6.2 and used for both reconstructed data and RealMC simulations.

C.1 General cuts

```
adst cuts version: 1.0
#----------------------------------

eyeCut                   10000
heatOrientationUp


# Data cquisition cuts

badFDPeriodRejection
skipSaturated
noBadPixelsInPulse


# Atmosphere cuts

hasMieDatabase
LidarCloudRemoval        { params:    25
                           nMinusOne: 101  -1.  100. }
MinCloudDepthDistance    { params: -50  50 }
MaxCloudThickness        100
maxVAOD                   0.1


minLgEnergyFD            1e-20
XmaxErrorLessThanXmax
```

C.2   Geometry and profile cuts

```
adst cuts version: 1.0
#------------------------------------
# Geometry cuts

maxZenithFD              80
angleTrackLength         6

relativeEcalError        0.15
GHNdof                   8
!maxCFrac                70
xMaxInFOV 20
xMaxObsInExpectedFOV 60 0
```

APPENDIX D

Calculation of truncated mean of $X_{\mathbf{max}}$

The X_{max} distribution can be described with the exponential modified Gaussian distribution (EMG), which is the convolution [1] of a Gaussian distribution and an exponential distribution, where the exponential define the first interaction point and the Gaussian describes the shower development. As described in Section 6.3 in case of unlimited field of view the mean of X_{max} is given by

$$\langle X_{\text{max}}\rangle^{\infty} = \frac{\int_0^{\infty} x G(x) \otimes E(x) dx}{\int_0^{\infty} G(x) \otimes E(x) dx}, \tag{D.1}$$

where

$$G(x) = \frac{1}{\sigma\sqrt{2\pi}} \exp(\frac{-(x-\mu)^2}{2\sigma^2}), \tag{D.2}$$

and

$$E(x) = \frac{1}{\lambda} \exp(\frac{-x}{\lambda}). \tag{D.3}$$

But in reality the field of view has limits x_1 and x_2, so the mean will be truncated mean $\mu(x_1, x_2)$ and Eq. (D.1) become

$$\langle X_{\text{max}}\rangle^{\text{trun}} = \mu^{\text{trun}}(x_1, x_2) = \frac{\int_{x_1}^{x_2} x G(x) \otimes E(x) dx}{\int_{x_1}^{x_2} G(x) \otimes E(x) dx}. \tag{D.4}$$

The term $f(x) = G(x) \otimes E(x)$ describes the exponential modified Gaussian distribution:

$$\text{emg}(x; \mu, \sigma, \lambda) = \frac{1}{2\lambda} \exp(\frac{\mu-x}{\lambda} + \frac{\sigma^2}{2\lambda^2})\text{erfc}(\frac{\mu-x}{\sqrt{2}\sigma} + \frac{\sigma}{\sqrt{2}\lambda}), \tag{D.5}$$

where erfc is the complementary error function. First, let's calculate the denominator of Eq. (D.4) by simplifying then solving the integral

$$I(x) = \int G(x) \otimes E(x) dx = \int f(x) dx = \int \frac{1}{2\lambda} \exp(\frac{\mu-x}{\lambda} + \frac{\sigma^2}{2\lambda^2})\text{erfc}(\frac{\mu-x}{\sqrt{2}\sigma} + \frac{\sigma}{\sqrt{2}\lambda}) dx$$

$$= \int \frac{1}{2\lambda} \exp(\frac{\mu}{\lambda} + \frac{\sigma^2}{2\lambda^2}) \exp(\frac{-x}{\lambda})\text{erfc}(\frac{\mu + (\sigma^2/\lambda) - x}{\sqrt{2}\sigma}) dx. \tag{D.6}$$

---

[1]Convolution is an integral that expresses the amount of overlap of one function as it shifted over another function [139]

139

Assuming that

$$a = \mu + \frac{\sigma^2}{\lambda}, \qquad\qquad\qquad b = \sqrt{2}\sigma,$$

$$c = \frac{1}{2\lambda}\exp(\frac{\mu}{\lambda} + \frac{\sigma^2}{2\lambda^2}),$$

then the Eq. (D.6) can be simplified to

$$I(x) = \int c\exp(\frac{-x}{\lambda})\text{erfc}(\frac{a-x}{b})dx. \tag{D.7}$$

Using integration by parts and known the integral and derivate of the function erf(x) and erfc(x):

$$\frac{d\,\text{erf}(x)}{dx} = \frac{2}{\sqrt{\pi}}\exp(-x^2), \qquad\qquad \int \text{erf}(x) = x\,\text{erf}(x) + \frac{1}{\sqrt{\pi}}\exp(-x^2),$$

$$\frac{d\,\text{erfc}(x)}{dx} = \frac{-2}{\sqrt{\pi}}\exp(-x^2), \qquad\qquad \int \text{erfc}(x) = x - x\,\text{erf}(x) - \frac{1}{\sqrt{\pi}}\exp(-x^2)$$

$$
\begin{aligned}
I(x) &= c[-\lambda\exp(\frac{b^2-4a\lambda}{4\lambda^2})\text{erf}(\frac{a}{b} - \frac{b}{2\lambda} - \frac{x}{b}) - \lambda\exp(\frac{-x}{\lambda})\text{erfc}(\frac{a-x}{b})] \\
&= c[-\lambda\exp(-\frac{\mu}{\lambda} - \frac{\sigma^2}{2\lambda})\text{erf}(\frac{\mu-x}{\sqrt{2}\sigma}) - \lambda\exp(\frac{-x}{\lambda})\text{erfc}(\frac{\mu + (\sigma^2/\lambda) - x}{\sqrt{2}\sigma})] \\
&= -\lambda[\frac{1}{2\lambda}\exp(\frac{\mu}{\lambda} + \frac{\sigma^2}{2\lambda^2})\exp(-\frac{\mu}{\lambda} - \frac{\sigma^2}{2\lambda})\text{erf}(\frac{\mu-x}{\sqrt{2}\sigma}) + f(x)] \\
&= -\lambda f(x) - \frac{1}{2}\text{erf}(\frac{\mu-x}{\sqrt{2}\sigma})
\end{aligned}
\tag{D.8}
$$

Hence the denominator of Eq. (D.4) is

$$\int_{x_1}^{x_2} f(x)dx = I(x)\Big|_{x_1}^{x_2} = I(x_2) - I(x_1). \tag{D.9}$$

Now coming to the numerator of Eq. (D.4)

$$
\begin{aligned}
J(x) &= \int xG(x) \otimes E(x)dx = \int xf(x)dx = x\int f(x)dx - \iint f(x)dx^2 \\
&= xI(x) - \int I(x)dx \\
&= xI(x) + \lambda\int f(x)dx + \frac{1}{2}\int \text{erf}(\frac{\mu-x}{\sqrt{2}\sigma})dx \\
&= xI(x) + \lambda I(x) + \frac{1}{2}\int \text{erf}(z)(-\sqrt{2}\sigma)dz,
\end{aligned}
\tag{D.10}
$$

where $z = \frac{\mu-x}{\sqrt{2}\sigma}$ and $dx = -\sqrt{2}\sigma dz$ and as $\int \text{erf}(z)dz = z\text{erf}(z) + \frac{1}{\sqrt{\pi}}\exp(-z^2)$

$$
\begin{aligned}
\therefore J(x) &= (x+\lambda)I(x) - \frac{\mu-x}{2}\text{erf}(\frac{\mu-x}{\sqrt{2}\sigma}) - \frac{\sigma}{\sqrt{2}\sigma}\exp(-(\frac{\mu-x}{\sqrt{2}\sigma})^2) \\
&= (x+\lambda)I(x) - \frac{\mu-x}{2}\text{erf}(\frac{\mu-x}{\sqrt{2}\sigma}) - \sigma^2 G(x)
\end{aligned}
\tag{D.11}
$$

Hence D.4 will be

$$\mu^{\text{trun}}(x_1, x_2) = \frac{J(x_2) - J(x_1)}{I(x_2) - I(x_1)}. \tag{D.12}$$

APPENDIX E

Field of view

E.1 The expected FoV

Acceptance of the expected FoV for the observed data at different energy bins.
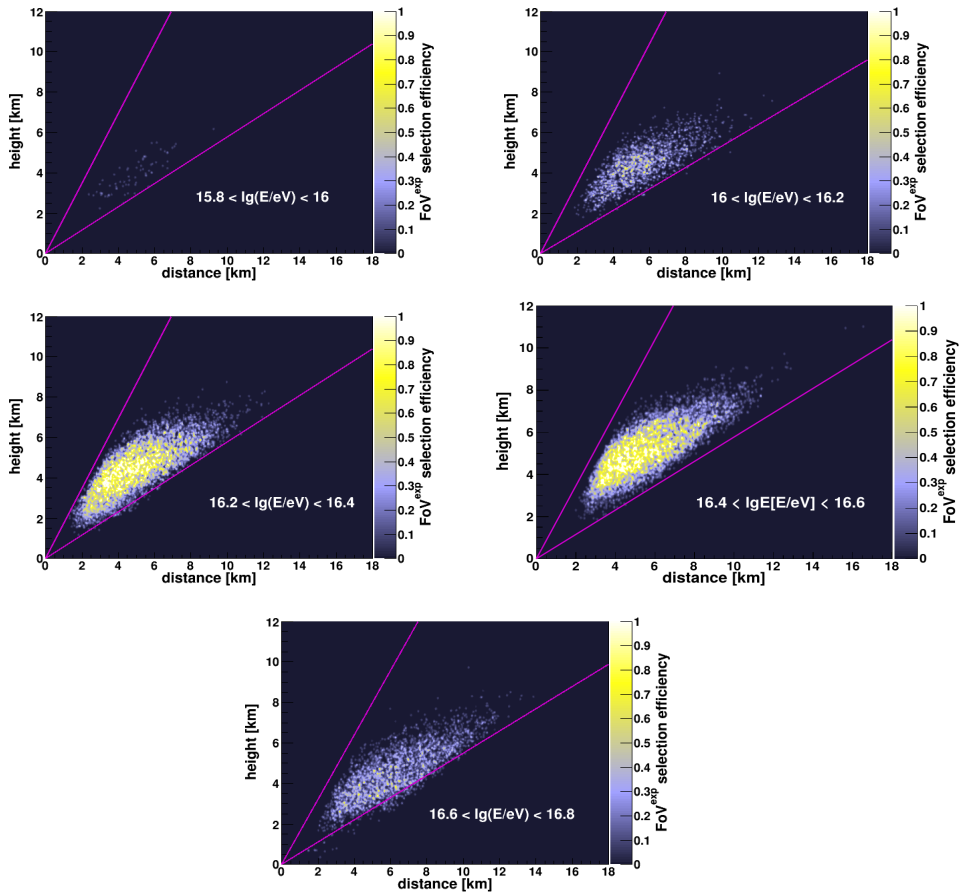
Figure E.1: The expected field of view for data showers in different energy bins with step 0.2 of logarithmic calorimetric energy. On X-axis the ground distance from the shower X_{max} to the HEAT and on Y-axis the hight of X_{max} above the telescope. The magenta lines defined the geometric field of view for HEAT. The color scale describes the efficiency of selected quality showers.

E.2   Fiducial FoV

A collection plots for the fiducial FoV analysis done for both data and RealMC. in Fig. E.2 the plots for the data sample and split in 0.1 of logarithmic calorimetric energy in the range from $10^{15.7}$ eV to 10^{17} eV. In Fig. E.3 the plots for the RealMC simulations in the energy in the range from $10^{15.8}$ eV to $10^{16.9}$ eV.

E.2.1 Data fiducial FoV
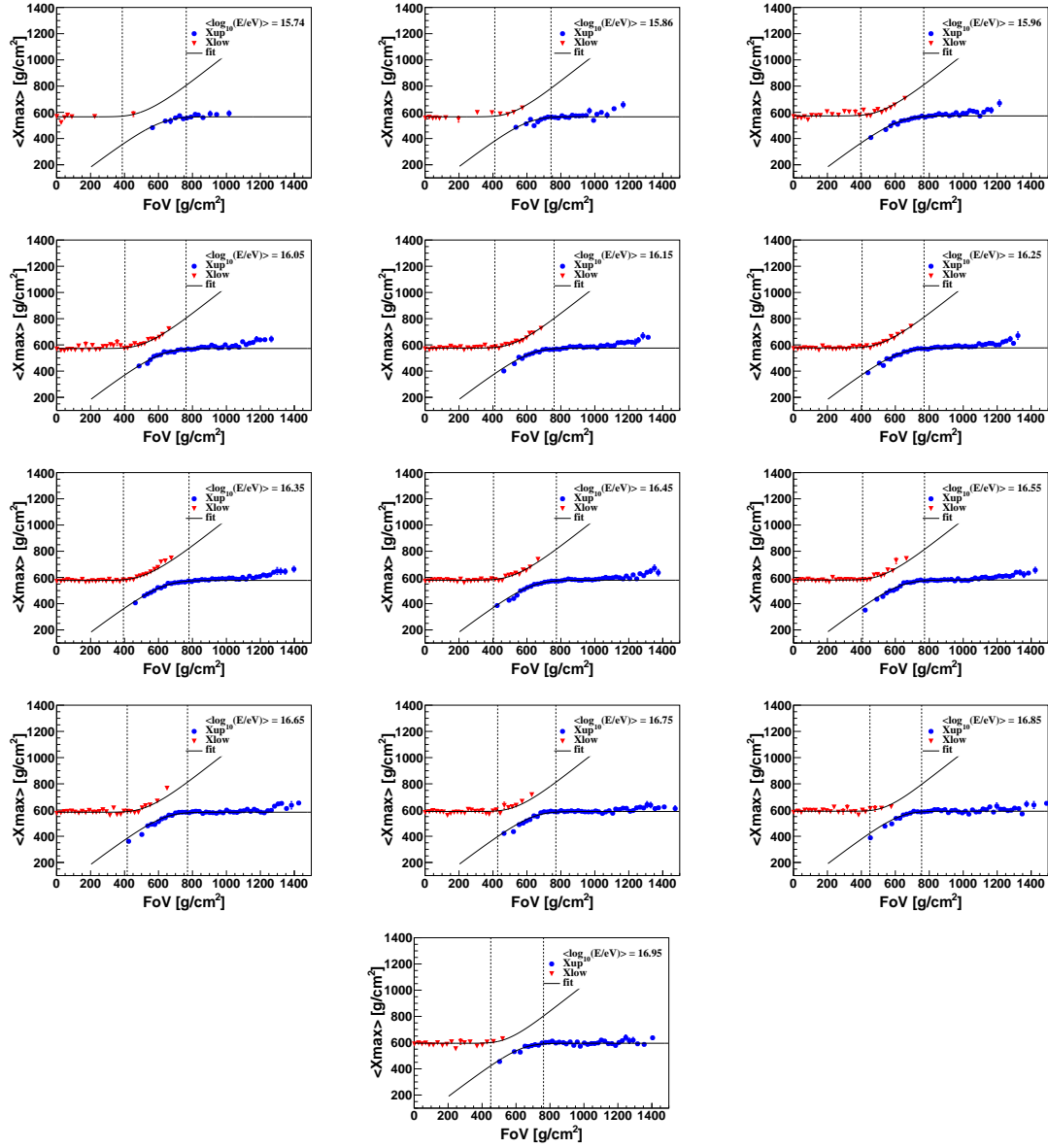
Figure E.2: Collection plots of the fiducial FoV for dataset at different energy bins. $\langle X_{\max} \rangle$ as function of X_{low} (red inverted triangle) and X_{up} (blue dots) fitted with μ^{trun} (black curves). The dashed lines represent the cut values for $\Delta = 5 \text{g}/\text{cm}^2$.

E.2.2   Monte Carlo fiducial FoV
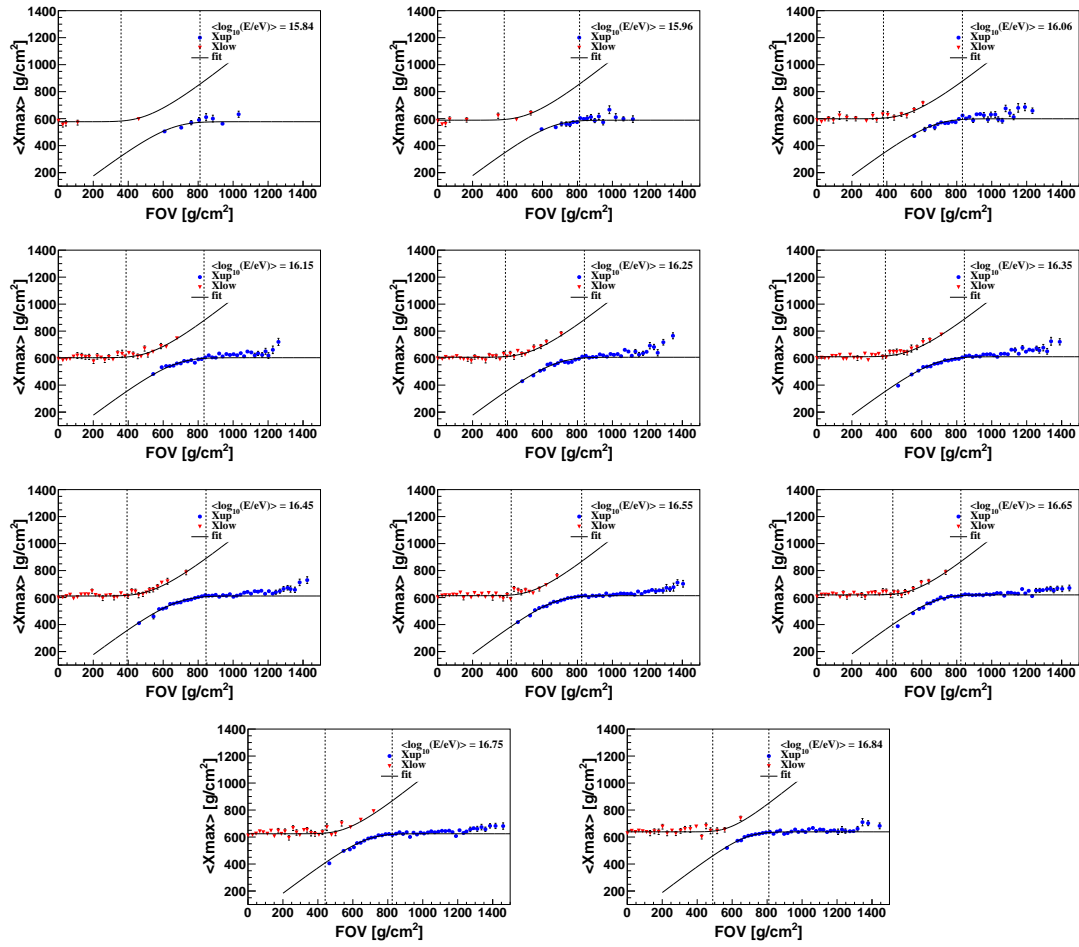
Figure E.3: Collection plots of the fiducial FoV for the RealMC library at different energy bins. $\langle X_{\max} \rangle$ as function of X_{low} (red inverted triangle) and X_{up} (blue dots) fitted with μ^{trun} (black curves). The dashed lines represent the cut values for $\Delta = 5\text{g}/\text{cm}^2$.

APPENDIX F

X_{max} distributions
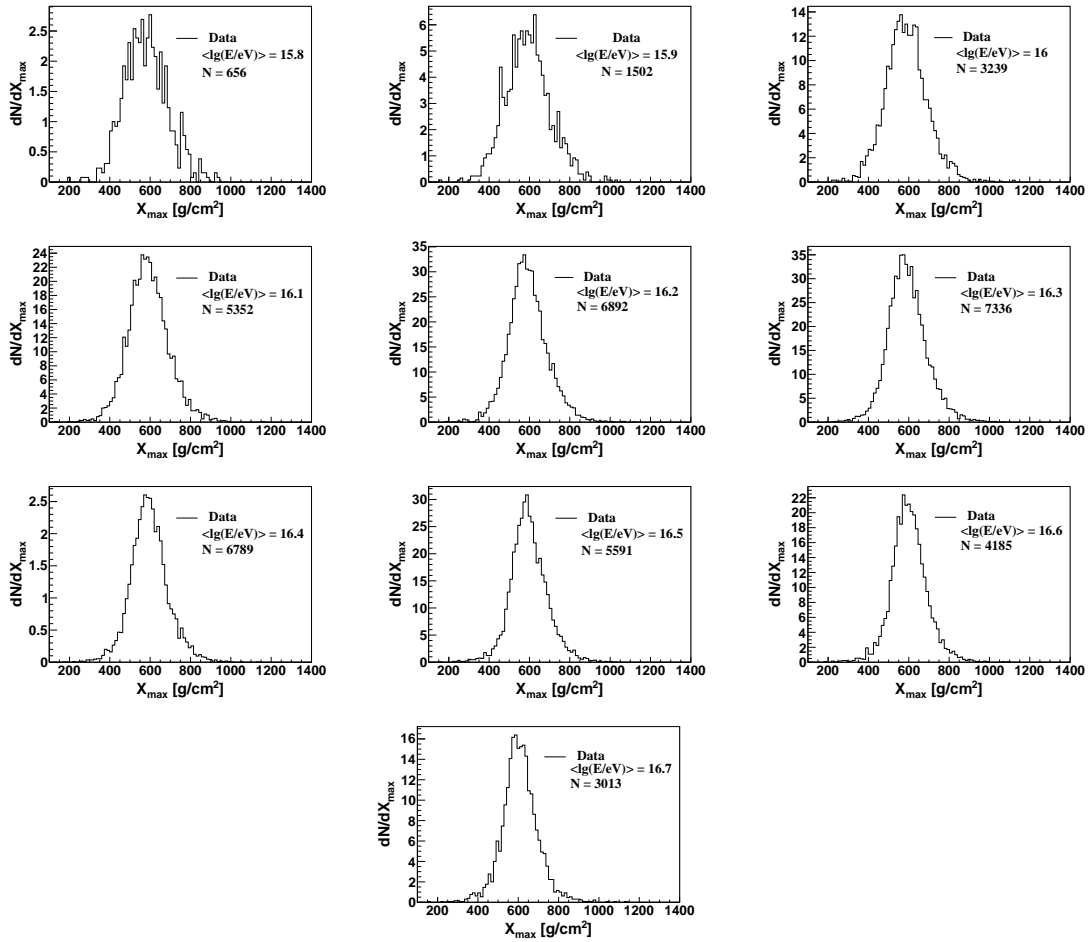
Figure F.1: X_{max} distributions at different energy bins.

APPENDIX G

Data and Monte Carlo shower geometry investigation

G.1 R_p distributions
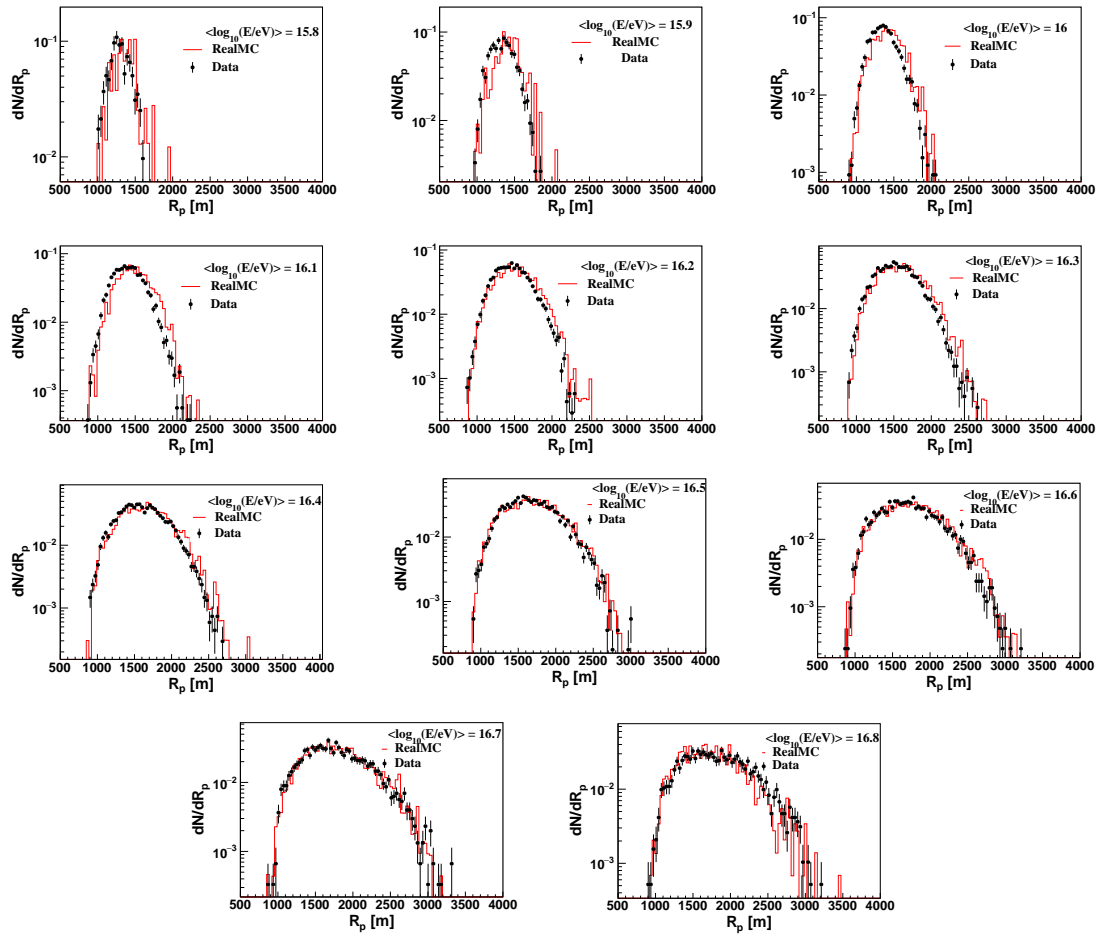
Figure G.1: Comparison plots show the R_p distributions for reconstructed HEAT data (black) and the Monte Carlo (red) in different energy bins cover the range from $10^{15.7}$ eV to $10^{16.9}$.

G.2   Zenith distributions
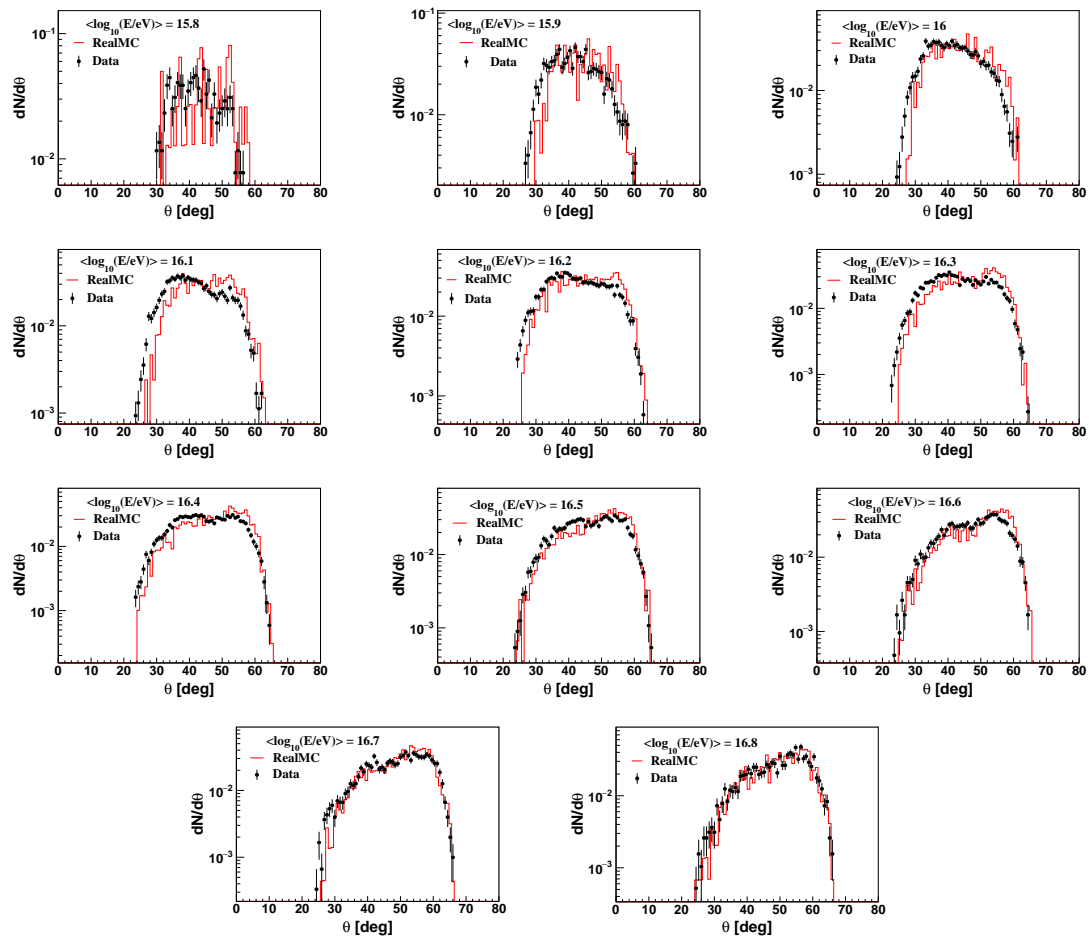
Figure G.2: Zenith angle distributions compared for both reconstructed HEAT data (black) and the Monte Carlo (red) in different energy bins cover the range from $10^{15.7}$ eV to $10^{16.9}$.

Erklärung

Karlsruhe, den 20.09.2018

Erklärung der selbständigen Anfertigung meiner Dissertationsschrift

Hiermit versichere ich, dass ich die Dissertationsschrift mit dem Titel

**Measurements of the maximum depth of air shower profiles at LHC energies
with the High-Elevation Auger Telescopes**

selbständig und ohne unerlaubte fremde Hilfe verfasst habe. Dabei habe ich keine anderen, als die von mir angegebenen Hilfsmittel benutzt.

_____

Your Name